Fall 12-13-2021

Theory of nanospaser: the role of topology and inter-level relaxation.

Rupesh Ghimire

Recommended Citation

Ghimire, Rupesh, "Theory of nanospaser: the role of topology and inter-level relaxation.." Dissertation, Georgia State University, 2021.
doi: https://doi.org/10.57709/26834583

Theory of nanospaser: the role of topology and inter-level relaxation.

by

RUPESH GHIMIRE

Under the Direction of Vadym Apalkov, PhD

ABSTRACT

Spasers are devices based on the effects of a plasmonic field and emulate a laser phenomenon in a nanoscale. A spaser consists of a resonator, which is a metal, and a gain, which is usually a semiconductor. The topological properties of materials are independent of geometrical deformations and are invariant under structural changes and perturbations. The electronic properties of a group called transition metal dichalcogenides(TMDCs), a type of two-dimensional(2D) materials, exhibit robustness around certain symmetry points called valleys, where the dipole-transitions are most probable.

Topological nanospaser consists of a silver nanospheroid and a gain 2D monolayer TMDC placed atop of it. The metallic spheroid acts as a nanoresonator for the plasmonic field. It supports two dipole modes rotating in the opposite directions with surface plasmon resonance frequency (ω_{sp}). When transition frequency in the gain matches to the ω_{sp} of nanospheroid there is a coupling between the plasmonic modes and the chiral valleys (K and K$'$) which results in the generation of plasmons. Here, we selectively pump a single valley and study the dynamics of a nanospaser for different radii of the gain flake. When the radius of TMDC nanoflake is less than the radius of nanospheroid, the plasmons generated are only those which match the chirality of the pumped valley and plasmons with the opposite chirality are absent. However, for a large enough flake size, the plasmonic field outside the footprint of the spheroid polarizes the unpumped valley and the generation of these mismatched plasmonic modes becomes highly probable. In addition, we also analyze the far-field radiation due to this nanospaser.

We, further, study the effects of inter-level relaxation in a spaser system of spherical nanoparticle embedded inside a sphere composed of dye. Assuming gain to be a three-level model, we will explain the effects due to relaxation in the higher energy levels in the generation of plasmons. Contrary to a two-level system spaser where the dependence of plasmons on excitation is linear, we observe a quadratic relationship.

Both these nanospasers have tremendous potential uses in the different areas of infrared spectroscopy, sensing, probing, and mainly biomedical treatment.

INDEX WORDS: Near-field optics, Spaser, Optical pumping, Plasmonics, Symmetry protected topological states, Topological materials, Valleytronics

Theory of nanospaser: the role of topology and inter-level relaxation.

by

RUPESH GHIMIRE

A Dissertation Submitted in Partial Fulfillment of the Requirements for the Degree of

Doctor of Philosophy

in the College of Arts and Sciences

Georgia State University

2021

Theory of nanospaser: the role of topology and inter-level relaxation.

by

RUPESH GHIMIRE

Committee Chair:	Vadym Apalkov
Committee:	Sidong Lei
	Mukesh Dhamala
	Fabien .R. Baron

Electronic Version Approved:

Office of Graduate Studies

College of Arts and Sciences

Georgia State University

December 2021

DEDICATION

To my beloved parents

and friends.

ACKNOWLEDGMENTS

I would like to express my deepest gratitude to my supervisors Professor Mark I. Stockman and Professor Vadym Apalkov for the inspiring support and time consideration during my thesis work. This dissertation could not have been possible without their expert guidance and motivation. My sincerest gratitude and thanks also goes to my committee members: Professor Vadym Apalkov, Professor Sidong Lei, Professor Mukesh Dhamala and Professor Fabien Baron for their time in reviewing my thesis work and precious comments. I would like to thank graduate advisor, Professor Murad Sarsour, the chair of physics and astronomy department, Professor Sebastien Lepine and all professors at Georgia state university for enriching classes.

I am extremely grateful to my parents, sister, and all my colleagues who helped me with their support and guidance to achieve my dreams.

TABLE OF CONTENTS

LIST OF TABLES

LIST OF FIGURES

CHAPTER 1

INTRODUCTION

Numerous inventions have made a mark on the collective development of human race. Amongst them, Laser[1; 2], over 70 years of its introduction, has undeniably shaped almost every aspect of living from communication to medicine. Consequently, miniaturization of a source has enabled laser technology to be integrated with the semiconductor and transistor applications, which has been an elusive goal for a long time. Conventional photonic lasers are limited by size, main reason because light cannot be confined in a cavity with a dimension less than a wavelength. Thus, over the years, continual efforts have been made to design a laser in a sub-wavelength scale which can open path for several applications.

In the last couple of decades, the research has been mostly centered around the capability of metals to fill the requirement of a laser such as optical confinement, feedback, electrical contacts, and thermal management. The approach relies on metals to support EM waves in the form of localized surface plasmons. Bergman and Stockman[3] in 2003 proposed a theory, where surface plasmon waves could also be amplified by stimulated emission – a concept named spaser (surface plasmon amplification by stimulated emission of radiation). Several spaser devices were later build based on this general concept and many are still in development proposing many uses in the area of communication, medicine, defense and other technological areas.

In the following sections, we briefly overview the key concepts of spaser right from the basics of plasmons and light matter interactions.

1.1 Plasmons

Plasmons are the eigenmodes of the oscillation of electrons in a metal. Just as the photon is the quanta of the oscillation of the electromagnetic field, the plasmon is the quanta of the oscillation of electron density within a metal. Since electrons are associated with charge, these oscillations of charge involve the generation of field within the region of oscillation. We can categorize plasmons into 3 main types:

- Bulk Plasmons:

  The bulk plasmon is the most common form of plasmon. The electron density inside a metal undergoes a longitudinal oscillation with a very high frequency called plasma frequency (ω_p). This ω_p is a constant for a given type of material.

- Surface Plasmons:

  The Surface Plasmons(SP) exist on the surface of a metal-dielectric interface and interact with light to form a propagating surface plasmon polaritons. They are evanescent waves that can propagate along the interface with a broad range of plasma frequencies from $\omega = 0$ to $\omega = \omega_p/\sqrt{2}$.

- Localized Surface Plasmons(LSPs):

  LSPs are non-propagating types of plasmons that exist in a metal nanoparticle. The impinging field drives the entire system in oscillation, which is much different from that of the bulk system. They have a striking resemblance with the surface plasmons as the frequency of oscillation of these plasmons(LSP frequency) also depends on the

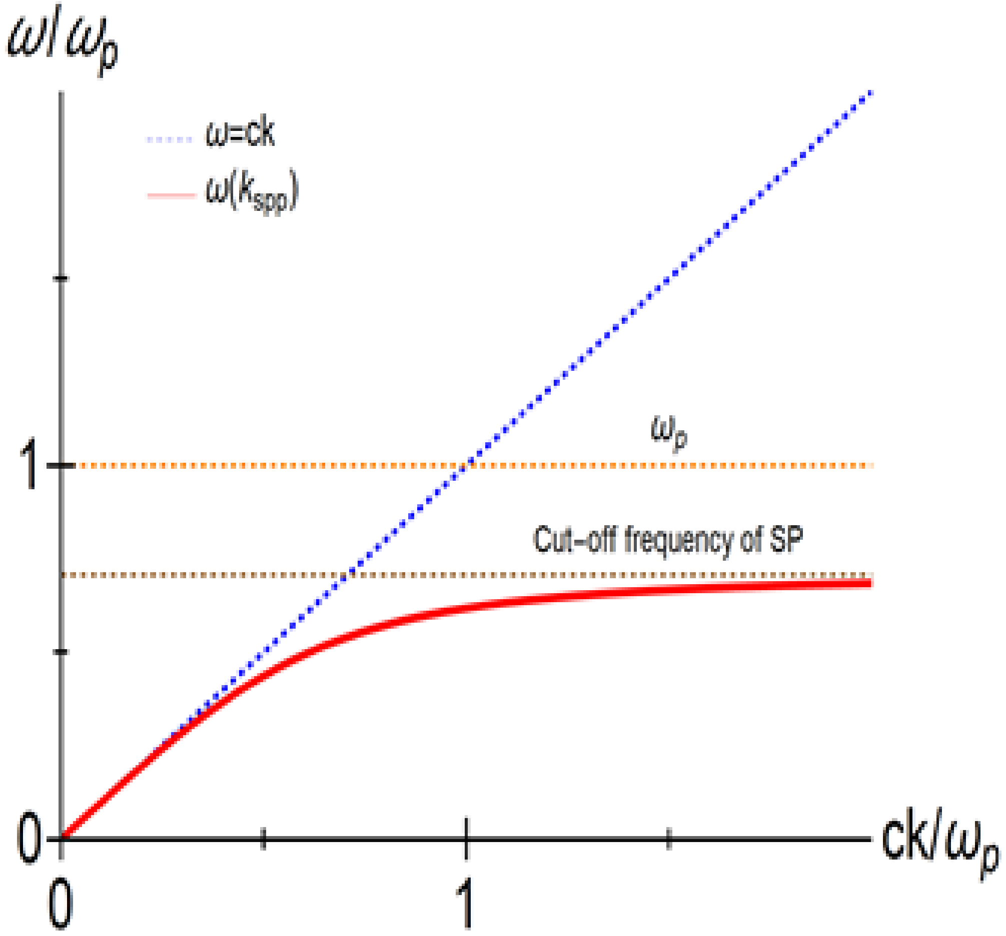

Figure 1.1 Dispersion curve of photon, bulk plasmons and the surface plasmons are represented by of dotted blue, dotted orange and solid red lines respectively. The brown line represents the cut-off frequency of the surface plasmon.

external dielectric environment. However, LSPs are localized within the dimensions of the nanoparticle.

Fig 1.1 shows the dispersion relation of photon, bulk plasmon and surface plasmon. A dotted Blue line indicates the linear dispersion relation of the photon. However, the dispersion curve of the surface plasmon(solid Red) is quadratic in nature. This implies that, for a same value of frequency, surface plasmon can possess higher values of momentum in comparison to photon, which allows the confinement of wavelength in tighter spaces. These surface plasmons can only sustain below a certain value of frequency known as cut-off frequency(dotted brown). Bulk plasmon frequency is constant for a given metal as given by the constant dotted Orange line. The oscillation of electron densities in three different types of plasmons is illustrated in Fig. 1.2[4].

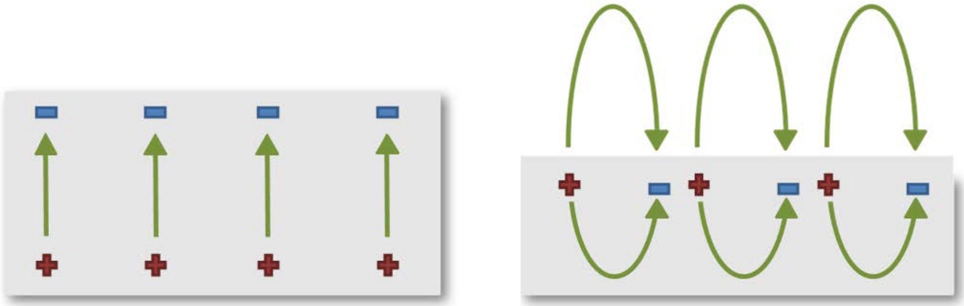

(a) Bulk Plasmons (b) Surface Plasmon Polaritons

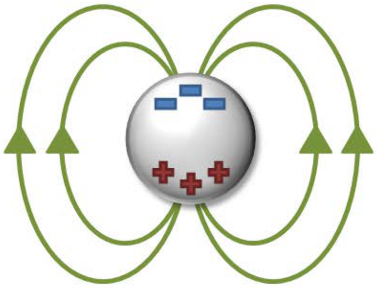

(c) Localized Surface Plasmons

Figure 1.2 Oscillation of electron densities in the (a) Bulk plasmons, (b) surface plasmon, (c) localized surface plasmon). The plus(+) and minus(-) signs represent the separated positive and negative charges which form a dipole. Green lines indicate the direction of electric field due to these dipoles.

1.2 Light-Matter Interaction

Interactions between light and matter have been a subject of great interest in modern research in science. The possible applications are seen in the areas of spectroscopy, sensing, information processing and lasers. Nanostructured optical materials with subwavelength dimensions can exhibit peculiar behavior when they interact with the electromagnetic light(EM wave). The frequency of oscillation(ω_{LSP}) of electrons in a nanoparticle can be tuned by changing the geometry of the particle, environment and several other factors. Understanding the light-matter interaction on the subwavelength scale can open the possibility for several applications. Such interaction is governed by the Maxwell's equations, which we discuss in the next section.

1.2.1 Maxwell's Wave Equations

Maxwell's four equations form a complete description of electric and magnetic field due to electric charges and currents. These equations in a homogeneous and lossless dielectric medium are written in terms of the electric field **E** and magnetic field **H** as

$$\begin{aligned}
\nabla \cdot \mathbf{D} &= 4\pi\rho_{ext}, && \text{(Colomb's law)}\\
\nabla \cdot \mathbf{B} &= 0, && \text{(Gauss Law)}\\
\nabla \times \mathbf{H} &= \frac{1}{c}\frac{\partial \mathbf{D}}{\partial t} + \frac{4\pi}{c}\mathbf{J}_{ext}, && \text{(Ampere's Law)}\\
\nabla \times \mathbf{E} &= -\frac{1}{c}\frac{\partial \mathbf{B}}{\partial t} && \text{(Faraday's Law)}
\end{aligned} \tag{1.1}$$

Here, electric flux density **D** and the magnetic flux density **B** are defined as $\mathbf{D} = \epsilon\mathbf{E}$ and $\mathbf{B} = \mu\mathbf{H}$ respectively, where ϵ and μ denote the permittivity and permeability of the medium. ρ_{ext} is an external charge and $\mathbf{J}_{ext}$ is the current density due to an external source.

Considering the frequency of propagating wave ω and wavevector **k**, the above equations (1.1), in the absence of charge and current i.e. $\rho_{ext} = 0$ and $\mathbf{J}_{ext} = 0$, can be written as(in CGS)

$$\begin{aligned}\mathbf{k}\cdot\mathbf{D} &= 0,\\ \mathbf{k}\cdot\mathbf{B} &= 0.\\ \mathbf{k}\times\mathbf{H} &= -\frac{i\omega\epsilon\mathbf{E}}{c},\\ \mathbf{k}\times\mathbf{E} &= \frac{i\omega\mathbf{B}}{c}\end{aligned} \tag{1.2}$$

On Solving equations (1.2), we obtain Helmholtz equation, which defines the propagation of EM wave in a medium.

$$(\mathbf{k}^2 + \frac{\omega^2}{c^2}\mu\epsilon)\begin{bmatrix}\mathbf{E}\\ \mathbf{H}\end{bmatrix} = 0 \tag{1.3}$$

1.2.2 Waves in a Medium

The electromagnetic waves with frequency ω propagating through a given medium are affected by the permittivity(ϵ_ω) and permeability(μ_ω) of the medium. The medium can be also characterized by electric and magnetic susceptibilities, χ_ω and $\chi_{m,\omega}$. They are related to ϵ_ω and μ_ω by the following equations

$$\begin{aligned}\epsilon_\omega &= (1 + 4\pi\chi_\omega),\\ \mu_\omega &= (1 + 4\pi\chi_{m,\omega})\end{aligned} \tag{1.4}$$

The refractive index, $\mathbf{n}$, of a medium is related to ϵ_ω and μ_ω as

$$\mathbf{n} = \sqrt{\epsilon_\omega\ \mu_\omega} \tag{1.5}$$

The refractive index $\mathbf{n}$, usually a complex quantity, can also be written as a sum of real and imaginary parts

$$\mathbf{n} = n + ik \tag{1.6}$$

where n defines the real part which is related to the transmission of a wave through the medium and k determines the damping of the wave. Further, the electric field and magnetic field in terms of polarization($\mathbf{P}$) and magnetization($\mathbf{M}$) can be written as

$$\begin{aligned} \mathbf{D} &= \epsilon_\omega \mathbf{E} = (1 + 4\pi\chi_\omega)\mathbf{E} = \mathbf{E} + 4\pi\mathbf{P} \\ \mathbf{B} &= \mu_\omega \mathbf{H} = (1 + 4\pi\chi_{m,\omega})\mathbf{H} = \mathbf{H} + 4\pi\mathbf{M} \end{aligned} \tag{1.7}$$

In equations (1.7), we divide the displacement field into two parts; the first part is the response of the free space and the second part is the response of the material. These susceptibilities, in general, show the extent of the displacement of charges or the limit of polarization that can occur inside the material.

The polarization $\mathbf{P}$, current $\mathbf{J}$ and the conductivity σ can be expressed as

$$\begin{aligned} \mathbf{P} &= -\frac{1}{4\pi}(\epsilon_\omega - 1)\mathbf{E} \\ \mathbf{J} &= -\frac{i\omega}{4\pi}(\epsilon_\omega - 1)\mathbf{E} \\ \sigma &= -\frac{i\omega}{4\pi}(\epsilon_\omega - 1) \end{aligned} \tag{1.8}$$

From the above equations (1.8), the relation between ϵ_ω and the σ can be written as

$$\epsilon_\omega = 1 + \frac{4\pi i}{\omega}\sigma \tag{1.9}$$

1.3 Interaction of Electromagnetic Waves with Metal

The optical properties of a metal structure are characterized by the conductivity and electric susceptibility of the material. For metals, there are two main models, the Lorentz model and the Drude model, which can be used to estimate these characteristics. Below we review these models in details.

1.3.1 Lorentz Model

A system of an electron cloud hovering around a nucleus can be thought of as a harmonic oscillator: a mass in a spring. Any external force applied to that mass brings about an oscillatory motion in a system. The equation of motion is given as

$$\begin{gathered} m\frac{\partial^2 \mathbf{r}}{\partial \mathbf{t^2}}+m\Gamma\frac{\partial \mathbf{r}}{\partial t}+m\omega_0^2\mathbf{r}=-q\mathbf{E} \\ \omega_0=\sqrt{\frac{K}{m}} \end{gathered} \tag{1.10}$$

where K is the restoring constant and Γ is a damping parameter and m is the mass of the electron cloud.

The Fourier transform of Eq. (1.10) yields

$$(-m\omega^2-i\omega m\Gamma+m\omega_0^2)\mathbf{r}_\omega=-q\mathbf{E}_\omega \tag{1.11}$$

where $\mathbf{r}_\omega$ and $\mathbf{E}_\omega$ are the Fourier transforms of the displacement and electric field, respectively. Thus, the displacement in terms of driving electric field and mass can be written as

$$\mathbf{r}_\omega=\frac{-q}{m}\frac{\mathbf{E}_\omega}{\omega_0^2-\omega^2-i\omega\Gamma} \tag{1.12}$$

The dipole moment(μ_ω) and the Lorentz polarizability(α_ω)can be written as

$$\begin{aligned}
\mu_\omega &= -q\mathbf{r}_\omega \\
\mu_\omega &= \frac{q^2}{m}\frac{\mathbf{E}_\omega}{\omega_0^2 - \omega^2 - i\omega\Gamma} \\
\alpha_\omega &= \frac{q^2}{m}\frac{1}{\omega_0^2 - \omega^2 - i\omega\Gamma}
\end{aligned} \tag{1.13}$$

The polarization ($\mathbf{P}_\omega$) is associated with the macroscopic behavior of the system contrary to the dipole moment which is defined for an atom. Thus, we take a macroscopic average considering all the atoms are equally polarized. For a given volume V this can be written as

$$\begin{aligned}
\mathbf{P}_\omega &= \frac{1}{V}\sum_V \mu_\omega \\
&= N_q \langle \mu_\omega \rangle
\end{aligned} \tag{1.14}$$

where N_q is the charge density.

Since $\mathbf{P}_\omega = \chi_\omega \mathbf{E}_\omega$, the susceptibility of the material for a given frequency ω can be written as:

$$\begin{aligned}
\chi_\omega &= \frac{Nq^2}{m}\frac{1}{\omega_0^2 - \omega^2 - i\omega\Gamma} \\
&= \frac{\omega_p^2}{\omega_0^2 - \omega^2 - i\omega\Gamma}
\end{aligned} \tag{1.15}$$

where $\omega_p = \frac{Nq^2}{m}$ is the plasma frequency which is fixed for a given material.

Consequently, the dielectric permittivity from Eq. (1.4)can be written as

$$\epsilon_\omega = 1 + 4\pi\frac{\omega_p^2}{\omega_0^2 - \omega^2 - i\omega\Gamma} \tag{1.16}$$

This is a simple model where we account for only one type of resonance where electrons shift back and forth, however, there can be several others like contortion of molecules.

Here is how to convert polarization expressed in CGS and SI units:

$$\begin{aligned} P_{SI} &= P_{CGS}\sqrt{4\pi\epsilon_0} \\ &= \chi_{CGS}\mathbf{E}_{CGS}\sqrt{4\pi\epsilon_0} \\ &= \frac{\chi_{SI}}{4\pi}\sqrt{4\pi\epsilon_0}\mathbf{E}_{SI}\sqrt{4\pi\epsilon_0} \\ &= \epsilon_0\chi_{SI}\mathbf{E}_{SI} \end{aligned}$$

1.3.2 Drude Model

In the Drude model, we consider the restoring force constant equal to zero $K = 0$ which sets the resonant frequency ($\omega_0 = 0$). In this case, the dielectric permittivity from Eq (1.17) is given by

$$\epsilon_\omega = 1 + 4\pi\frac{\omega_p^2}{\omega^2 - i\omega\Gamma} \tag{1.17}$$

Further generalization can be done from the equations above.

1.4 NanoPlasmonics: A Brief Overview

Nanoplasmonics is a branch of condensed matter physics that deals with the optical phenomena in the nanoscale. A common presumption tells that electromagnetic radiation cannot be confined in a space that is half of the light's wavelength which makes the idea to achieve electric field modes within less than micrometer dimensions impossible. However, the remarkable property of a nanoscopic system is that it allows nanoscopic concentration of the optical energy in the modes of oscillations such as surface plasmons or localized surface plasmons. The underlying physics is related to the properties of EM waves in the vicinity of metal surfaces. When driven by the incident electric field, the free-moving electrons in the metal nanoparticles are periodically displaced with respect to their lattice ions. The attraction between these electrons and ions acts as a restoring force to this external field. This results in an electron oscillator, whose quantum is a localized surface plasmon, and the frequency of which depends on the restoring force experienced by the system.

The three important aspects of a nanoscopic system are its high quality factor(Q), great oscillator strength(f), and a small modal volume(V_m). The quality factor Q defines the number of electron oscillations within the relaxation time. It's value for the noble metals is in the range of 10-100. Oscillator strength f is related to the number of conduction electrons which is abundant. It's value in metals is $\sim 10^5$, while in quantum dots it is around 1. Modal volume V_m depends on the size of the nanoparticle and is of the order of nanometers. All these properties of a nanoscopic system makes nanoplasmonics a coveted area of research with numerous applications as biosensors[5–9], optical devices[10–12],photovolatic devices[13] and others.

1.5 Metal Nano-systems

Below we consider only a special type of metal system: metal nanospheroid or metal nanosphere.

1.5.1 A Metal Nanospheroid

1.5.1.1 Geometry and Co-ordinate System

The topological nanospaser consists of a silver metal nanospheroid. We assume that the nanospheroid has an oblate shape with the radius of 12 nm and the height of 1.2 nm. It is described by an azimuthal symmetry and the corresponding plasmonic modes are characterized by azimuthal quantum number m.

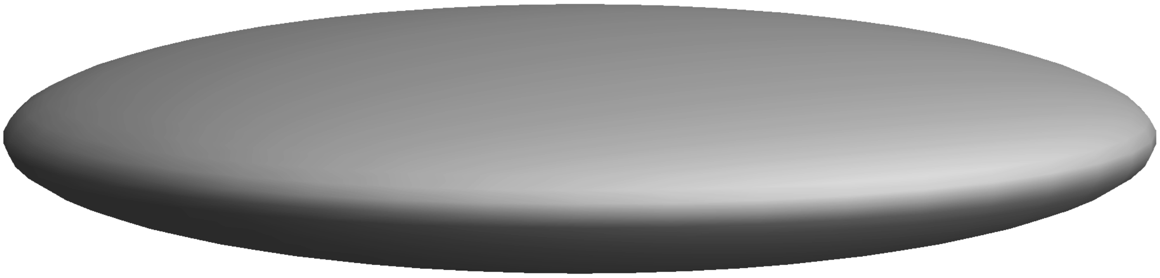

Figure 1.3 An oblate silver nanospheroid

In the Cartesian coordinate system it is described by the following equation

$$\frac{x^2+y^2}{a^2}+\frac{z^2}{c^2}=1\ , \tag{1.18}$$

where a and c are semi-axes, $\varepsilon=\sqrt{1-\frac{c^2}{a^2}}$ is the eccentricity of the spheroid.

It is convenient to introduce the spheroidal coordinates, ξ, η and φ, which are related to the Cartesian coordinates, x, y and z through the following expressions[14]:

$$x=f\sqrt{\xi^2+1}\sqrt{1-\eta^2}\ \cos(\varphi), \tag{1.19}$$

$$y=f\sqrt{\xi^2+1}\sqrt{1-\eta^2}\ \sin(\varphi), \tag{1.20}$$

$$z=f\xi\eta, \tag{1.21}$$

where $0\le\xi<\infty,\quad -1\le\eta\le 1,\quad 0\le\varphi<2\pi$ and $f=\varepsilon a$.

1.5.1.2 Eigenmodes of a Spheroid and Bergman Parameter

Then the surface plasmon eigenmodes of the metal spheroid are described by the quasistatic equation [15]

$$\nabla\left[\theta(\mathbf{r})\nabla\phi_m\right] = s_{\text{sp}}\nabla^2\phi_m, \tag{1.22}$$

where s_{sp} is the eigenvalue of the corresponding mode ϕ_m. Here $\theta(\mathbf{r})$ is the characteristic function that is 1 inside the metal and 0 elsewhere. For oblate spheroid, the eigenmodes are characterized by multipole quantum number l and magnetic quantum number m. For the relevant modes of topological nanospaser, the multipole quantum number is 1, $l = 1$. Then the corresponding eigenmodes are described by the following expressions

$$\phi_m = C_{\text{N}} P_1^m(\eta) e^{im\phi} \begin{cases} \frac{P_1^m(i\xi)}{P_1^m(i\xi_0)}, & 0 < \xi < \xi_0, \\ \\ \frac{Q_1^m(i\xi)}{Q_1^m(i\xi_0)}, & \xi_0 < \xi, \end{cases} \tag{1.23}$$

where $P_l^m(x)$ and $Q_l^m(x)$ are the Legendre functions of the first and second kind, respectively, and $\xi_0 = \frac{\sqrt{1-\varepsilon^2}}{\varepsilon}$. The constant C_{N} is determined by normalization condition,

$$\int_{\text{All Space}} |\nabla\phi(\mathbf{r})_m|^2 d^3\mathbf{r} = 1. \tag{1.24}$$

Due to axial symmetry of the nanospheroid, the corresponding eigenvalues, s_{sp}, do not depend on m. They can be also found from the following expression[3; 16]

$$s_{\text{sp}} = \frac{\displaystyle\int_{\text{All Space}} \theta(\mathbf{r})|\nabla\phi_m(\mathbf{r})|^2 d^3\mathbf{r}}{\displaystyle\int_{\text{All Space}} |\nabla\phi_m(\mathbf{r})|^2 d^3\mathbf{r}}. \tag{1.25}$$

Using explicit expression (1.23) for ϕ_m, we derive the final equation for the eigenvalue

$$s_{\text{sp}} = \left.\frac{\frac{dP_1^m(x)}{dx}}{\frac{dP_1^m(x)}{dx} - \frac{P_1^m(x)}{Q_1^m(x)}\frac{dQ_1^m(x)}{dx}}\right|_{x=i\xi_0} . \tag{1.26}$$

To find the plasmon frequency, ω_{sp}, and the plasmon relaxation rate, γ_{sp}, we use the following relations [3; 16]:

$$s_{\text{sp}} = \text{Re}[s(\omega_{\text{sp}})], \tag{1.27}$$

$$r_{\text{sp}} = \frac{\text{Im}[s(\omega_{\text{sp}})]}{s'_{\text{sp}}}, \qquad s'_{\text{sp}} \equiv \left.\frac{d\text{Re}[s(\omega)]}{d\omega}\right|_{\omega=\omega_{\text{sp}}}, \tag{1.28}$$

where the Bergman spectral parameter is defined as

$$s(\omega) = \frac{\epsilon_d}{\epsilon_d - \epsilon_m(\omega)} . \tag{1.29}$$

Here ϵ_d is the dielectric constant of surrounding medium, and $\epsilon_m(\omega)$ is the dielectric function of the metal (silver). In our computations, for silver, we use the dielectric function from Ref. [17].

1.5.2 A Metal Nanosphere

We use a solid metal silver sphere for our spaser with a three-level system(TLS) of gain. It is isotropic and the eigenmodes within the sphere can be defined by potential expressed in terms of spherical harmonics. For a dipole mode, m=1 and l=0, the potential is given by the following expression

$$\phi(\mathbf{r}) = \left(\frac{a}{r^2} + br\right) Y_{10}(\mathbf{r}), \tag{1.30}$$

where a and b are constants, and $Y_{10}(\mathbf{r})$ is the spherical harmonics function for a dipole mode.

A detailed method to evaluate the LSP frequency of the system using a boundary condition approach is explained in Chapter 4.

1.6 Gain

Gain is another key element of a spaser which supports population inversion and acts as a source of energy for the stimulated emission. We have used two types of gain for the projects based on their electronic properties

1.6.1 Monolayer TMDC

Because of its many unique features, graphene is immensely popular, but its lack of an electronic bandgap has sparked a hunt for 2D materials with semiconducting capabilities. A viable option is transition metal dichalcogenides (TMDCs), which are semiconductors of the form MX_2, where M is a transition metal atom (such as Mo or W) and X is a chalcogen atom (such as S, Se, or Te) as shown in Fig. 1.4. TMDCs have a unique combination of atomic-scale thickness, direct bandgap, strong spin–orbit coupling, and favorable electrical and mechanical properties, making them appealing for fundamental research as well as practical applications. A suitable monolayer TMDC gain is selected for the nanospaser which is circular in shape and lies atop of the nanospheroid. The radii of the TMDC is changed to address the effect of plasmonic field for different size. In our computational work, we mostly use MoS_2 as a gain, though the choice remains feasible as suited to the requirements.

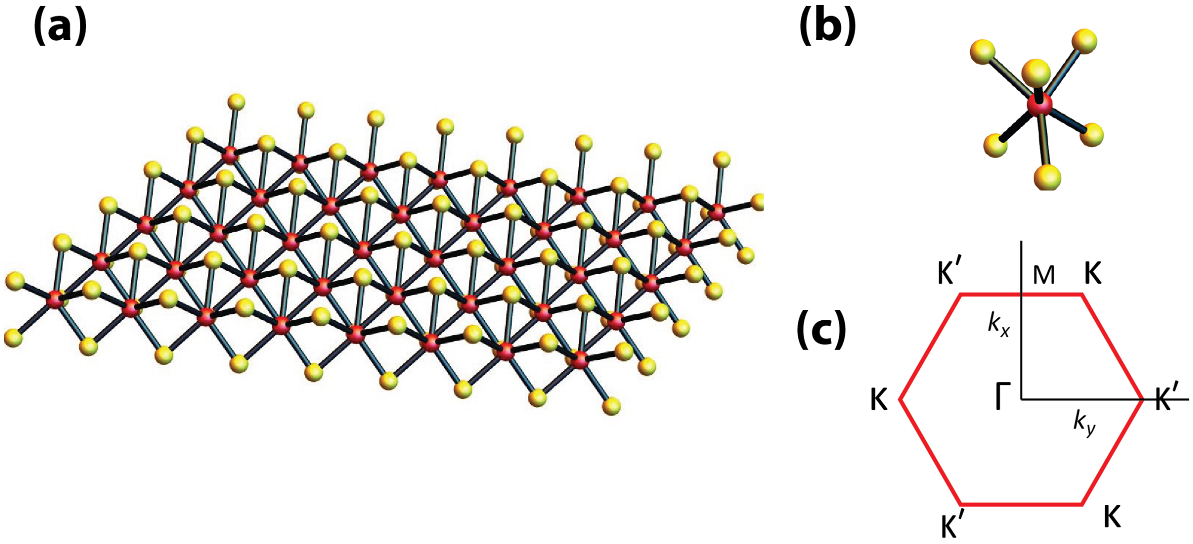

Figure 1.4 (a) a crystal structure of monolayer TMDC showing a layer of molybdenum atoms (Red) sandwiched between two layers of sulfur atoms (yellow) (b) Unit cell of a TMDC in a real space (c) hexagonal Brillouin zone in a reciprocal space characterized by the momentum vectors k_x and k_y with symmetric points $\mathbf{K}$,$\mathbf{K}'$, $\mathbf{\Gamma}$ and $\mathbf{M}$.

1.6.1.1 Electronic properties of the Gain

The electronic properties of these TMDCs are dominated by the two in-equivalent valleys that occur at the **K** and **K′** points (see Fig.1.4(c)), which lie at the edges of Brillouin zone. These valleys can be represented by a binary pseudo-spin which resembles the behavior of a spin-1/2 system; the electrons in one valley(**K**) designated as spin up and the electrons in the other valley($\mathbf{K}'$) as spin down.

Band Structure

A monolayer TMDC has some peculiar properties compared to it's bulk structure. One of the most important characteristics is the presence of a direct band-gap in the valleys. This band-gap enhances the properties like electronic transition rate, absorption and conduction of the material. Here, we study a band structure of a monolayer MoS_2 using 3-band tight binding model [18]. The Hamiltonian matrix in this model is expressed as

$$\mathbf{H}_{TMDC} = \begin{pmatrix} h_0 & h_1 & h_2 \\ h_1^\dagger & h_{11} & h_{12} \\ h_2^\dagger & h_{12}^\dagger & h_{22} \end{pmatrix} \tag{1.31}$$

where,

$$\begin{aligned}
h_0 &= 2t_0(2\cos(\alpha)\cos(\beta) + \cos(2\alpha)) + \epsilon_1 \\
h_1 &= -2\sqrt{3}\mathrm{t}_2\sin(\alpha)\sin(\beta) + 2i\mathrm{t}_1(\sin(\alpha)\cos(\beta) + \sin(2\alpha)) \\
h_2 &= 2\mathrm{t}_2(\cos(2\alpha) - \cos(\alpha)\cos(\beta)) + 2i\sqrt{3}\mathrm{t}1\cos(\alpha)\sin(\beta) \\
h_{11} &= 2\mathrm{t}_{11}\cos(2\alpha) + \cos(\alpha)\cos(\beta)(\mathrm{t}_{11} + 3\mathrm{t}_{22}) + \epsilon_2 \\
h_{22} &= \cos(\alpha)\cos(\beta)(3\mathrm{t}_{11} + \mathrm{t}_{22}) + 2\mathrm{t}_{22}\cos(2\alpha) + \epsilon_2 \\
h_{12} &= \sqrt{3}\sin(\alpha)\sin(\beta)(\mathrm{t}_{22} - \mathrm{t}_{11}) + 4i\mathrm{t}_{12}\sin(\alpha)(\cos(\alpha) - \cos(\beta))
\end{aligned} \tag{1.32}$$

with $\alpha = \frac{1}{2}k_x a$ and $\beta = \frac{\sqrt{3}}{2}k_y a$. Here, $\epsilon_1,\ ,\epsilon_2,\ t_0,\ t_1,\ t_2,\ t_{11},\ t_{12}$ and t_{22} are the on-site energies and inter-orbital hopping parameters, which are derived from the results of LDA and

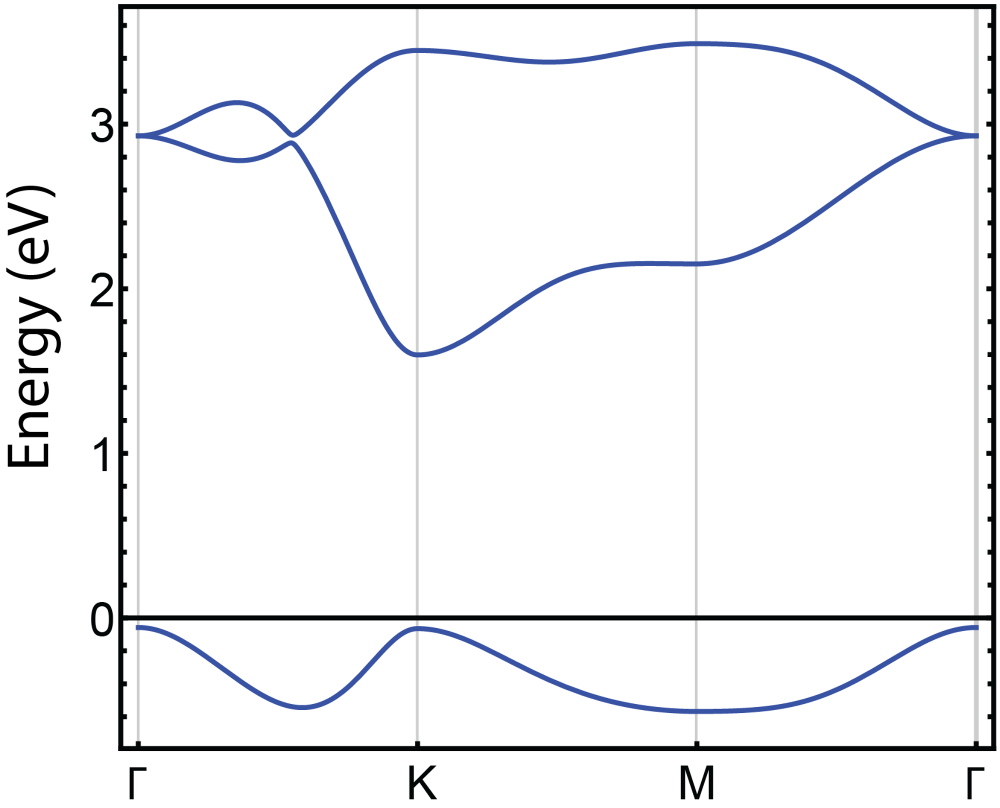

Figure 1.5 Electronic band structure diagram of MoS_2 calculated using 3-band tight binding model

GGA calculations[18]. The values of these parameters differ for different types of TMDCs.

Energy band diagram of a monolayer MoS_2 is shown in the Fig. 1.5. The bottom most conduction band and top most valance band are closest to each other about the **K** point which shows a presence of a direct band-gap. The band-gap of a monolayer MoS_2 was theoretically calculated to be 1.66 eV. Similar calculations were done for other TMDCs too.

Berry Curvature and Topological Charge

In solids, the topological properties are determined by the change of phase of an electron wavefunction within a unit cell of the reciprocal space and are quantified by the Berry connection and the corresponding Berry curvature. The Berry curvature acts as a magnetic field in the reciprocal space and the flux of the Berry curvature through the first Brillouin zone determines the topological charge that is quantized and is called the Chern number. While for the systems with time-reversal symmetry the total topological charge is zero, if the time-reversal symmetry is broken, e.g., by magnetic field, the topological charge can be non-zero. The famous examples of such quantization for the systems with broken time-reversal symmetry is Quantum Hall Effect, where the Hall conductance is proportional to the topological charge and quantized.

Although for the systems with time-reversal symmetry the total topological charge is zero, it can take non-zero values within some regions of the reciprocal space. That determines nontrivial topology of the systems. The examples of such systems are graphene-like materials, such as graphene, silicene, germanene, and TMDC. In these materials there are points in the reciprocal space, where the Berry curvature is singular, like in graphene, or has maximum, like in TMDC. These points are called the Dirac points or valleys as discussed above in section 1.6.1.1 The total flux of the Berry curvature through the surface that encloses the Dirac point is quantized topological charge, which is related to the geometric Berry phase accumulated by an electron along a path that encloses the Dirac point. For different valleys the topological charges are opposite so the total topological charge for the whole system is zero. Because of the nontrivial topology of the valleys in TMDC, the electron states of the valleys are chiral with opposite chirality for two valleys, $\mathbf{K}$ and $\mathbf{K}'$.

TMDC	Dipole elements (D)		Band gap (eV)
	$\mathbf{d}_{\mathbf{K}}$	$\mathbf{d}_{\mathbf{K}'}$	
MoS_2	$17.68\mathbf{e}_+$	$17.68\mathbf{e}_-$	1.66
$MoSe_2$	$19.23\mathbf{e}_+$	$19.23\mathbf{e}_-$	1.79
WSe_2	$18.38\mathbf{e}_+$	$18.38\mathbf{e}_-$	1.43
$MoTe_2$	$20.08\mathbf{e}_+$	$20.08\mathbf{e}_-$	1.53

Table 1.1 Parameters employed in the calculations: dipole matrix elements and band gaps of the TMDCs.

Transition Dipole Matrix

The plasmonic field modes of the nanospheroid couple to the dipole of the TMDC resulting in a spasing process. For a conduction band c and valance band v, the inter-band transition is governed by a non-Abelian k-space gauge potential called Berry connection[19; 20] $\boldsymbol{A}_{cv}(\mathbf{k})$ which is given as

$$\boldsymbol{A}_{cv}(\mathbf{k}) = i\left\langle \psi_{\mathbf{k}}^{(c)} | \nabla_{\mathbf{k}} \psi_{\mathbf{k}}^{(v)} \right\rangle, \tag{1.33}$$

where $\psi_{\mathbf{k}}^{(c)}$ and $\psi_{\mathbf{k}}^{(c)}$ are the eigenstates of the Hamiltonian given in Eq. 1.31 at a given momentum $\mathbf{k} \sim \mathbf{k}(kx, ky)$. The dipole matrix elements can then be written as

$$D_{cv}(\mathbf{k}) = e\mathbf{A}_{cv}(\mathbf{k}). \tag{1.34}$$

where e is the electronic charge.

The calculated values of the transition dipole matrix elements and the bandgap are given in Table 1.1. The dipole matrix elements at the $\mathbf{K}$ and $\mathbf{K}'$ points are purely chiral. They are proportional to $\mathbf{e}_\pm = 2^{-1/2}\left(\mathbf{e}_x \pm i\mathbf{e}_y\right)$, where $\mathbf{e}_x$ and $\mathbf{e}_y$ are the Cartesian unit vectors. The plot of the absolute value of the chiral dipole, $|\mathbf{d}_\pm|$, where $\mathbf{d}_\pm = \mathbf{e}_\pm^* \mathbf{d}$, is shown in Fig. 1.6.

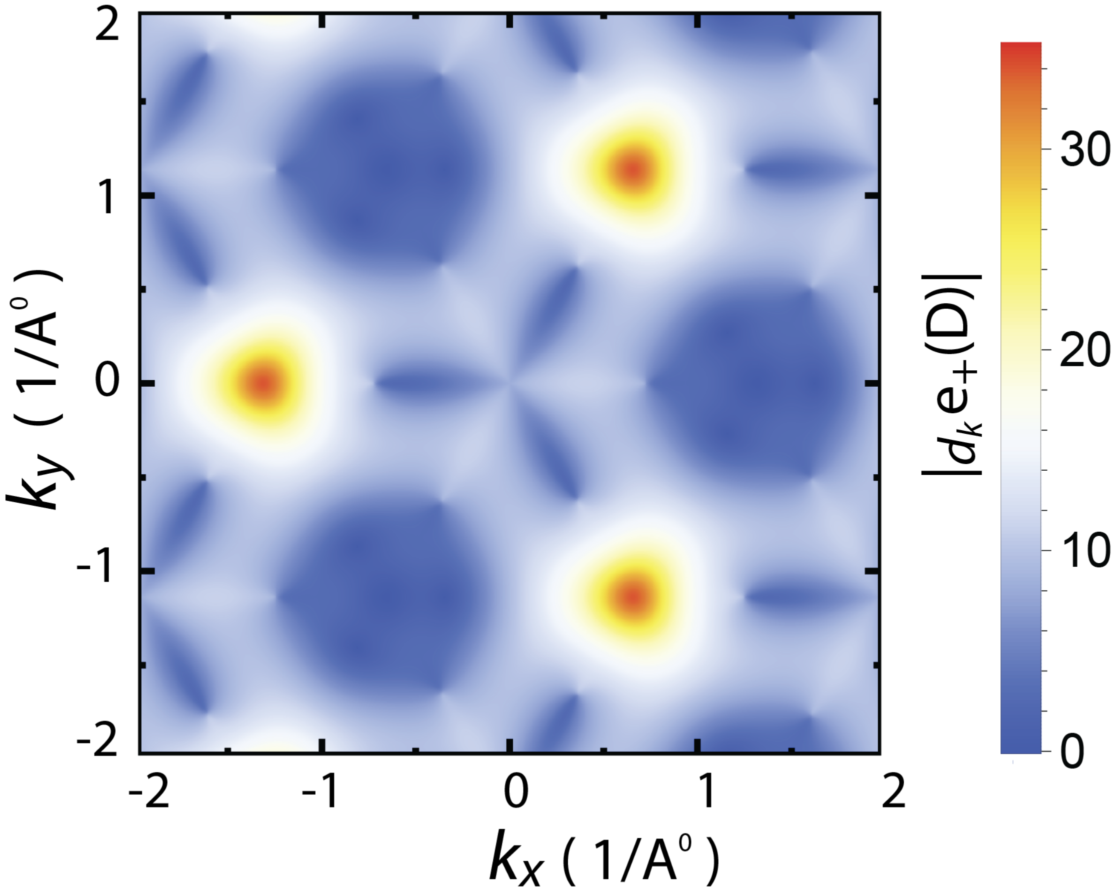

Figure 1.6 Absolute value of the left-rotating chiral dipole component, $\mathbf{d}_- = \mathbf{e}_+\mathbf{d}$, in MoS$_2$. It has maximum at K points.

1.6.2 Dye Molecule

A dye molecule is used as a gain in a TLS spaser system. The bandgap of the dye molecule lies in the range of a semi-conductor . It has a dipole moment of 1.7×10^{-18} esu(17 D). These molecules surround the metal sphere and the density of the chromophores is approximately $2 \times 10^{20}/\text{cm}^3$.

CHAPTER 2

Topological Nanospaser

2.1 Introduction

Spaser (surface plasmon amplificaiton by stimulated emission of radiation) was originally introduced in 2003 [3] as a nanoscopic phenomenon and device: a generator and amplifier of coherent nanolocalized optical fields. Since then, the science and technology of spasers experienced a rapid progress. Theoretical developments [16; 21–24] were followed by the first experimental observations of the spaser [25; 26] and then by an avalanch of new developments, designs, and applications. Currently there are spasers whose generation spans the entire optical spectrum, from the near-infrared to the near-ultraviolet [27–35].

Several types of spasers, which are synonymously called also nanolasers, have so far been well developed. Historically, the first is a nanoshell spaser [25] that contains a metal nanosphere as the plasmonic core that is surrounded by a dielectric shell containing gain material, typically dye molecules [5; 25]. Such spasers are smallest coherent generators produced so far, with sizes in the range of tens nanometers. Almost simultaneously, another type of nanolasers was demonstrated [26] that was built from a semiconductor gain nanorod situated over a surface of a plasmonic metal. It has a micrometer-scale size along the nanorod. Its modes are surface plasmon polaritons (SPPs) with nanometer-scale transverse size. Given that the spasers of this type are relatively efficient sources of far-field light, they are traditionally called nanolasers though an appropriate name would be polaritonic spasers. Later, this type of nanolasers (polaritonic spasers) was widely developed and perfected [27; 32; 36–39]. There are also spasers that are similar in design to the polaritonic nanolasers but are true nanospasers whose dimensions are all on the nanoscale. Such a spaser consists of a monocrystal nanorod of a semiconductor gain material deposited atop of a monocrystal nanofilm of a plasmonic metal [40]. These spasers possess very low thresholds and are tunable in all visible spectrum by changing the gain semiconductor composition while the geometry remains fixed [31; 41; 42]. There are also other types of demonstrated spasers. Among them we mention semiconductor-metal nanolasers [43] and polaritonic spasers with plasmonic cavities and quantum dot gain media [44].

A fundamentally different type of quantum generators is the lasing spaser [24; 45; 46]. A lasing spaser is a periodic array of individual spasers that interact in the near field and form a coherent collective mode. Such lasing spasers have been built of plasmonic crystals that incorporate gain media. One type of the lasing spasers is a periodic array of holes in a plasmonic metal film deposited on a semiconductor gain medium [30]; another type is a periodic array of metal nanoparticles surrounded by a dye molecules solution [47]. We have recently proposed a topological lasing spaser that is built of a honeycomb plasmonic crystal of silver nanoshells containing a gain medium inside [48]. The generating modes of such a spaser are chiral surface plsmons (SPs) with topological charges of $m = \pm 1$, which topologically protects them against mixing. Only one of the $m = \pm 1$ topologically-charged modes can generate at a time selected by a spontaneous breaking of the time-reversal symmetry.

The spasers are not only of a significant fundamental interest but also are promising for applications based on their nanoscale-size modes and high local fields. Among such demonstrated applications are those to sensing of minute amounts of chemical and biological agents in the environment [37; 38; 49]. Another class of the demonstrated applications of the spasers is that in cancer theranostics (therapeutics and diagnostics) [5]. An important

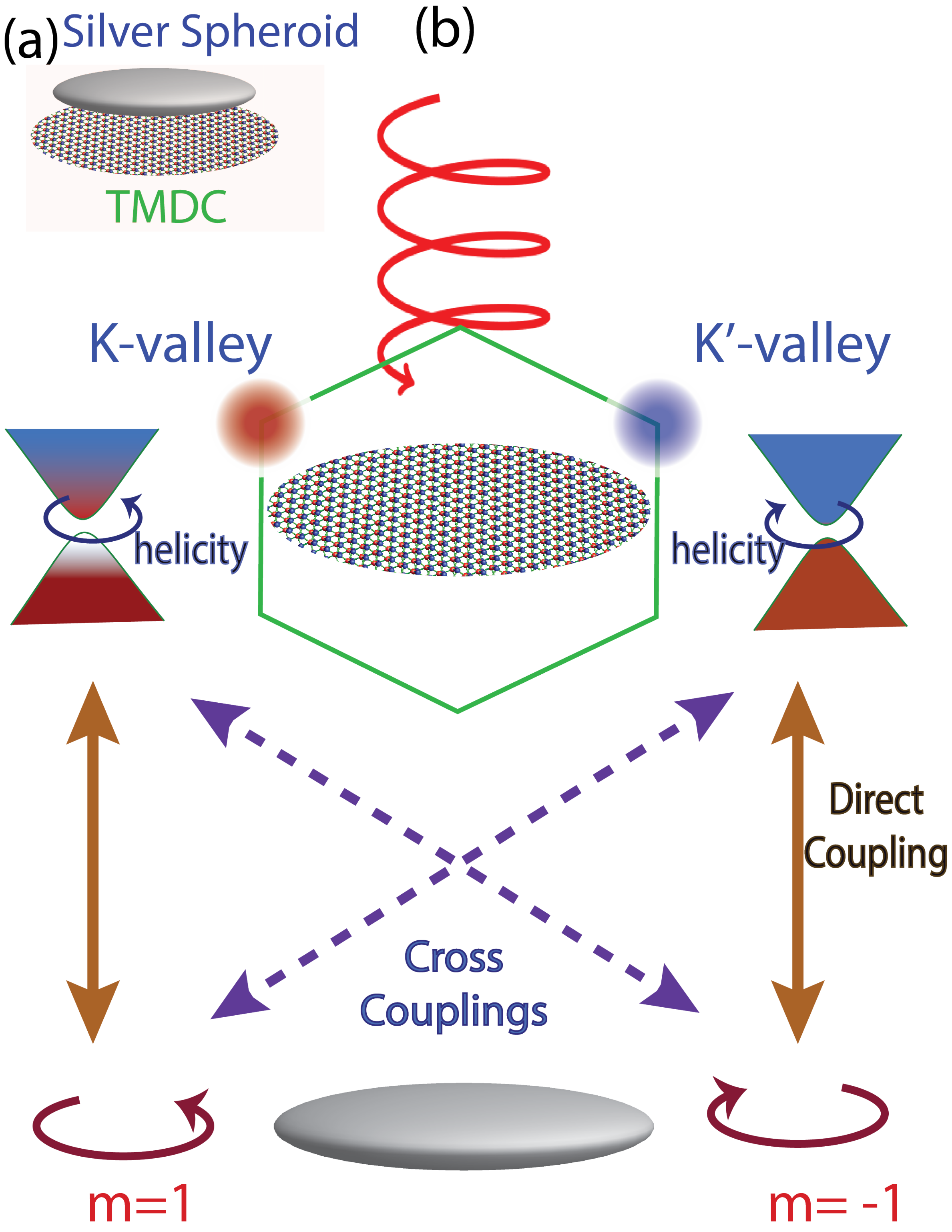

Figure 2.1 Schematics of the topological spaser. (a) Spaser consists of a silver nanospheroid placed on the top of TMDC nanoflake of a circular shape. The silver nanospheroid has oblate shape with radius 12 nm and height 1.2 nm. (b) Schematic of spaser operation. A circular-polarized light excites the valley with the chirality that match the light helicity. The metal nanospheroid supports two plasmon modes with azimuthal quantum numbers $m = -1$ and $m = 1$. The stimulated CB→VB transitions at the corresponding K or K′ points couple to these plasmon modes through direct and cross couplings.

perspective application of spasers is on-chip communications in optoelectronic information processing [50].

It is of a great interest to explore intersections of the spaser technology and topological physics. In our recently proposed topological lasing spaser [48], the topologically-charged eigenmodes stem from the Berry curvature [19; 51] of the plasmonic Bloch bands of a honeycomb plasmonic crystal of silver nanoshells. In contrast, the gain medium inside these nanoshells is completely achiral. This topological lasing spaser is predicted to generate a pair of mutually time-reversed eigenmodes carrying topological charges of ±1, which strongly compete with each other, so only one of them can be generated at a time.

In this Article we propose a topological nanospaser that also generates a pair of mutually time-reversed chiral SP eigenmodes with topological charges of ±1, whose fields are rotating in time in the opposite directions. In a contrast to [48], this proposed spaser is truly nanoscopic, with a radius ~ 10 nm. The topological charges (chiralities) of its eigenmodes originate from the Berry curvature of the gain-medium Bloch bands. This gain medium is a two-dimensional honeycomb nanocrystal of a transition metal dichalcogenide (TMDC) [52–54]. The plasmonic subsystem is an achiral nanodisk of a plasmonic metal. Note that previously the TMDCs have been used as the gain media of microlasers where the cavities were formed by microdisk resonators [55; 56] or a photonic crystal microcavity [57]. None of these lasers generated a chiral, topologically charged mode.

2.2 Spaser Structure and Main Equations

The geometry and the fundamentals of functioning of the proposed topological nanospaser is illustrated in Fig. 2.1. This spaser consists of a thin silver nano-spheroid placed atop of the two-dimensional (2d) gain medium (a nanodisk of a monolayer TMDC) – see Fig. 2.1(a). As panel (b) illustrates, the gain medium is pumped with circularly-polarized light, which is known to selectively populate one of the K or K' valleys depending on its helicity [58; 59]. Due to the axial symmetry, the plasmonic eigenmodes, $\phi(\mathbf{r})$, depend on the azimuthal angle, φ: $\phi_m(\mathbf{r}) \propto \exp\{(im\varphi)\}$, where $m = \text{const}$ is the magnetic quantum number. Figure 2.1(b) illustrates that the conduction band (CB) to valence band (VB) transitions in the TMDC couple predominantly to the SPs whose chirality matches that of the valley: the transitions in K- or K'-valley excite the $m = 1$ or $m = -1$ SPs, respectively.

The surface plasmon eigenmodes $\phi_n(\mathbf{r})$ are described by the quasistatic equation [15]

$$\nabla\Theta(\mathbf{r})\nabla\phi_n(\mathbf{r}) = s_n\nabla^2\phi_n(\mathbf{r}), \tag{2.1}$$

where n is a set of the quantum numbers defining the eigenmode, s_n is the corresponding eigenvalue, which is a real number between 0 and 1, and $\Theta(\mathbf{r})$ is the characteristic function, which is equal to 1 inside the metal and 0 outside. We assume that the metal nanoparticle is a spheroid whose eigenmodes can be found in oblate spheroidal coordinates [14] – see Chapter I (Sec. 1.5.1.1). They are characterized by two integer spheroidal quantum numbers: multipolarity $l = 1, 2, \ldots$ and azimuthal or magnetic quantum number $m = 0, \pm1, \ldots$. We will consider a dipolar mode, $l = 1$ where $m = 0, \pm1$. Note that the dipole transitions in the TMDC at the K-, K'-points are chiral, and they couple only to the modes with $m = \pm1$.

The Hamiltonian of the SPs is

$$H_{SP} = \hbar\omega_{\rm sp} \sum_{m=\pm 1} \hat{a}_m^\dagger \hat{a}_m, \tag{2.2}$$

where $\omega_{\rm sp}$ is the SP frequency, and $\hat{a}_m^\dagger$ and $\hat{a}_m$ are the SP creation and annihilation operators (we indicate only the magnetic quantum number m). The electric field operator is [3; 16]

$$\mathbf{F}_m(\mathbf{r}, t) = -A_{\rm sp}\nabla\phi_m(\mathbf{r})(\hat{a}_m e^{-i\omega_{\rm sp}t} + \hat{a}_m^\dagger e^{i\omega_{\rm sp}t}), \tag{2.3}$$

$$A_{\rm sp} = \sqrt{\frac{4\pi\hbar s_{\rm sp}}{\epsilon_d s'_{\rm sp}}}, \tag{2.4}$$

where $s'_{\rm sp} = {\rm Re}[ds(\omega)/d\omega|_{\omega=\omega_{\rm sp}}]$. The monolayer TMDC is coupled to the field of the SPs via the dipole interaction. We choose the proper thickness of the silver spheroid so that the SP energy $\hbar\omega_{\rm sp}$ is equal to the band gap of the TMDC gain medium. The Hamiltonian of the TMDC near the K or K' point can be written as

$$H_{\boldsymbol{\mathcal{K}}} = \int d^2\mathbf{q} \sum_{\alpha={\rm v,c}} E_\alpha(\boldsymbol{\mathcal{K}} + \mathbf{q})|\alpha, \boldsymbol{\mathcal{K}} + \mathbf{q}\rangle\langle\alpha, \boldsymbol{\mathcal{K}} + \mathbf{q}|, \tag{2.5}$$

where $\boldsymbol{\mathcal{K}} = K$ or K', and v and c stand for the valence band and the conduction band, correspondingly. We expand the Hamiltonian around the K and K' points as

$$H_{\boldsymbol{\mathcal{K}}} \simeq \nu_{\boldsymbol{\mathcal{K}}} \sum_{\alpha=c,\ v} E_\alpha(\boldsymbol{\mathcal{K}})|\alpha, \boldsymbol{\mathcal{K}}\rangle\langle\alpha, \boldsymbol{\mathcal{K}}|, \tag{2.6}$$

where $\nu_{\boldsymbol{\mathcal{K}}}$ is the density of electronic states in the $\boldsymbol{\mathcal{K}}$ valley, which we adopt from experimental data [55; 60]: $\nu_{\mathbf{K}} = \nu_{\mathbf{K}'} = 7.0 \times 10^{12}\ {\rm cm}^{-2}$.

The field of the SPs in nanoparticles is highly nonuniform in space, which gives rise to a spatial non-uniformity of the electron population of the TMDC monolayer. To treat this, we employ a semiclassical approach where the state $|\alpha, \boldsymbol{\mathcal{K}}, \mathbf{r}\rangle$ represents an electron in the $\boldsymbol{\mathcal{K}}$ valley at position $\mathbf{r}$. The corresponding Hamiltonian in the semiclassical approximation can be written as

$$H_{\boldsymbol{\mathcal{K}}} = \nu_{\boldsymbol{\mathcal{K}}} \sum_{\alpha=c,\ v} E_\alpha(\boldsymbol{\mathcal{K}}) \int d^2\mathbf{r} |\alpha, \boldsymbol{\mathcal{K}}, \mathbf{r}\rangle\langle\alpha, \boldsymbol{\mathcal{K}}, \mathbf{r}| \tag{2.7}$$

The interaction between the monolayer TMDC and the SPs is described by an interaction Hamiltonian

$$H_{int} = -\nu_{\mathbf{K}} \sum_{\boldsymbol{\mathcal{K}}=\mathbf{K},\mathbf{K}'} \int d^2\mathbf{r} \sum_{m=\pm1} \mathbf{F}_m(\mathbf{r}) \hat{\mathbf{d}}_{\boldsymbol{\mathcal{K}}}(\mathbf{r}) \ , \tag{2.8}$$

where the dipole operator is given by

$$\hat{\mathbf{d}}_{\boldsymbol{\mathcal{K}}}(\mathbf{r}) = \mathbf{d}_{\boldsymbol{\mathcal{K}}} e^{i\Delta_{\mathrm{g}} t} |c, \boldsymbol{\mathcal{K}}, \mathbf{r}\rangle\langle v, \boldsymbol{\mathcal{K}}, \mathbf{r}| + \text{h.c.} \ , \tag{2.9}$$

and $\hbar\Delta_{\mathrm{g}}$ is the band gap (at the K- or K'-point).

The transition dipole element, $\mathbf{d}_{\boldsymbol{\mathcal{K}}}$, is related to the non-Abelian (interband) Berry connection $\boldsymbol{\mathcal{A}}^{(\mathrm{cv})}(\mathbf{k})$ as

$$\begin{aligned} \mathbf{d}_{\boldsymbol{\mathcal{K}}} &= e\boldsymbol{\mathcal{A}}^{(\mathrm{cv})}(\mathbf{k}) \ , \\ \boldsymbol{\mathcal{A}}^{(\mathrm{cv})}(\mathbf{k}) &= i \left\langle u_{\mathrm{c}\mathbf{k}} \left| \frac{\partial}{\partial \mathbf{k}} \right| u_{\mathrm{v}\mathbf{k}} \right\rangle \Bigg|_{\mathbf{k}=\boldsymbol{\mathcal{K}}} \ , \end{aligned} \tag{2.10}$$

where $u_{\alpha\mathbf{k}}$ are the normalized lattice-periodic Bloch functions.

In this Article, we consider the dynamics of the system semiclassically: we treat the SP annihilation and creation operators as complex c-numbers, $\hat{a}_m = a_m$ and $\hat{a}_m^\dagger = a_m^*$, and describe the electron dynamics quantum mechanically by density matrix $\hat{\rho}_{\boldsymbol{\mathcal{K}}}(\mathbf{r}, t)$. Furthermore, we assume that the SP field amplitude is not too large, $\tilde{\Omega}_{m,\boldsymbol{\mathcal{K}}} \ll \Delta_{\mathrm{g}}$, where the Rabi frequency is defined by

$$\tilde{\Omega}_{m,\boldsymbol{\mathcal{K}}}(\mathbf{r}) = -\frac{1}{\hbar} A_{\mathrm{sp}} \nabla\phi_m(\mathbf{r}) \mathbf{d}_{\boldsymbol{\mathcal{K}}}^* \ . \tag{2.11}$$

Then we can employ the rotating wave approximation (RWA) [61; 62] where the density matrix can be written as

$$\hat{\rho}_{\boldsymbol{\mathcal{K}}}(\mathbf{r}, t) = \begin{pmatrix} \rho_{\boldsymbol{\mathcal{K}}}^{(\mathrm{c})}(\mathbf{r}, t) & \rho_{\boldsymbol{\mathcal{K}}}(\mathbf{r}, t) e^{i\omega t} \\ \rho_{\boldsymbol{\mathcal{K}}}^*(\mathbf{r}, t) e^{-i\omega t} & \rho_{\boldsymbol{\mathcal{K}}}^{(\mathrm{v})}(\mathbf{r}, t) \end{pmatrix} . \tag{2.12}$$

Following [16], the equations of motion of the SPs and the monolayer TMDC electron density matrix are

$$\begin{aligned} \dot{a}_m = {} & [i(\omega - \omega_{\mathrm{sp}}) - \gamma_{\mathrm{sp}}] a_m + \\ & i\nu_{\boldsymbol{\mathcal{K}}} \int_S d^2\mathbf{r} \sum_{\boldsymbol{\mathcal{K}}} \rho_{\boldsymbol{\mathcal{K}}}^*(\mathbf{r}) \tilde{\Omega}_{m,\boldsymbol{\mathcal{K}}}^*(\mathbf{r}) \ , \end{aligned} \tag{2.13}$$

$$\begin{aligned} \dot{n}_{\boldsymbol{\mathcal{K}}}(\mathbf{r}) = & -4 \sum_{m=1,-1} \mathrm{Im} \left[\rho_{\boldsymbol{\mathcal{K}}}(\mathbf{r}) \tilde{\Omega}_{m,\boldsymbol{\mathcal{K}}}(\mathbf{r}) a_m \right] + \\ & g_{\boldsymbol{\mathcal{K}}} \left[1 - n_{\boldsymbol{\mathcal{K}}}(\mathbf{r}) \right] - \gamma_{2\boldsymbol{\mathcal{K}}}(\mathbf{r}) \left[1 + n_{\boldsymbol{\mathcal{K}}}(\mathbf{r}) \right] , \end{aligned} \tag{2.14}$$

$$\dot{\rho}_{\boldsymbol{\mathcal{K}}}(\mathbf{r}) = [-i(\omega - \Delta_{\mathrm{g}}) - \Gamma_{12}]\rho_{\boldsymbol{\mathcal{K}}}(\mathbf{r}) + in_{\boldsymbol{\mathcal{K}}}(\mathbf{r}) \sum_{m=1,-1} \tilde{\Omega}^{*}_{m,\boldsymbol{\mathcal{K}}} a^{*}_{m} \ , \tag{2.15}$$

where S is the entire area of the TMDC, ω_{sp} is the SP frequency, γ_{sp} is the SP relaxation rate, Γ_{12} is the polarization relaxation rate for the spasing transition 2 → 1, $g_{\boldsymbol{\mathcal{K}}}$ is the pumping rate in valley $\boldsymbol{\mathcal{K}}$, the population inversion, $n_{\boldsymbol{\mathcal{K}}}$, is defined as

$$n_{\boldsymbol{\mathcal{K}}} \equiv \rho^{(\mathrm{c})}_{\boldsymbol{\mathcal{K}}} - \rho^{(\mathrm{v})}_{\boldsymbol{\mathcal{K}}} \ , \tag{2.16}$$

and the spontaneous emission rate of the SPs is [16]

$$\gamma_{2\boldsymbol{\mathcal{K}}}(\mathbf{r}) = \frac{2(\gamma_{\mathrm{sp}} + \Gamma_{12})}{(\omega_{\mathrm{sp}} + \Delta_{\mathrm{g}})^2 + (\gamma_{\mathrm{sp}} + \Gamma_{12})^2} \sum_{m=1,-1} \left| \tilde{\Omega}_{m,\boldsymbol{\mathcal{K}}}(\mathbf{r}) \right|^2 \tag{2.17}$$

2.3 Results and Discussion

2.3.1 Parameters of Spaser and Chiral Coupling to Gain Medium

We consider a spaser consisting of an oblate silver nanospheroid with semi-major axis $a =$ 12 nm placed atop of a circular TMDC flake whose radius is equal or greater to that of the nanospheroid. We assume that the system is embedded into a dielectric matrix with permittivity $\epsilon_{\mathrm{d}} = 2$. We choose the value of the semi-minor axis c (the height of the silver spheroid) to fit ω_{sp} to the K-point CV→VB transition frequency in the TMDC, $\omega_{\mathrm{sp}} = \Delta_{\mathrm{g}}$. We employ the three-band tight-binding model for monolayers of group-VIB TMDCs of Ref. [18]. We also set $\hbar\Gamma_{12} = 10$ meV.

From the tight-binding model, we calculate the band structure, including band gap Δ_{g}

and the transition dipole matrix element $\mathbf{d}$. Note that at the K- and K'-points, the band gaps are the same, $\Delta_{\mathrm{g}}(\mathbf{K}) = \Delta_{\mathrm{g}}(\mathbf{K}')$, while the transition dipole matrix elements are complex conjugated, $\mathbf{d}_{\mathbf{K}} = \mathbf{d}^{*}_{\mathbf{K}'}$, as protected by the $\mathcal{T}$-symmetry. The values used in the computations are listed in Table 1.1. Here we give an example for MoS_2: $c = 1.2$ nm; $\hbar\Delta_{\mathrm{g}} = 1.66$ eV; $\mathbf{d}_{\mathbf{K}} = 17.7\ \mathbf{e}_{+}$ D, and $\mathbf{d}_{\mathbf{K}'} = 17.7\ \mathbf{e}_{-}$ D, where $\mathbf{e}_{\pm} = (\mathbf{e}_x \pm i\mathbf{e}_y)/\sqrt{2}$ are the chiral unit vectors.

There are two modes with the opposite chiralities, $m = \pm 1$, and identical frequencies, ω_{sp}, which are time-reversed with respect to each other, whose wave functions are $\nabla\phi \propto e^{\pm i\varphi}$. In the center of the TMDC patch, i.e., at $\mathbf{r} = 0$, the point symmetry group of a metal nanospheroid on the TMDC is C_{3v}. It contains a C_3 symmetry operation, i.e., a rotation in the TMDC plane by an angle $\varphi = \pm 2\pi/3$, which brings about a chiral selection rule $m = 1$ for the K-point and $m = -1$ for the K'-point, i.e., the chirality of the SPs matches that of the valley. For eccentric positions, which are not too far from $\mathbf{r} = 0$, this selection rule is not exact but still there is a preference for the chirally-matched SPs.We assume that the pumping is performed with the circularly polarized radiation, and one of the valleys, say the K valley, is predominantly populated. Consequently, the first mode that can go into generation is the $m = 1$ SP.

The dynamics of the spaser is completely determined by the coupling of plasmonic excitations characterized by the Rabi frequency, $\tilde{\Omega}_{m,\mathcal{K}}(\mathbf{r})$, which is a function of the radius vector, $\mathbf{r}$, within TMDC nanoflake and also depends on the type of the plasmon, $m = 1$ or $m = -1$, and the valley of TMDC, K or K'. The real and imaginary parts of $\tilde{\Omega}_{m,\mathcal{K}}(\mathbf{r})$ are shown in Fig. 2.2 for different combinations of m and TMDC valley. The radius of metal nanospheroid, which is 12 nm in the x-y plane, determines two different dependences

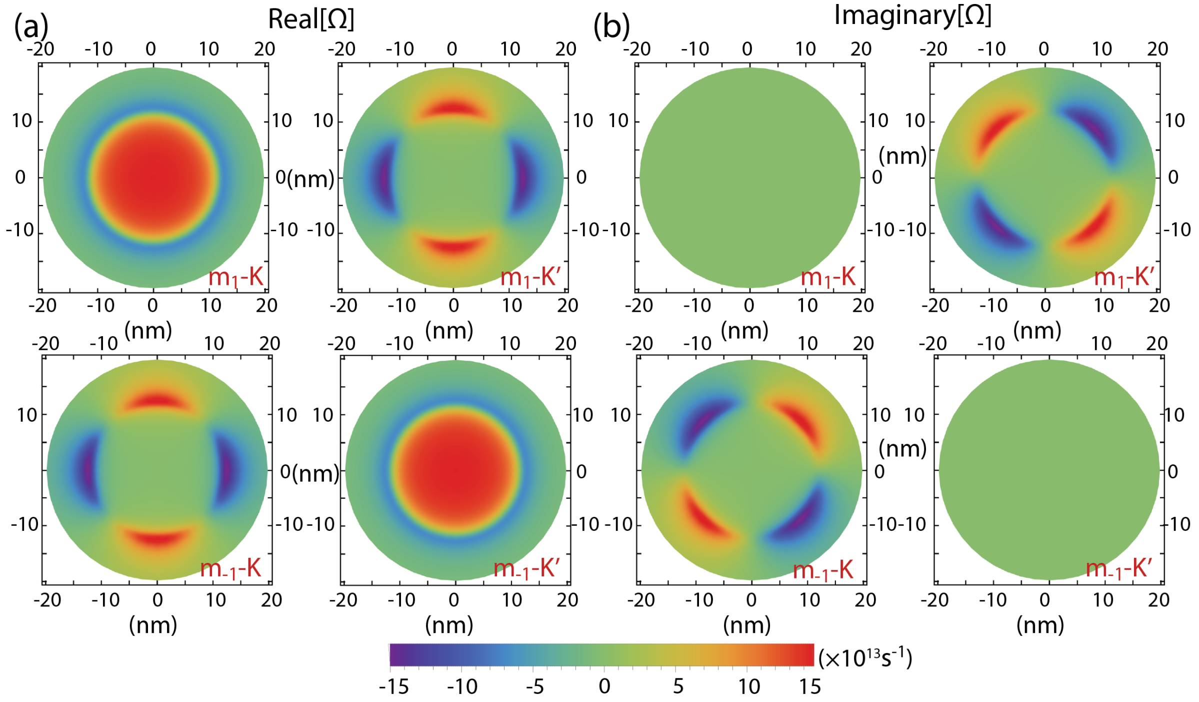

Figure 2.2 The real part (a) and imaginary part (b) of the Rabi frequency. The Rabi frequency determines the coupling of the plasmon mode m and the K or K' valleys of TMDC. The radius of the metal spheroid is $a = 12$ nm.

of $\tilde{\Omega}_{m,\boldsymbol{\mathcal{K}}}(\mathbf{r})$. If $r < 12$ nm, then the Rabi frequency, both it's real and imaginary parts, is an isotropic function of radius. It mainly follows the "angular momentum" selection rule, i.e., $m = 1$ is coupled to the K valley, while $m = -1$ is coupled to the K' valley. This selection is exact at $r = 0$, but for $r > 0$ it is a good approximation.

For $r > 12$ nm, i.e., a point is outside the metal nanospheroid in the x-y plane, the plasmonic electric field has a dipole nature. As a result, $\tilde{\Omega}_{m,\boldsymbol{\mathcal{K}}}(\mathbf{r})$ behaves completely differently. Namely, both $\tilde{\Omega}_{m=1,K'}$ and $\tilde{\Omega}_{m=-1,K}$ are large, while $\tilde{\Omega}_{m=-1,K'}$ and $\tilde{\Omega}_{m=1,K}$ are small. Also, because of the dipole nature of the plasmonic electric field, the Rabi frequency acquires strong angular dependence of type $\exp(2i\varphi)$ - see Fig. 2.2, where φ is the polar in-plane angle.

Thus, from the properties of the Rabi frequency, we can conclude that if the radius of TMDC nanoflake is less than 12 nm, then $m = 1$ plasmon mode is mainly coupled to the TMDC valley of the same chirality, i.e, the K valley, while $m = -1$ plasmon mode - to the K' valley. But if the radius of TMDC is greater than 12 nm, then $m = 1$ and $m = -1$ plasmon modes are coupled to both K and K' valleys. The larger the radius of the TMDC flake, the stronger the coupling of the plasmonic mode to the TMDC valley of opposite chirality.

The chiral optical fields generated by the topological spaser are not stationary – they evolve in time rotating clockwise for $m = 1$, as illustrated in Fig. 2.3, and counterclockwise for $m = -1$. The magnitude of the field is large even for one SP per mode, $|\mathbf{E}| \sim 10^7$ V/Å, which is a general property of the nanospasers related to the nanoscopic size of the mode. Note that with increase of the SP population, the field increases as $|\mathbf{E}| \propto \sqrt{N_m}$.

Below in this Article, we provide numerical examples of the spaser kinetics. For certainty, we assume that the K-valley is selectively pumped, which can be done with the right-hand circularly polarized pump radiation. (As protected by the $\mathcal{T}$-symmetry, exactly the same results are valid for the left-handed pump and the K'-valley.) Thus, we set $g_K = g$ and $g_{K'} = 0$.

Below we discuss the dependencies of the LSPs in spasing modes, $m = 1$ and $m = -1$, with respect to the applied rate of pumping g. In this, we solve the system of Eqs. (2.13)-(2.15) with the given initial conditions, which are $N_{m=1} = |a_1|^2 = 9$ ($a_1 = 3$), i.e., there are nine $m = 1$ plasmons, and the conduction band populations of both K and K' valley are zero. The two cases we discuss are of i) the radius of TMDC flake equal to the radius of the nanospheroid and, ii) the radius of TMDC flake greater than that of the radius of the nanospheroid:

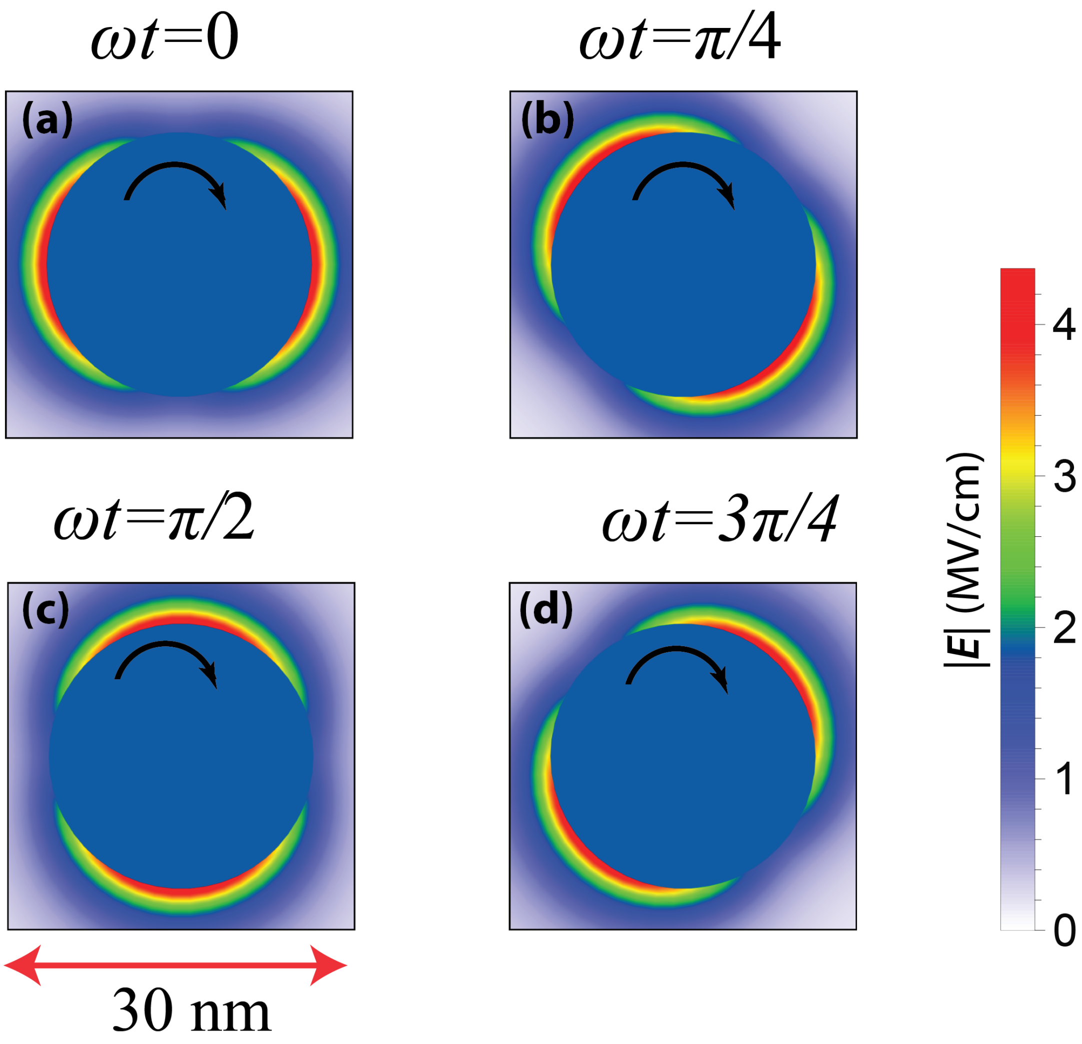

Figure 2.3 Temporal dynamics of the local electric field, $|\mathbf{E}|$, in topological spaser generating in the $m = 1$ mode. The curved arrow indicates the rotation direction of the field (clockwise). The magnitude of the field is calculated for a single SP per mode, $N_m = 1$; it is color-coded by the bar to the right. The phase of the spaser oscillation is indicated at the top of the corresponding panels.

2.3.2 Radius of TMDC Equal to the Nanospheroid

Below we explain the properties of a topological nanospaser when the radius of the TMDC flake is equal to the radius of the Nanospheroid. We will focus on the description of a continuous wave solution, dynamics and far-field radiation.

2.3.2.1 Kinetics of Continuous-Wave Spasing

A continuous wave (CW) solution can be obtained by solving Eqs. (2.13)-(2.15) where the time derivatives in the left-hand sides are set to zero.The calculated dependences of the generated coherent SP population, $N_m = |a_m|^2$ where $m = \pm 1$, on the pumping rate, g, for various TMDC's are shown in Fig. 2.4(a). As we can see, there is a single spasing threshold for each of the TMDCs. Significantly above the threshold, for $g_{\mathcal{K}} > 30$ ps^{-1}, the number of SPs, N_m, grows linearly with pumping rate g. This is a common general property of all spasers: it stems from the fact that the feedback in the spasers is very strong due to the extremely small modal volume. Therefore, the stimulated emission dominates the electronic transitions between the spasing levels, which is a prerequisite of the linear dependence $N_m(g)$. The slope of this straight line (the so-called slope efficiency) is specific for every given TMDC.

We have verified that the mismatched mode ($m = -1$) does not have a finite threshold, i.e., it is not generated at any pumping rate. The reason is that the matched mode ($m = 1$) above its threshold clamps the inversion at a constant level [16] preventing its increase with the pumping and, thus, precluding the generation of the mismatched mode. In this case, the single chiral mode generation enjoys a strong topological protection.

At the threshold, the spasing curves experience a bifurcation behavior. This is clearly seen in the magnified plot in Fig. 2.4(b): there is the threshold as the bifurcation point and two branches of the spasing curve above it. As we see from Fig. 2.4(c), these two branches differ by the stationary values of population inversion $n_{\boldsymbol{K}}$: for the upper branch it is significantly lower than for the lower branch. To answer a question whether these two branches are stable, we slightly perturb the accurate numerical solutions at $g = 25$ ps^{-1} by

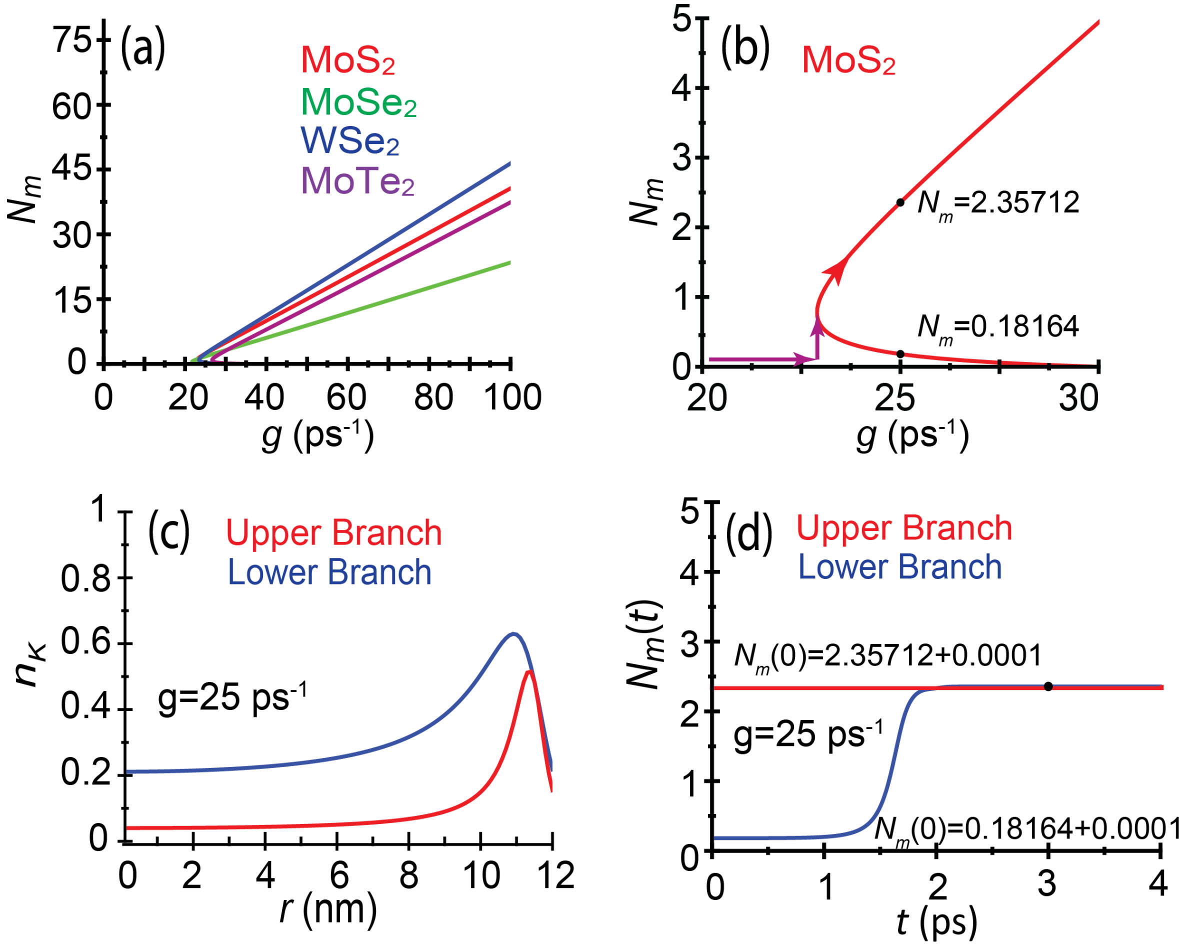

Figure 2.4 Spaser kinetics. (a) Dependence of the number of SP quanta in the spasing mode on the pumping rate for gain medium of the matched radius, $R_g = a = 12$ nm. Only the chirality-matched SP with $m = 1$ are generated. (b) Magnified near-threshold portion of panel (a) for MoS$_2$. The number of the SPs, N_m, is indicated for the points shown on the graphs for the two branches. (c) Radial distribution of the inversion, n_k for each of the two branches. (d) Test of stability of the two SP branches. The kinetics of the SP population, N_m, after the number of the SPs in each branch is increased by $\Delta N_m = 0.0001$.

changing the number of SPs by a minuscule amount, $\Delta N_m = 0.0001$. The density matrix solution for the dynamics of the SP population induced by such a perturbation is shown in Fig. 2.4(d). As we see, the upper branch is absolutely stable but the lower branch is unstable, and it evolves in time towards the upper branch within less than half a picosecond. As a result of this bifurcation instability, the system actually evolves with the increase of pumping

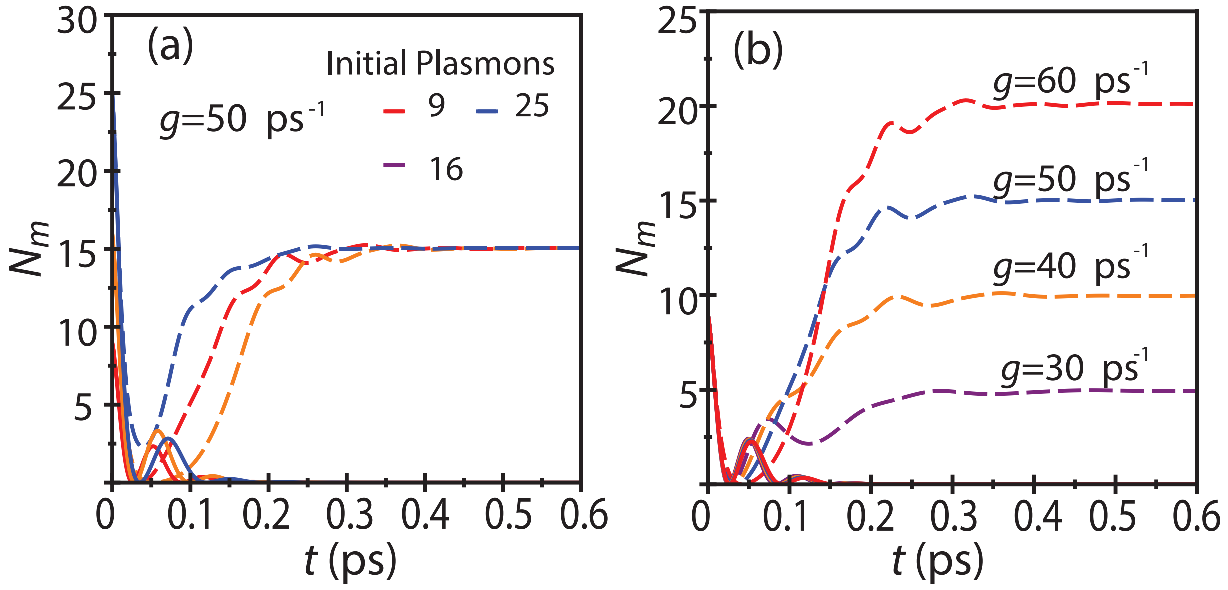

Figure 2.5 Number of SPs N_m as a function of time t for a spaser with MoS_2 as a gain material. The pumping is performed by a radiation whose electric field rotates clockwise in the plane of system ($m = 1$). The solid lines denote the chiral SPs with $m = -1$, and the dashed lines denote the SPs with $m = 1$. The pumping rates are indicated in the panels. (a) Dependence of SP number N_m on time t after the beginning of the pumping for different initial SP populations (color coded as indicated) for pumping rate $g = 50\ \mathrm{ps}^{-1}$. (b) Dependence of SP number N_m on time t for different pumping rates g (color coded). The initial SP number is $N_m = 10$.

along a path indicated by arrows in Fig. 2.4(b): Below the threshold, the population of the coherent SPs $N_m = 0$; it jumps to the apex of the curve at the bifurcation point and then follows the upper branch. One can state that the spatial inhomogeneity of the field and the inversion cause the spasing transition to become the first order. This is in contrast to the previous homogeneous case of Ref. [16] where this transition was continuous, i.e., of the second order.

2.3.2.2 Stability and Topological Protection of Spaser Modes

In Fig. 2.5(a), we test the stability and topological protection of the spasing mode. Panel (a) displays the dynamics of the SP population of the topological spaser, $N_m(t)$, for different initial numbers of SPs, $N_m(0)$, and for their different chiralities, $m = \pm 1$. As these data show, the left-rotating SPs ($m = -1$) are not amplified irrespectively of their initial numbers: the corresponding curves evolve with decaying relaxation oscillations tending to $N_{-1} = 0$. In contrast, the $m = 1$ SPs exhibit a stable amplification: their number increases to a level that is defined by the pumping rate, g, and does not depend on the initial populations. The $m = 1$ chirality SP-amplification stability with respect to the injection of the $m = -1$ quanta, which these data demonstrate, is due to the topological protection: matching the phase windings of the SP mode and the electronic states in the pumped K-valley. Although the selective coupling of electron states of TMDC and plasmonic modes of nanospheroid is due to chirality of electron states, such chirality is inherent to the systems with nontrivial topology like TMDC. Namely, any system with nontrivial topology is chiral. At the same time, the topology plays an important role in protecting such chiral states from perturbations and long-range disorder. Such topological protection also strongly suppresses the coupling of states with opposite chirality. In the case of TMDC, there are the states of K and K' valleys. Thus, the nontrivial topology of TMDC results in topologically protected chiral electron states that are selectively coupled to plasmonic modes of nanospheroid.

As a complementary test, we show in Fig. 2.5(b) the temporal dynamics of the SP population for equal initial number of SPs but different pumping rates. The dynamics in this case is again stable with the mismatched $m = -1$ SPs decaying to zero, and the matched

$m = 1$ being amplified to the stable levels that linearly increase with the pumping rate.

2.3.2.3 Far-Field Radiation of Spaser

The spaser is a subwavelength device design to generate intense, coherent nanolocalized fields. Generation of far-field radiation is not its primary function. However, the proposed spaser, as most existing nanospasers, generates in a dipolar mode that will emit in the far field. This emission, in absolute terms, can be quite intense for a nanosource. In particular, the spaser emission was used to detect cancer cells in the blood flow model [5]; it was, actually, many orders of magnitude brighter than from any other label for biomedical detection.

To describe the spaser emission, we note that the radiating dipole uniformly rotates with the angular velocity of $\omega_{\rm sp}$. The emitted radiation will be right-hand circularly polarized for the pumping at the K point and left-hand circularly polarized for the K' pumping. Note that the corresponding two radiating modes are completely uncoupled. This is equivalent to having two independent chiral spasers in one.

To find the intensity, I, of the emitted radiation, we need to calculated the radiating dipole. To do so, we will follow Ref. [63]. We take into account that the modal field, $\mathbf{E}_m = \nabla\phi_m$, inside the metal spheroid is constant. Then from Eq. (1.25) in Chapter I, we can find

$$E_m^2 = \frac{s_{\rm sp}}{V_{\rm m}} \ , \tag{2.18}$$

where $V_{\rm m}$ is the spheroid's volume. The physical field squared inside the metal is found from Eqs. (2.3) and (2.4),

$$F_m^2 = \frac{4\pi\hbar s_{\rm sp}^2 N_m}{\epsilon_{\rm d} s'_{\rm sp} V_m} \ . \tag{2.19}$$

From this, we find the radiating dipole squared as

$$|d_{0\mathrm{p}}|^2 = \frac{\hbar}{4\pi}\left(\mathrm{Re}\frac{\partial\epsilon_\mathrm{m}(\omega_\mathrm{sp})}{\partial\omega_\mathrm{sp}}\right)^{-1}\mathrm{Re}\left[\epsilon_\mathrm{m}(\omega_\mathrm{sp})-\epsilon_\mathrm{d}\right]^2 V_\mathrm{m} N_m \ . \tag{2.20}$$

The dipole radiation rate (photons per second) can be found from a standard dipole-radiation formula [64] as

$$\begin{aligned} I \ &= \ \frac{4}{9}\left(\frac{\omega}{c_0}\right)^3 (\epsilon_\mathrm{d})^{1/2}\,\mathrm{Re}\left[\epsilon_\mathrm{m}(\omega_\mathrm{sp})-\epsilon_\mathrm{d}\right]^2 \times \\ &\left(\mathrm{Re}\frac{\partial\epsilon_\mathrm{m}(\omega_\mathrm{sp})}{\partial\omega_\mathrm{sp}}\right)^{-1} a^2 c N_m \ , \end{aligned} \tag{2.21}$$

where c_0 is speed of light in vacuum.

For our example of $\mathrm{MoS_2}$, substituting parameters that we used everywhere in our calculations (see Sec. 2.3.1), we obtain

$$I = 2.1\times 10^{12} N_m\ \mathrm{s}^{-1}; \quad P = \hbar\omega_\mathrm{sp} I = 0.55 N_m\ \mu\mathrm{W}\ , \tag{2.22}$$

where P is the power of the emission. From these numbers, we conclude that the emission is extremely bright for a nano-emitter and easily detectable. This is in line with the observation of the emission from single spasers of the comparable size in Ref. [5].

2.3.3 Radius of TMDC Greater than the Nanospheroid

In this section we will, mostly, discuss the effects of the coupling for the TMDC flake of size greater than the radius of the nanospheroid. Here, we use numerical approach to solve the equations Eqs. (2.13)-(2.15). The section primarily focuses on the study of threshold behavior for different radius of gain at different pumping rate g.

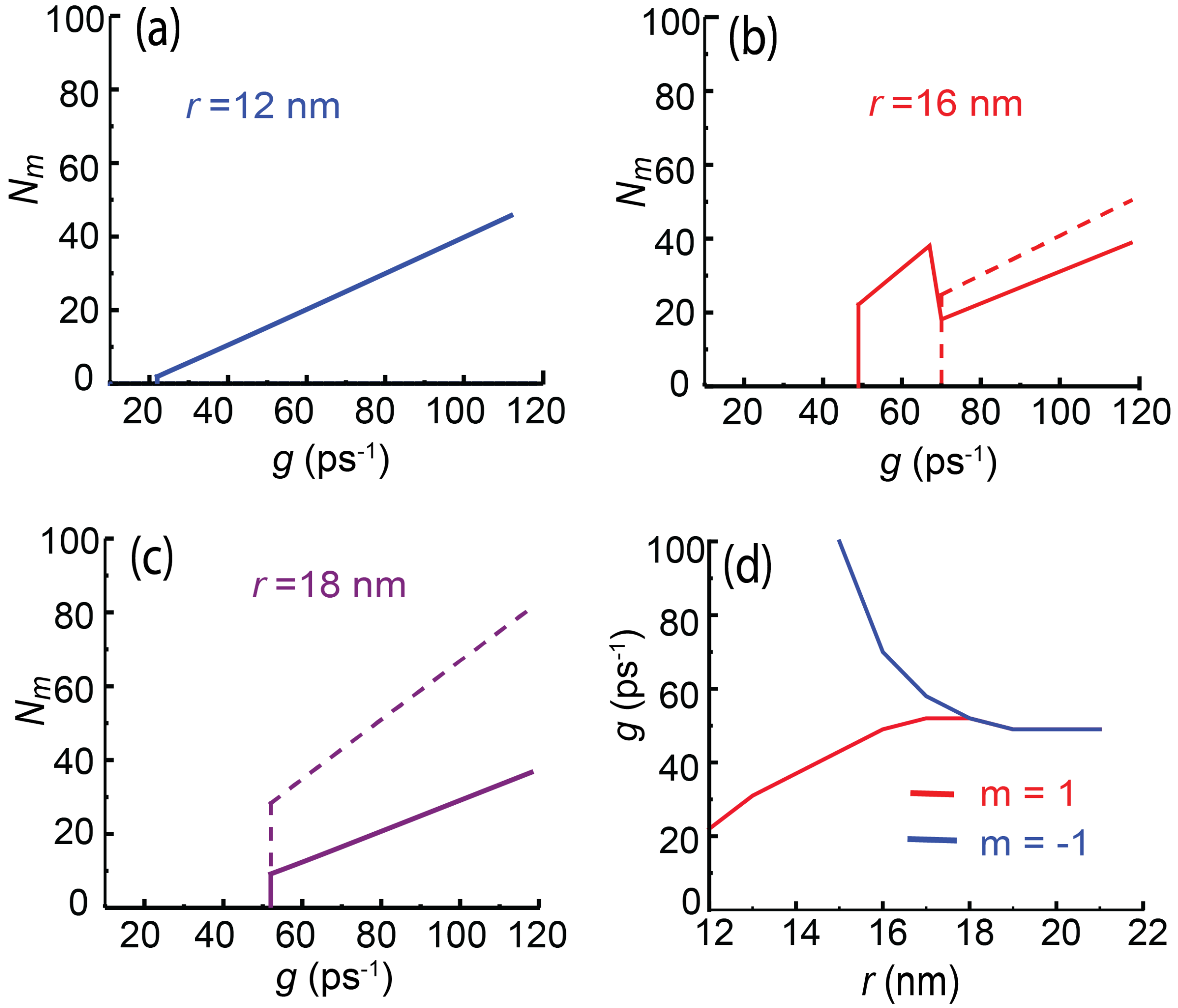

Figure 2.6 (a)-(c) Number of plasmons, N_m, as a function of gain, g. The solid and dashed lines correspond to the plasmons with $m = 1$ and $m = -1$, respectively. The radius of TMDC nanoflake is (a) 12 nm, (b) 16 nm, and (c) 18 nm. (d) The topological spaser thresholds as a function of radius of TMDC nanoflake. If $g_{th,2} > g > g_{th,1}$ then only $m = 1$ plasmon mode exists in the stationary regime, while if $g > g_{th,2}$ then both modes $m = 1$ and $m = -1$ are generated.

2.3.3.1 The Kinetics of a Topological Nanospaser: Threshold Behavior and Effects of Population Inversion

The number of plasmons, $N_m = |a_m|^2$, as a function gain, g, is shown in Fig. 2.6 (a)-(c) for three different radii of TMDC nanoflake. The solid and dashed lines correspond to $m = 1$

and $m = -1$ plasmons, respectively. If $r = 12$ nm then only co-rotating ($m = 1$) plasmon mode, i.e., the mode that is strongly coupled to the excited K valley, is generated. There is a characteristic spaser threshold, $g_{th} \approx 20\ ps^{-1}$, when the plasmon mode starts generating.

For a larger radius, $r = 16$ nm, see Fig. 2.6(b), the system show different behavior. Now, the K valley is coupled to both co-rotating $m = 1$ and counter-rotating $m = -1$ modes (although the coupling to the counter-rotating mode is still relatively weak). There are two thresholds, $g_{th,1}$ and $g_{th,2}$. At lower threshold, $g_{th,1} \approx 49\ ps^{-1}$, only one mode, $m = 1$, is generated, while at larger threshold, $g_{th,2} \approx 70\ ps^{-1}$, both plasmon modes, $m = 1$ and $m = -1$, cogenerated. At the second threshold the energy is transferred from the $m = 1$ mode to $m = -1$ mode so the number of $m = 1$ plasmons decreases. Another unique feature of the second regime, $g > g_{tr,2}$, is that there are more counter-rotating plasmons than the co-rotating ones, $N_{-1} > N_1$.

The corresponding solutions for N_{-1} and N_1 give an idea of why there are more counter-rotating plasmons than the co-rotating ones. Namely, the numbers of generated plasmons are effectively proportional to the areas of TMDC nanoflake with large coupling to the corresponding plasmonic modes and they do not depend on the magnitude of the coupling as long as the system is above the threshold. Thus, the number of co-rotating plasmons is proportional to πr_0^2, where $r_0 \approx 11$ nm and for $r < r_0$ the co-rotating mode is strongly coupled to the K valley, while the number of counter-rotating plasmons is proportional to $\pi(r_1^2 - r_0^2)$, where r_1 is the radius of TMDC nanoflake and the counter-rotating mode is strongly coupled to the K valley of TMDC at $r_1 > r > r_0$. Then $N_{-1} > N_1$ if $r_1 > \sqrt{2} r_0 \approx 16$ nm.

When the radius of the TMDC nanoflake increases even more, $r = 18$ nm, two thresholds,

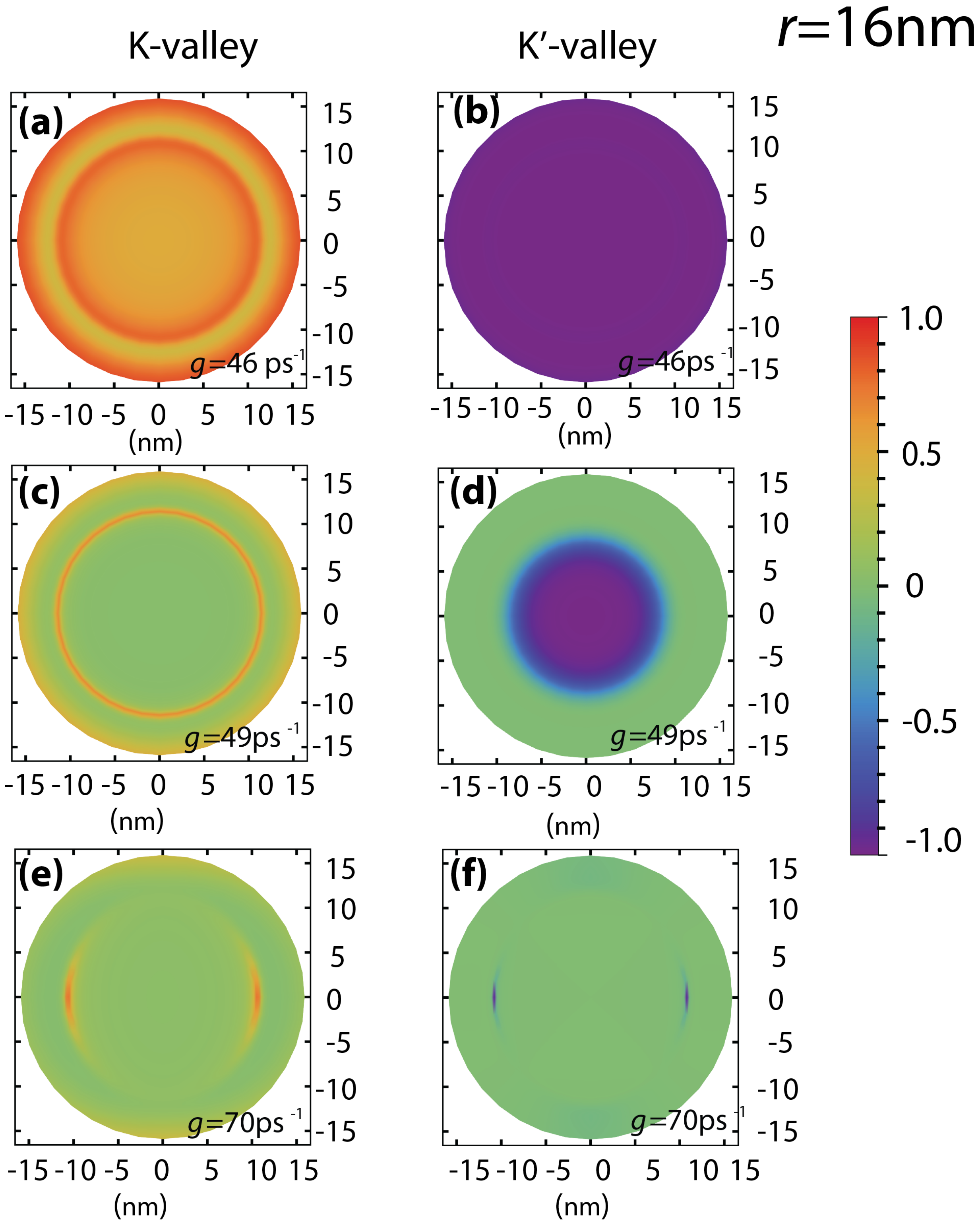

Figure 2.7 Inversion population of K and K' valleys of $\mathrm{MoS_2}$ nanoflake with the radius of 16 nm. The gain is (a),(b) 46 ps^{-1}, (c),(d) 49 ps^{-1}, and (e),(f) 70 ps^{-1}. The panels (a), (c), and (e) correspond to the K valley, while the panels (b), (d), and (f) describe the K' valley.

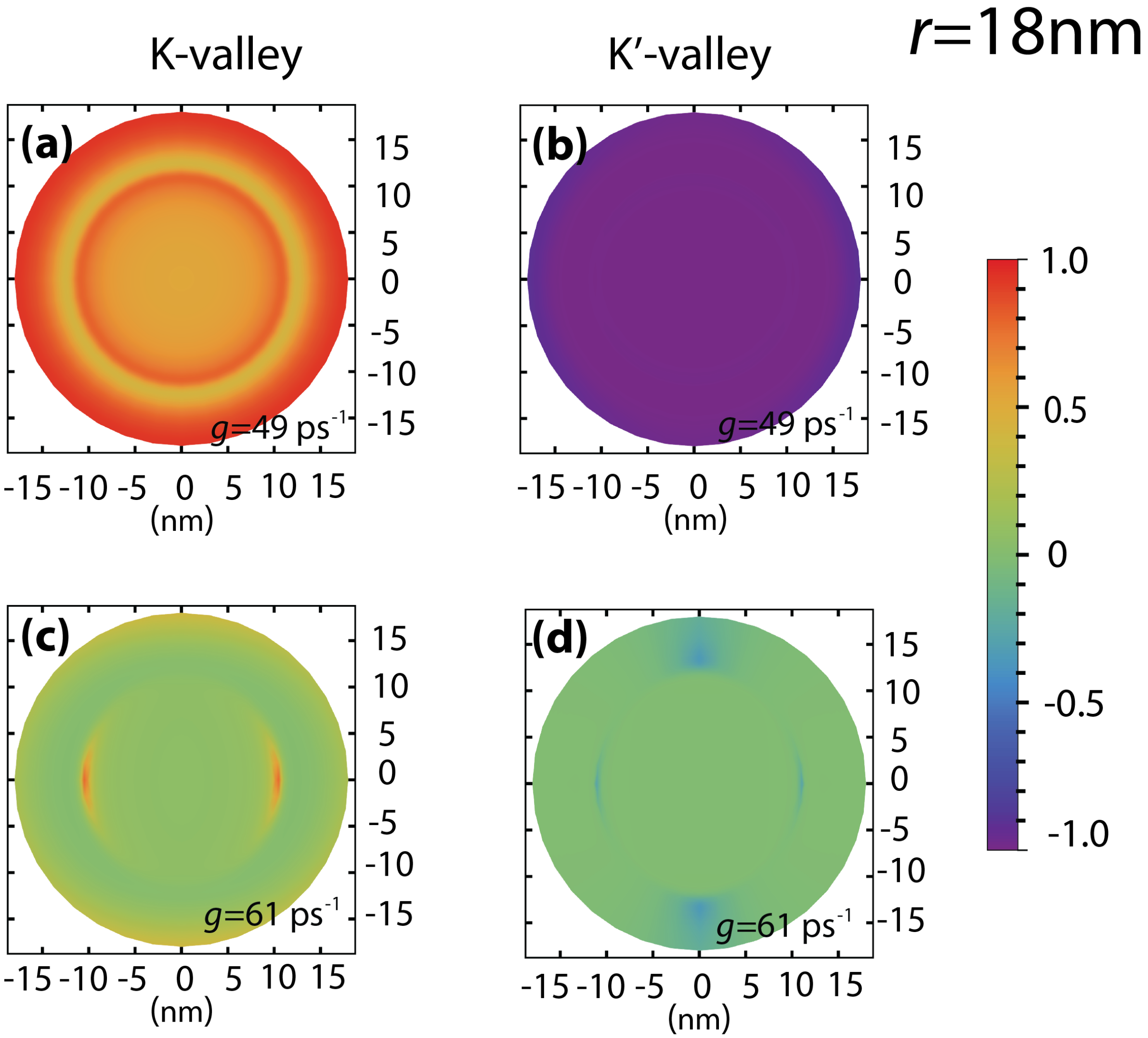

Figure 2.8 Inversion population of K and K' valleys of $\mathrm{MoS_2}$ nanoflake with the radius of 18 nm. The gain is (a),(b) 49 ps^{-1} and (c),(d) 61 ps^{-1}. The panels (a), (c) correspond to the K valley, while the panels (b), (d) describe the K' valley.

$g_{th,1}$ and $g_{th,2}$, merge into a single one, $g_{th,1} = g_{th,2} \approx 52\ ps^{-1}$, at which two plasmon modes are generated simultaneously - see Fig. 2.6(c). Similar to a smaller radius, the number of counter-rotating plasmons is more than the number of co-rotating ones. The dependence of two thresholds, $g_{th,1}$ and $g_{th,2}$, on the TMDC radius, r, is shown in Fig. 2.6(d). At $r \lesssim 15$ nm, there is only one spaser regime when only co-rotating mode is generated. At

$15nm \lesssim r \lesssim 17nm$ there are two thresholds and the system can generate either one plasmon mode, $m = 1$, or two plasmons modes, $m = 1$ and $m = -1$, depending on the gain, g. At $r > 17$ nm, two thresholds merge into a single one and there is only one regime with two generated plasmon modes.

To illustrate different regimes of spaser dynamics, we show in Fig. 2.7 the distributions of the population inversions at the K and K' valleys for the radius of TMDC flake of 16 nm and different values of gain. If the gain is less than the first threshold, $g < g_{th,1}$, then no plasmons are generated and the population inversion of the K valley is close to one, while the population inversion of the K' valley is exactly -1, i.e., the valence band is completely occupied and the conduction band is empty. This case is shown in Fig. 2.7(a)-(b).

In Fig. 2.7(c)-(d) the gain is greater than $g_{th,1}$ but less than $g_{th,2}$. In this case, only one plasmon mode, $m = 1$, is generated. The distribution of population inversion is isotropic and it is close to zero for $r < 12$ nm for the K valley and for $r > 12$ nm for the K' valley, which illustrates strong coupling of these spatial regions to the $m = 1$ mode -see also Fig. 2.2.

Another possibility, when the gain is greater than $g_{th,2}$, is shown in Fig. 2.7(e)-(f). Under this condition, both $m = 1$ and $m = -1$ plasmon modes are generated. They are coupled to both valleys at all spatial regions ($r < 12$ nm and $r > 12$ nm), as a result, the population inversions for both K and K' valleys are close to zero. Because of the coexistence of two plasmon modes, the resulting electric field shows interference features, and the corresponding population inversion distribution is anisotropic - see Fig. 2.7(c)-(d).

The large radius of TMDC nanoflake, $r = 18$ nm, is illustrated in Fig. 2.8. In this case there is only one threshold. If the gain is less than the threshold, see Fig. 2.8(a)-(b), then no

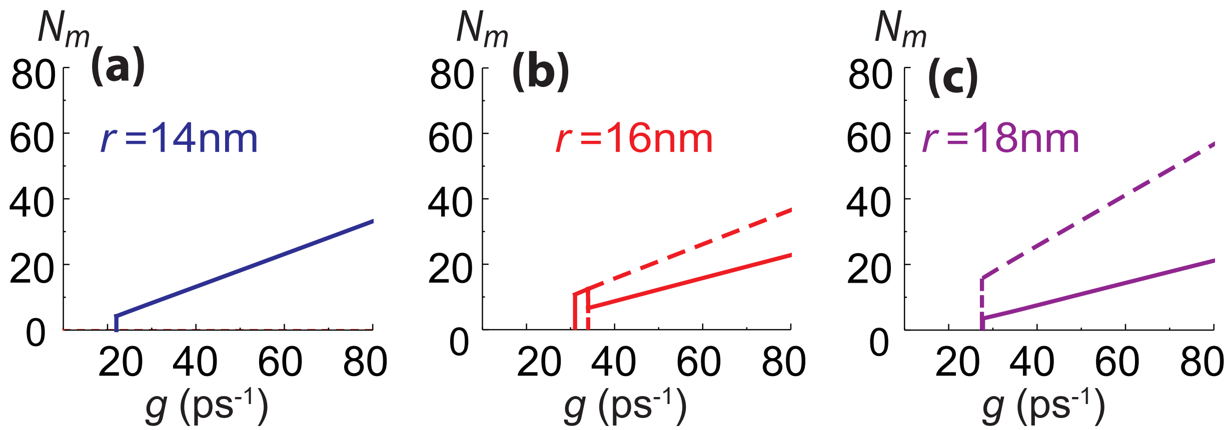

Figure 2.9 (a)-(c) Number of plasmons, N_m, as a function of gain, g in the dielectric environment with the constant of $\epsilon_d = 3.5$. The parameters of the nanospheroid are $a = 12nm$ and $c = 2.185nm$. The solid and dashed lines correspond to $m = 1$ and $m = -1$ plasmons, respectively. The radius of TMDC nanoflake is (a) 14 nm, (b) 16 nm, and (c) 18 nm.

plasmons are generated and the conduction band of the K valley is highly populated, while the population inversion of the K' valley is -1 at all spatial points. If the gain is greater than the threshold, see Fig. 2.8(c)-(d), then two plasmon modes, $m = -1$ and $m = 1$, are generated. The population inversion is close to zero for both K and K' valleys. The population inversion distribution is also anisotropic, which is due to the interference of the plasmonic fields of two modes.

To illustrate that the existence of three different regimes of operating of topological nanospaser is a generic property and does not depend on specific parameters of the system, we show in Figs. 2.9 and 2.10 two-threshold behavior for different nanospaser systems. The parameters of the system are adjusted in a such way that the plasmonic frequency is equal to the transition frequency, ω_{21}, of the MoS$_2$ monolayer. We change the dielectric constant of the surrounding media to $\epsilon_d = 3.5$ and consider two different sizes of the metal nanospheroid: $a = 12nm$ and $c = 2.185nm$ in Fig. 2.9 and $a = 16nm$ and $c = 2.890nm$ in Fig. 2.10. The

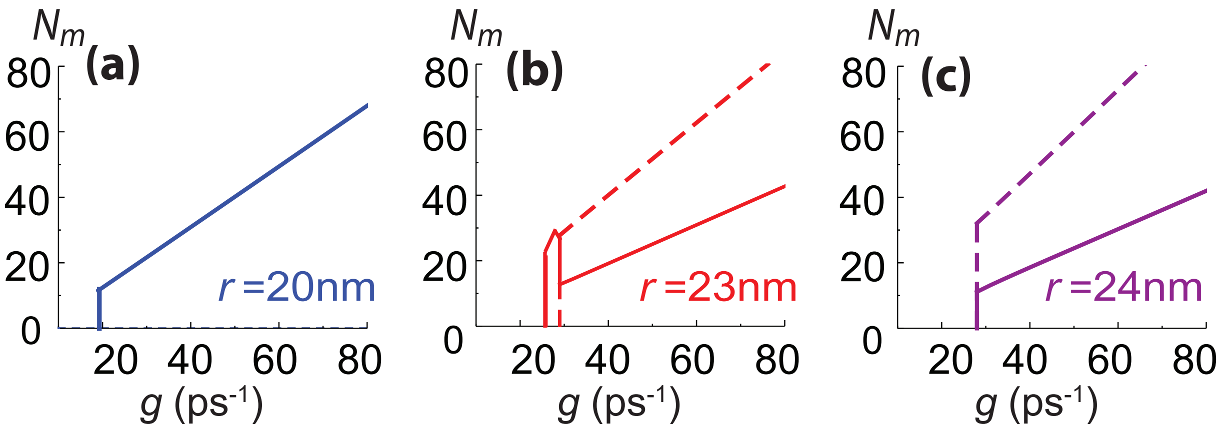

Figure 2.10 (a)-(c) Number of plasmons, N_m, as a function of gain, g in the dielectric environment with the constant of $\epsilon_d = 3.5$. The parameters of the nanospheroid are $a = 16nm$ and $c = 2.890nm$. The solid and dashed lines correspond to $m = 1$ and $m = -1$ plasmons, respectively. The radius of TMDC nanoflake is (a) 20nm, (b)23 nm, and (c) 24 nm.

sizes of nanospheroid are defined by the condition that the plasmon frequency is equal to ω_{21}. In both cases, with increasing the size of TMDC nanopatch, we can clearly see the transitions from one threshold dynamics when only $m = 1$ mode is generated to two threshold regime, and finally to one threshold regime again when two plasmon modes, $m = 1$ and $m = -1$, are generated. The radii when these transitions occur are correlated with the size of TMDC nanopatch.

In the above analysis we assumed that only the K valley is pumped by a circularly polarized light, i.e., $g_K = g$ and $g_{K'} = 0$. If the handedness of the pulse is changed to an opposite one, then only the K' valley will be pumped ($g_K = 0$ and $g_{K'} = g$) and the new results will be identical to what we obtained above but with the interchange of $m = 1$ and $m = -1$ plasmons, so that the $m = -1$ plasmons will be co-rotating and the $m = 1$ plasmons - counter-rotating ones.

2.3.3.2 Temporal Dynamics of a Topological Nanospaser

The temporal dynamics of the topological spaser is shown in Fig. 2.11. The initial number of plasmons is nine for both modes, $m = 1$ and $m = -1$. In Fig. 2.11(a), the gain is fixed, $g = 82\ ps^{-1}$, and the results are shown for different radii of TMDC nanoflake. For all parameters, the number of plasmons, N_1 and N_{-1}, show similar initial dynamics (at $t \lesssim 0.15$ ps). Namely, first, both N_1 and N_{-1} sharply decrease to almost zero values, then show small oscillations and finally monotonically increase to the stationary values. At the stationary stage, for small radius of TMDC nanoflake, $r = 14$ nm, only $m = 1$ is generated, while for large radius, $r = 16$ nm or $r = 18$ nm, both modes, $m = 1$ and $m = -1$, are generated - see Fig. 2.11(a).

This property is also illustrated in Fig. 2.11(b), in which the radius is fixed, $r = 16$ nm, and the gain is varied. For $g = 50\ ps^{-1}$ and $g = 60\ ps^{-1}$, which are less then the second threshold, only $m = 1$ plasmons are generated in the stationary regime. For larger gain, $g = 70\ ps^{-1}$, mode $m = -1$ coexists with $m = 1$ plasmonic mode.

In the regimes when two plasmonic modes are generated, the relative phases of the generated modes, $m = -1$ and $m = 1$, are equal to the initial relative phases. For example, if the initial values of a_1 and a_{-1} are real with zero phase difference, then the stationary values of a_1 and a_{-1} are also real with zero relative phase.

2.3.3.3 Far-Field Radiation

Although it is not its primary role, the topological nanolaser can be used as a miniature source of far-field radiation, which is due to the oscillating electric dipole of the spaser system. The induced electric dipole moment of the system is the sum of two contributions: the dipole

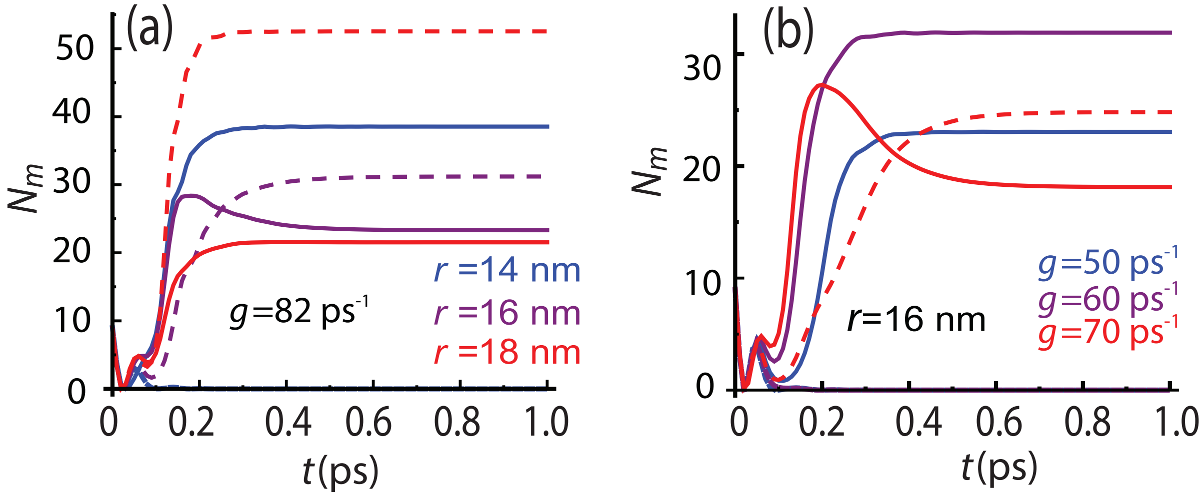

Figure 2.11 The number of surface plasmons, N_m, as a function of time t for topological spaser with MoS$_2$ nanoflake as a gain medium. The solid and dashed lines correspond to $m = 1$ and $m = -1$ plasmons, respectively. The initial number of plasmons is $N_1 = N_{-1} = 9$. (a) The gain is $g = 82\ ps^{-1}$ and the radii of TMDC nanoflake are 14 nm, 16 nm, and 18 nm. The corresponding lines are shown by different colors as marked in the panel. (b) The radius of TMDC nanoflake is 16 nm and the gain is 50 ps^{-1}, 60 ps^{-1}, and 70 ps^{-1}. The corresponding lines are shown by different colors as marked in the panel.

moment of TMDC nanoflake, $\mathbf{d_{tmdc}}$, and the dipole moment of the metal nanospheroid, $\mathbf{d_{metal}}$,

$$\mathbf{d_{total}} = \mathbf{d_{tmdc}} + \mathbf{d_{metal}}. \tag{2.23}$$

The dipole moment of TMDC nanoflake can be expressed in terms of the non-diagonal part of the density matrix of TMDC system

$$\begin{aligned}\mathbf{d_{tmdc}} &= \sum_{\mathcal{K}=\mathbf{K},\mathbf{K'}} (\rho_{\mathcal{K}} \mathbf{d}_{\mathcal{K}} e^{i\omega t} + \rho^*_{\mathcal{K}} \mathbf{d}^*_{\mathcal{K}} e^{-i\omega t}) \\ &= (\rho_{\mathbf{K}} \mathbf{d_K} + \rho_{\mathbf{K'}} \mathbf{d_{K'}}) e^{i\omega t} + (\rho^*_{\mathbf{K}} \mathbf{d}^*_{\mathbf{K}} \\ &\quad + \rho^*_{\mathbf{K'}} \mathbf{d}^*_{\mathbf{K'}}) e^{-i\omega t}.\end{aligned} \tag{2.24}$$

The dipole moment of the metal nanospheroid can be found from the known electric field [see Eq. (3.6)] inside the metal,

$$\mathbf{d_{metal}} = \int_V \frac{\mathrm{Re}[\epsilon_{metal} - \epsilon_d]}{4\pi} \mathbf{F_m}(\mathbf{r}, \mathbf{t})\, \mathbf{dr}. \tag{2.25}$$

Here the integral is calculated over the volume of the nanospheroid. The electric field, $\mathbf{F_m}(\mathbf{r}, \mathbf{t})$, inside the metal depends on the number of $m = 1$ and $m = -1$ plasmons.

The x and y components of the total dipole moment, which is the sum of Eqs. (42) and (2.25), can be expressed in the following forms

$$\mathbf{d_{total,x}} = \mathrm{B}_1 e^{i\omega t} + \tilde{\mathrm{B}_1} e^{-i\omega t}, \tag{2.26}$$

$$\mathbf{d_{total,y}} = \mathrm{C}_1 e^{i\omega t} + \tilde{\mathrm{C}_1} e^{-i\omega t}, \tag{2.27}$$

where,

$$\mathrm{B}_1 = -\kappa \mathrm{A_{sp}} \mathrm{E_0} \mathrm{V}(\hat{a}_1^* + \hat{a}_{-1}^*) + \mathrm{f}_{\mathbf{K}} \mathrm{d}_0 + \mathrm{f}_{\mathbf{K'}} \mathrm{d}_0, \tag{2.28}$$

$$\mathrm{C}_1 = i\kappa \mathrm{A_{sp}} \mathrm{E_0} \mathrm{V}(\hat{a}_1^* - \hat{a}_{-1}^*) + i\mathrm{f}_{\mathbf{K}} \mathrm{d}_0 - i\mathrm{f}_{\mathbf{K'}} \mathrm{d}_0, \tag{2.29}$$

$$\kappa = \frac{\mathrm{Re}[\epsilon_{metal} - \epsilon_d]}{4\pi} \tag{2.30}$$

$$\mathrm{f}_{\mathbf{K}} = -\nu \sum_{\mathrm{S}} \frac{i n_{\mathbf{K}}(\mathbf{r}) \sum_{m=1,-1} \tilde{\Omega}^*_{m,\mathbf{K}} a^*_m}{-(\omega - \Delta_{\mathrm{g}}) + i\Gamma_{12}}, \tag{2.31}$$

$$\mathrm{f}_{\mathbf{K}'} = -\nu \sum_{\mathrm{S}} \frac{i n_{\mathbf{K}'}(\mathbf{r}) \sum_{m=1,-1} \tilde{\Omega}^*_{m,\mathbf{K}'} a^*_m}{-(\omega - \Delta_{\mathrm{g}}) + i\Gamma_{12}}, \tag{2.32}$$

$$\mathbf{d}_{\mathbf{K}} = \mathrm{d}_0 \mathbf{e}_+ \ \ \& \ \ \mathbf{d}_{\mathbf{K}'} = \mathrm{d}_0 \mathbf{e}_-. \tag{2.33}$$

The derivation of Eqs. (2.28)- (2.32) is given in the Appendix Section (B). The main contribution to the total dipole moment comes from the metal nanospheroid, for which the corresponding dipole moment is almost two order of magnitude larger than the dipole moment of TMDC nanoflake.

The components of the dipole radiated field are proportional to the total dipole moment, $E_x \propto \mathbf{d}_{\mathbf{total,x}}$, $E_y \propto \mathbf{d}_{\mathbf{total,y}}$. The corresponding polarization ellipse is shown in Fig. 2.12 for two regimes of operation of the topological spaser: (a) only one $m = 1$ plasmon mode is generated and (b) two modes, $m = 1$ and $m = -1$, are cogenerated. For case (a), the far field radiation is left circularly polarized, which is the same polarization as the one of the pump light. This is consistent with the condition that only one plasmon mode is generated in this case.

If two plasmon modes are generated [Fig. 2.12(b)], then the corresponding polarization ellipse describes the right elliptically polarized radiation. Note, that the pump light is left circularly polarized. The change of the handedness of polarization from left to right is due to the fact that the number of $m = -1$ plasmons is greater than the number of $m = 1$ plasmons in the continuous wave regime of the spaser.

Thus, for a given radius of TMDC nanoflake, by changing the gain, i.e., the intensity of the circularly polarized light, we can switch the handedness of the far-field radiation from

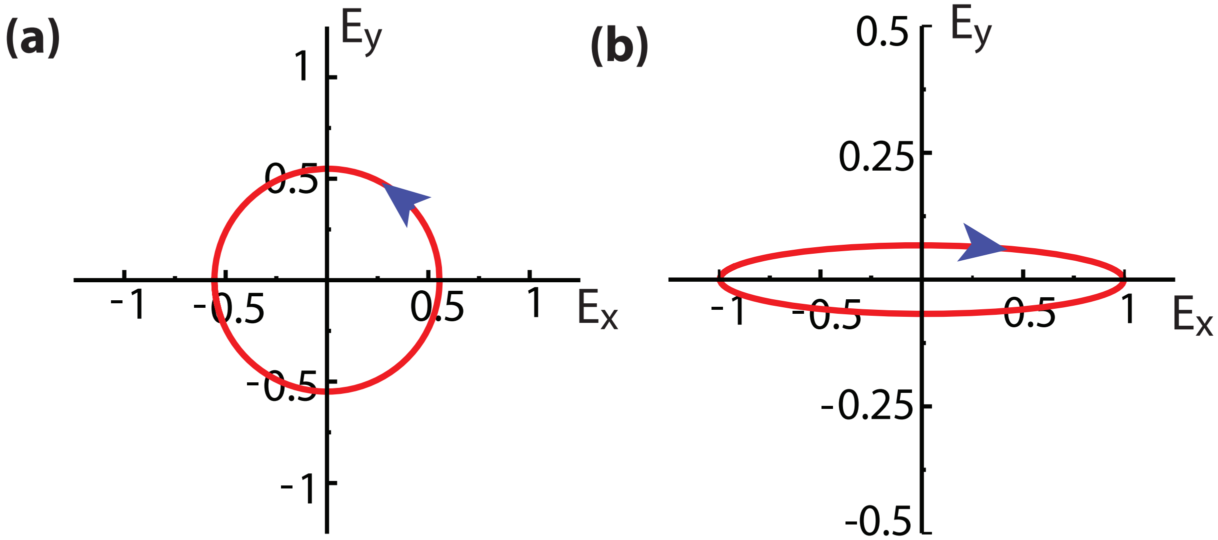

Figure 2.12 Polarization ellipse of the far field radiation of topological spaser for its two regimes of continuous wave operation. (a) Radius of TMDC nanoflake is 16 nm and the gain is 49 ps^{-1}. Only $m = 1$ plasmon mode is generated. The far field radiation is left circularly polarized. (b) Radius of TMDC nanoflake is 16 nm and the gain is 70 ps^{-1}. Two plasmon modes, $m = 1$ and $m = -1$ are generated. The far field radiation is right elliptically polarized. The electric field is shown in arbitrary units.

left to right and vica versa. For example, if $g_{th_1} < g < g_{th_2}$ then the far field radiation is left circularly polarized, but if $g_{th_2} < g$ then it is right elliptically polarized.

2.4 Conclusion

A topological nanospaser of type II consists of two main components: a metal nanospheroid and a TMDC, e.g., MoS$_2$, monolayer flake of a circular shape. The nanospheroid functions as a plasmonic nanoresonator with two relevant plasmonic modes, which rotate in the opposite directions and are characterized by azimuthal quantum numbers $m = \pm 1$. The MoS$_2$ monolayer is a gain medium with nontrivial topology. It is placed atop of a nanospheroid and has two chiral *valleys*, K and K'. The system is pumped by a circular polarized light, which populates the conduction band states of only one valley, say the K valley.

Such topological spaser has been theoretically proposed in Ref. [65]. In the present paper, we show that it has very rich dynamics, which strongly depends on the radius of the gain medium (TMDC nanoflake). If the radius of TMDC is small, then the K and K' valleys are mainly coupled to the co-rotating plasmonic modes, e.g., the K valley is coupled to the $m = 1$ mode. In this case the nanospaser has one threshold, g_{th}, so that if the gain is larger than g_{th} then the co-rotating plasmon mode is generated. For larger radius of nanoflake, the valleys of TMDC become also strongly coupled to the counter-rotating modes, and the nanospaser has two thresholds, $g_{th,1}$ and $g_{th,2}$, so that if $g_{th,2} > g > g_{th,1}$ then only the co-rotating mode is generated, while if $g > g_{th,2}$ then both co-rotating and counter-rotating modes are generated. For an even larger radius of TMDC, the two thresholds merge into one and the nanospaser has only one regime when two modes, $m = 1$ and $m = -1$, are cogenerated. In this case, the number of counter-rotating plasmons is larger than the number of co-rotating ones. Because of that property the far-field radiation of nanospaser shows interesting behavior. Namely, by changing the gain strength, one can change the handedness of the far-field radiation from left to right and vice versa.

All these unique properties of topological nanospaser make it an extremely viable option for several nanoscopic applications. Main areas are near-field spectroscopy and sensing where a plasmon frequency of a nanospaser can be tuned to work at the required condition. However, the topological nanospaser can also be used in optical interconnects and probing. Another key area is the biomedical one where similar systems have been previously adopted [5; 66] for the diagnosis and therapeutics of cancer. With added topoligical chiral benefits, this nanolaser can be more effective in such detection. In addition to all these, the topological nanospaser has also a potential as an excellent far-field radiation source.

CHAPTER 3

Three-level Spaser System: a Semi-Classical Analysis

3.1 Introduction

Scaling down electronic and optical systems to harness their optimum efficiency has been a goal of today's scientific and industrial research. Among the research fields, working in this direction, nanoplasmonics plays an important role due to its unique possibilities and broad applications [67–69]. In nanoplasmonics, the light is confined within a sub-wavelength scale, which results in a strong enhancement of the optical field. Some of the notable application of nanoplasmonics are in the areas of near-field optics [70; 71], bio-sensing [72–74], surface plasmon-based photo-detectors [75; 76], spaser[77–79] and many others. Spaser (surface plasmon amplification by stimulated emission of radiation), which has experienced a vast development over the last decade, plays a special role in this list. It was introduced in the early 2000's [3] by David. J. Bergman and Mark. I . Stockman [80; 81], and throughout the time has paved its way up as a miniature source of spectrally tunable stimulated emission [16; 21]. Apart from the mainstream research, spaser has found numerous applications in different areas such as opto-electronic systems[50; 82–88], sensing in biological and chemical agents[89–91] and also as a biological probe[5; 66] in disease therapeutics and diagnostics.

The whole idea of spaser is based on the existence of localized surface plasmons, which are characterized by a high concentration of optical energy within a nanoscale range[92]. Such strong concentration of optical field combined with stimulated emission [3] process allow to design a nanoscale laser - spaser. Different variations of such nanoscopic lasers were proposed theoretically and realized experimentally. The first of the type[93] was introduced

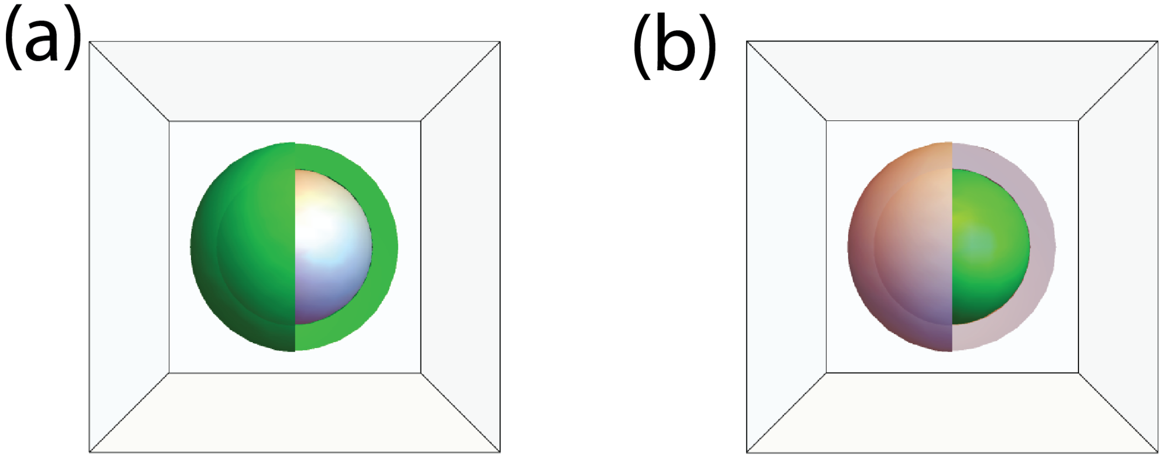

Figure 3.1 Schematic illustration of two geometries of spaser: (a) a metal nanosphere surrounded by a gain medium (shown by green) (b) a gain medium placed inside a metal nanoshell.

in 2008 and was based on an array of plasmonic resonators. A year later, a spaser, based on Localized Surface Plasmons Resonance[94; 95](LSPR), was demonstrated experimentally[25], which contained a gold sphere embedded inside a dye. The same design has been also been studied for a cancer diagnosis and treatment by Ganzala et al[5] in 2017

The design of spaser based on a gain nanorod placed near plasmonic metal with the dimensions in micrometers has been considered in Ref. [96; 97]. Recently, the topological spasers of type I and II were introduced[48; 65; 98], where the spaser dynamics is protected by nontrivial topological properties of either a plasmonic system[48] or a gain medium[65; 98].

Spaser can be understood as a nanoplasmonic counterpart of a normal laser[99]. It consists of two major components: a metal resonator and a gain medium. Usually, the metal is silver due to its low non-radiative losses, however, gold or aluminum can also be used for the spaser operating at high frequency. The gain medium is usually dye molecules, with the gap close to the SP frequency. Apart from dyes, materials[18; 100; 101] with non-linear effects that exhibit topological resonance, have also been studied as a suitable gain. Additionally, the system may also be placed in an appropriate dielectric environment, which can be used to adjust the SP frequency of a nanosphere.

The two basic possibilities of how a gain medium can be introduced into a spaser system are shown in Fig. 3.1: i) gain encapsulating the solid nanosphere ii) gain placed inside a metal nanoshell. Below, we consider only the first case when the gain is placed outside the solid silver metal nanosphere as shown in Fig. 3.1a. Additionally, this system is placed in water which will further help to adjust the LSP frequency(ω_{sp}).

Theoretical modeling[16] of such nanolaser[25] is mostly in agreement with the experimental results, apart from the behavior of the spaser at a large value of electric pumping. In the present paper, we are using the same theoretical model[16] of spaser with some modifications, which can address the unexplained behavior. Namely, we consider a three-level model for the gain while in Ref. [16] only two levels were introduced for the gain medium.

3.2 Model and Main Equations

We consider a gain medium consisting of three energy levels with the corresponding populations n_0, n_1 and n_2. This approach is similar to the previously studied 2-level [16] system, but with an additional energy level added to account for the finite relaxation rate of electron population from the highest level to the second excited level. Many other noticeable works have been done previously to deal with the effects of multi-level[102; 103] on the spasing process. However, this paper describes an elegant way to account for coherent processes in gain, which makes our findings in close appropriation with the experimental ones as discussed

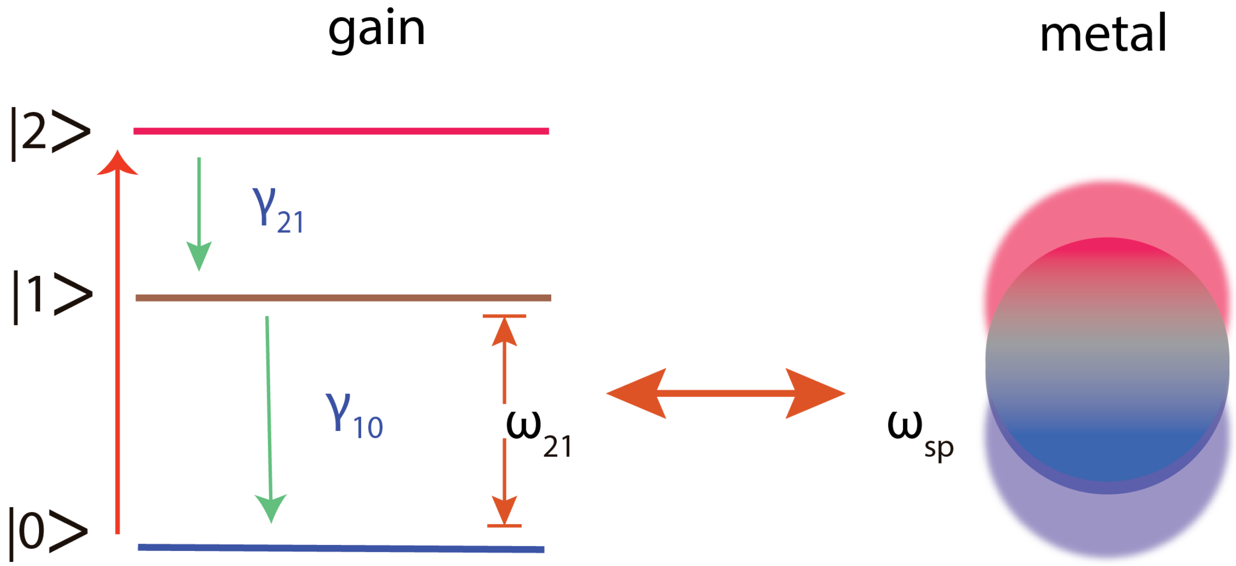

Figure 3.2 Schematics of energy levels of dye (gain medium) and a silver sphere. Here, $|0>$, $|1>$, and $|2>$ are the three levels of the dye (gain) with the corresponding populations n_1, n_2 and n_2. External laser pulse pumps the system and excites the gain medium from the ground state $|0>$ to the second excited one $|2>$. The corresponding transition is shown by red arrow. The gain system is also characterized by the relaxation processes: from level $|2>$ to level $|1>$ with the rate γ_{21} and from level $|1>$ to level $|0>$ with the rate γ_{10}. The frequency of the plasmonic dipole mode of the metal nanosphere is ω_{sp}. This mode is coupled to the inter-level transition $|1>\rightarrow|0>$ with the frequency $\omega_{10} \approx \omega_{sp}$.

below. The general schematics of transition within the system is shown in Fig. 3.2.

The gain system is pumped by an external light, which excites the system from the ground state $|0>$ to the second excited state $|2>$ with the transition (gain) rate g. The excited states of the system are also characterized by relaxation rates γ_{21} and γ_{10}, which represent the transitions $|2>\rightarrow|1>$ and $|1>\rightarrow|0>$ respectively. The gain medium is coupled to the plasmonic system through the field-dipole interaction and it is at the almost resonant condition with the frequency ω_{12} is close to the surface plasmon frequency, ω_{sp}, see Fig. 3.2.

For more than two mediums present in the system, we use the standard Laplace equation

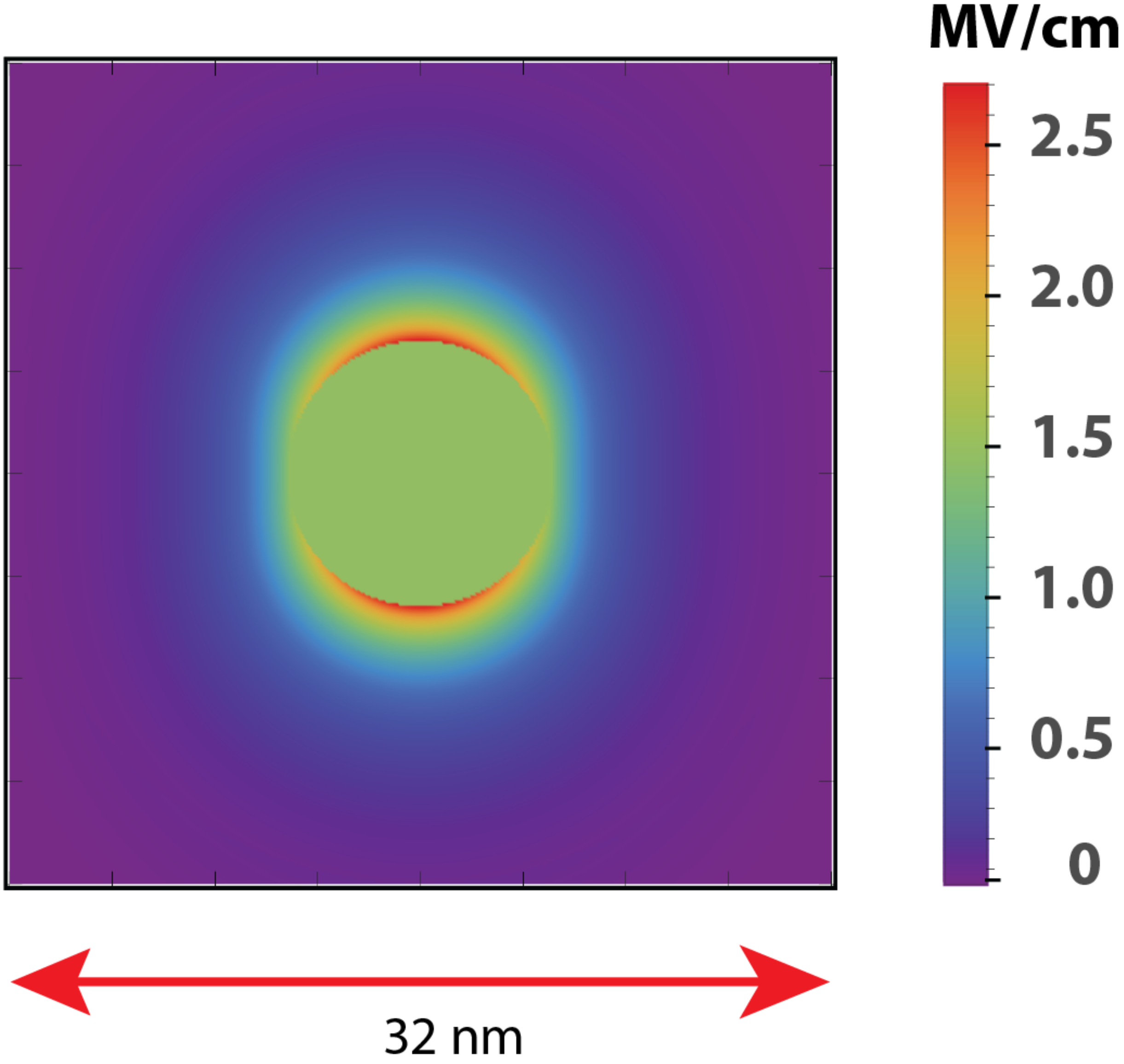

Figure 3.3 Electric field of the dipole mode of the spaser. The diameter of the spaser is 32 nm with a 10 nm diameter metal core inside it.

approach as adopted in a popular spaser research[5] to calculate the field of the Localized Surface Plasmons. In the spherical system, we consider the electric potential of the dipole mode to be of the form

$$\phi_i(\mathbf{r}) = \left(\frac{a_i}{r^2} + b_i r\right) Y_{10}(\mathbf{r}), \tag{3.1}$$

where i labels the medium ($i = 1, 2, 3$), a_i and b_i are coefficients corresponding to medium i, and $Y_{10}(\mathbf{r})$ is a spherical harmonics ($l = 1$ and $m = 0$). The Maxwell's continuity equations across the interfaces of the layers are given by the following expressions

$$\phi_i(\mathbf{r_i}) = \phi_{i+1}(\mathbf{r_i}), \tag{3.2}$$

$$\epsilon_i \frac{\partial}{\partial r}\phi_i(\mathbf{r_i}) = \epsilon_{i+1}\frac{\partial}{\partial r}\phi_{i+1}(\mathbf{r_i}), \tag{3.3}$$

where ϵ_i is the permittivity of medium i. For our system, which consists of 3 layers, silver sphere, dye, and water, we solve Eqs. (3.2) and (3.3) to obtain permittivity of silver (ϵ_s) as a function of permittivities of dye (ϵ_d) and water (ϵ_w), i.e.,

$$\epsilon_s \approx \epsilon_s(\epsilon_d, \epsilon_w). \tag{3.4}$$

The frequency of LSPs is then obtained by equating ϵ_s to the experimental value $\epsilon_{\mathrm{sil}}(\omega)$[104]

$$\epsilon_s = \mathrm{Re}[\epsilon_{\mathrm{sil}}(\omega_{\mathrm{sp}})] \tag{3.5}$$

The plasmon dipole mode creates a highly localized dipole-field as shown in the cross-section diagram in Fig. 3.3. The corresponding operator of electric field[3; 16] can be expressed in terms of creation and annihilation operators, $\hat{a}$ and $\hat{a}^*$, of SP,

$$\mathbf{E}(\mathbf{r}, t) = -A_{\mathrm{sp}}(\nabla\phi(\mathbf{r})\hat{a}e^{-i\omega t} + \nabla\phi^*(\mathbf{r})\hat{a}^* e^{i\omega t}), \tag{3.6}$$

where

$$A_{\rm sp} = \sqrt{\frac{4\pi\hbar}{s_1 \frac{\mathrm{d}\epsilon_{\rm sil}(\omega)}{\mathrm{d}\omega}}}\Bigg|_{\omega=\omega_{\rm sp}} \tag{3.7}$$

Here, the geometrical parameter s_1 is given by the following expression

$$s_1 = \frac{\displaystyle\int_{\mathcal{V}_{metal}} |\nabla\phi_i(\mathbf{r})|^2 d^3\mathbf{r}}{\displaystyle\int_{\text{All Space}} |\nabla\phi_i(\mathbf{r})|^2 d^3\mathbf{r}}. \tag{3.8}$$

The Hamiltonian of a spaser can be expressed in terms of individual Hamiltonians of surface plasmons and the gain medium, and the dipole type interaction Hamiltonian of the SP and the gain:

$$\hat{\mathcal{H}}_{total} = \hbar\omega_{\rm sp}\hat{a}^*\hat{a} + \hat{\mathcal{H}}_{gain} + \int_V \mathbf{E}(\mathbf{r},\mathbf{t})\hat{\mathbf{d}}\ d^{\mathbf{3}}\mathbf{r}. \tag{3.9}$$

Here V is the total volume of the gain medium and $\hat{\mathbf{d}}$ is the transition dipole moment operator of the gain medium.

In this article, we adopt a quasi-classical approach [16; 68] to study the properties of SPs, where the operators $\hat{a}$ and $\hat{a}^*$ are treated as classical variables represented in the form of a time dependent variable $\hat{a} = a_0 e^{-i\omega t}$ with a_0 being the slow varying amplitude. Then, the number of SPs in a given mode then can be written as $N_n = |a_0|^2$.

Below we assume that the corresponding dipole matrix elements are nonzero only between the levels $|0>$ and $|1>$ of the gain system, i.e., only the transitions between these levels can generate SPs. These interactions can be also characterized by the Rabi frequency[105], which is given by the following expression

$$\Omega_{10}(\mathbf{r},t) = \frac{\mathbf{E}(\mathbf{r},t)\mathbf{d_{01}}}{\hbar}, \tag{3.10}$$

where $\mathbf{d_{01}} =< 0|\hat{\mathbf{d}}|1 >$.

We describe the gain system within the density matrix approach with the corresponding equation of motion

$$i\hbar\dot{\hat{\rho}}(\mathbf{r},\mathbf{t}) = [\hat{\rho}(\mathbf{r},\mathbf{t}), \hat{\mathcal{H}}], \tag{3.11}$$

where $\hat{\rho}$ is the density matrix of three level gain system. Using Rotating Wave Approximation(RWA), we can express $\hat{\rho}(\mathbf{r},\mathbf{t})$ as slow-varying diagonal terms and fast varying non-diagonal terms with frequency $\omega \approx \omega_{\text{sp}}$.

$$\hat{\rho}(\mathbf{r}) = \begin{pmatrix} \rho_{22}(\mathbf{r},t) & 0 & 0 \\ 0 & \rho_{11}(\mathbf{r},t) & \rho_{10}(\mathbf{r},t)e^{i\omega t} \\ 0 & \rho_{01}(\mathbf{r},t)e^{-i\omega t} & \rho_{00}(\mathbf{r},t) \end{pmatrix}. \tag{3.12}$$

It is convenient to introduce the following notations: $n_0 = \rho_{00}$, $n_1 = \rho_{11}$ and $n_2 = \rho_{22}$. Then equations for the elements of the density matrix, which can be derived from Eq. (3.11), take the following form

$$\dot{\rho}_{10}(\mathbf{r}) = [-i(\omega-\omega_{10}) - \Gamma_{10}]\rho_{10}(\mathbf{r}) + \\ i n_{10}(\mathbf{r})\Omega^*_{10}(\mathbf{r})a^*_0, \tag{3.13}$$

$$\dot{n}_2 = g n_0 - \gamma_{21} n_2, \tag{3.14}$$

$$\dot{n}_1 = -\gamma_{10} n_1 + \gamma_{21} n_2 - 2\int_V d^{\mathbf{3}}\mathbf{r}\, \mathrm{Im}\left(\rho_{10}(\mathbf{r}) a_0 \Omega_{10}(\mathbf{r})\right), \tag{3.15}$$

$$\dot{n}_0 = -g n_0 + \gamma_{10} n_1 + 2\int_V d^{\mathbf{3}}\mathbf{r}\, \mathrm{Im}\left(\rho_{10}(\mathbf{r}) a_0 \Omega_{10}(\mathbf{r})\right), \tag{3.16}$$

where ω_{10} is the transition frequency between $|1>$ and $|0>$ levels of the gain medium and g is the rate of excitation from the $|0>$ level to the $|2>$ level by an external pulse. In the above equations, we also introduced the relaxation rates: polarization relaxation rate Γ_{10} and the spontaneous relaxation rates γ_{10} and γ_{21} between the corresponding states as indicated by the indices.

The equation of motion for SPs is obtained from Hamiltonian (3.9) and is given by the following expression

$$\dot{a} = -a_0\gamma_{\mathrm{sp}}(\omega) + i(\omega - \omega_{\mathrm{sp}})a_0 + \\ i\int_V d^{\mathbf{3}}\mathbf{r}\left(\rho^*_{10}(\mathbf{r})\Omega^*_{10}(\mathbf{r})\right), \tag{3.17}$$

where the plasmon relaxation rate $\gamma_{\mathrm{sp}}(\omega)$ is introduced, $\gamma_{\mathrm{sp}}(\omega) = \frac{\mathrm{Im}\{\epsilon_{\mathrm{sil}}(\omega)\}}{\frac{\mathrm{Re}\,\epsilon_{\mathrm{sil}}(\omega)}{\partial\omega}}$. Since the transitions between the levels $|0>$ and $|1>$ are due to coupling to the SPs, the corresponding relaxation rate, γ_{10}, can be expressed as

$$\gamma_{10} = |\Omega_{10}|^2 \frac{2(\gamma_{\text{sp}} + \Gamma_{10})}{(\omega_{\text{sp}} - \omega_{10})^2 + (\gamma_{\text{sp}} + \Gamma_{10})^2}. \tag{3.18}$$

Equations (3.13)-(3.17) determine the dynamics of three level spaser. First, we analyze the stationary solution of these equations, i.e., the continuous wave regime of a spaser. In this regime, the time derivatives in the left hand sides of Eqs. (3.13)-(3.17) are zero. It is convenient to introduce the population inversions through the following expressions

$$n_{10} = n_1 - n_0, \tag{3.19}$$

$$n_{21} = n_2 - n_1. \tag{3.20}$$

Then taking into account that $n_0 + n_1 + n_2 = 1$, we can express populations of different levels in terms of n_{10} as follows

$$n_0 = \frac{\gamma_{21} n_{10} - \gamma_{21}}{2\gamma_{21} + g}, \tag{3.21}$$

$$n_1 = -\frac{-\gamma_{21} - g n_{10} - \gamma_{21} n_{10}}{2\gamma_{21} + g}, \tag{3.22}$$

$$n_2 = -\frac{g n_{10} - g}{2\gamma_{21} + g}. \tag{3.23}$$

Substituting Eqs. (3.21)-(3.23) into the system of equations (3.13)-(3.17) we obtain the following solution of the stationary equations

$$\rho_{10}(\mathbf{r}) = -\frac{(a_0^* n_{10} \Omega_{10}^*(\mathbf{r}))}{i\Gamma_{10} - \omega_s + \omega_{10}}, \tag{3.24}$$

$$n_{10} = \frac{(\omega_s - \omega_{\mathrm{sp}})(\omega_{10} - \omega_s) + \gamma_{\mathrm{sp}}\Gamma_{10}}{V\rho\Omega_{10}^2}, \tag{3.25}$$

$$\begin{aligned} N_n = |a_0|^2 = & \frac{\Gamma_{10}^2 + (\omega_s - \omega_{10})^2}{2n_{10}\Gamma_{10}} \times \\ & \frac{\gamma_{21}\left(g - \gamma_{10} - n_{10}\left(\gamma_{10} + g\right)\right) - \gamma_{10} g n_{10}}{\left(2\gamma_{21} + g\right)\Omega_{10}^2}. \end{aligned} \tag{3.26}$$

In the above equations we assumed that the Rabi frequency is constant within the gain medium and the corresponding integrals in Eqs. (3.15) and (3.16) can be replaced by V. Here the spasing frequency ω_s is given by the following expression

$$\omega_s = \frac{\omega_{10}\gamma_{\mathrm{sp}} + \Gamma_{10}\omega_{\mathrm{sp}}}{\Gamma_{10} + \gamma_{\mathrm{sp}}}, \tag{3.27}$$

where $\omega_{\mathrm{sp}} < \omega_s < \omega_{10}$, and in the absence of detuning, i.e., if $\omega_{\mathrm{sp}} = \omega_{10}$, it is equal to ω_{sp}.

From the above expressions we can identify the effect of relaxation rate γ_{21} on the main spaser characteristics such as population inversion n_{10}, spasing frequency ω_s, threshold, and the number of generated plasmons N_n. From Eqs. (3.25), (3.27) one can see that both the population inversion and the spasing frequency do not depend on γ_{21}.

The spasing threshold g_{th} can be found from Eq. (3.26), where the threshold is determined from the condition $N_n = 0$,

$$g_{th} = \gamma_{10}\frac{1 + n_{10}}{1 - n_{10} - \frac{\gamma_{10}}{\gamma_{21}}n_{10}}. \tag{3.28}$$

Thus the spaser threshold depends on the relaxation rate, γ_{21}, but since $\gamma_{10} \ll \gamma_{21}$ this dependence is weak. Taking into account that $\gamma_{10}/\gamma_{21} \ll 1$, we can find the correction to the threshold $g_{th}^{(0)}$ determined by the two-level spaser model

$$g_{th} \approx g_{th}^{(0)} \left(1 + \frac{\gamma_{10}}{\gamma_{21}} \frac{n_{10}}{1 - n_{10}} \right), \tag{3.29}$$

where $g_{th}^{(0)} = \frac{1+n_{10}}{1-n_{10}} \gamma_{10}$.

Finite relaxation rate γ_{21} also affects the number of generated plasmons, see Eq. (3.26). When γ_{21} is large enough, i.e., $\gamma_{21} \gg g$, we can consider $\frac{1}{\gamma_{21}}$ as a small parameter and find expansion of Eq. (3.26) in the powers of $\frac{1}{\gamma_{21}}$ as follows

$$\begin{aligned} N_n = {} & \frac{\left(\Gamma_{10}^2 + (\omega_s - \omega_{10})^2\right)\left(g - \gamma_{10} - n_{10}\left(\gamma_{10} + g\right)\right)}{4 n_{10} \gamma_{10} \Gamma_{10} \Omega_{10}^2} - \\ & \frac{g\left(1 - n_{10}\right)\left(g - \gamma_{10}\right)\left({\Gamma_{10}}^2 + (\omega_s - \omega_{10})^2\right)}{8 n_{10} \gamma_{10}^2 \Gamma_{10} \Omega_{10}^2} \left(\frac{1}{\gamma_{21}}\right) - \\ & \frac{g^2\left(1 - n_{10}\right)\left(\Gamma_{10}^2 + (\omega_s - \omega_{10})^2\right)}{16 n_{10} \gamma_{10}^2 \Gamma_{10} \Omega_{10}^2} \left(\frac{1}{\gamma_{21}}\right)^2. \end{aligned} \tag{3.30}$$

The first term in this expansion is the result for the two-level spaser system[16], for which $\gamma_{21} \to \infty$. In this case, the number of generated SPs is proportional to the gain, g. The second and the third terms give the correction due to finite relaxation rate, γ_{21}. These terms introduce quadratic dependence on g.

3.3 Results and Discussions

3.3.1 System and Parameters

The spaser system is shown schematically in Fig. 3.1(a). A solid silver sphere of radius 5.15 nm is enclosed with a spherical dye layer making the total radius of the system 16 nm. The dielectric permittivity of the dye is $\epsilon_d = 2.2$, water is $\epsilon_w = 1.8$ and that of the metal $\epsilon_m(\omega)$ was obtained from the experimental data [104] of optical constants. The gain medium has an electronic band-gap of $\hbar\omega_{10} = 3.13$ eV. We have also used a small detuning ($\delta_2 = \hbar(\omega_{\text{sp}} - \omega_{10}) = 0.05$ eV) to highlight the robustness of the spaser under small frequency mismatch. The selection of these specific dimensions of the system ensures the matching of SPs frequency ω_{sp} to the transition frequency ω_{10}. Also, Additional parameters that is used are: $\hbar\Gamma_{10} = 0.01$ eV, $d_{10} = 1.5 \times 10^{-17}$ esu and the density of chromophores in a gain medium $\rho = 1.8 \times 10^{20}$ cm^{-3}.

3.3.2 Spasing in Continuous Wave (CW) Regime

In this subsection, we study the stationary solution, which is given by Eq. (3.26), as a function of the pumping rate, g: $N_n(g)$. The external optical pulse excites the gain system from the ground level, $|0>$, to the second excited level, $|2>$. If the relaxation from the level $|2>$ to first excited level $|1>$ is fast enough, then the spaser system is equivalent to the two-level system[16]. In this case, we observe the linear dependence of N_n on the gain rate g, see Fig. 3.4(a), where the fast relaxation rate, $\gamma_{21} \to \infty$, is shown by the blue line.

With decreasing the relaxation rate, γ_{21}, the first excited state, $|1>$, becomes less populated at a given value of the pump rate, g, which results in a smaller number of the generated SP. The corresponding dependencies, $N_n(g)$, are shown in Fig. 3.4(a) for γ_{21} in the range of 0.01 eV and 0.1 eV, i.e., for the relaxation time in the range of 6.5 fs and 65 fs. The data clearly show that N_n monotonically decreases with γ_{21}. For example, at $g = 25$ ps^{-1}, the number of plasmons decreases by almost a factor of 2 when the relaxation rate decrease from a large value to 0.01 eV. The dependence of N_n on g becomes also parabolic at finite values of γ_{21}.

To provide a more clear comparison of the two-level and the three-level spaser systems, we show in Fig. 3.4(b) the results for $\gamma_{21} = \infty$ (two-level system) and $\hbar\gamma_{21} = 0.03$ eV, i.e, the corresponding relaxation time is 22 fs, and interpolate them with parabolic dependence. While for the two-level system we have a clear linear dependence on g, the three-level system has an extra quadratic term. Interestingly, these calculations match the previous experimental findings [5; 102], where the N_n does not show a linear dependence on the pumping rate, but rather follows a parabolic dependence at a higher pumping rate g.

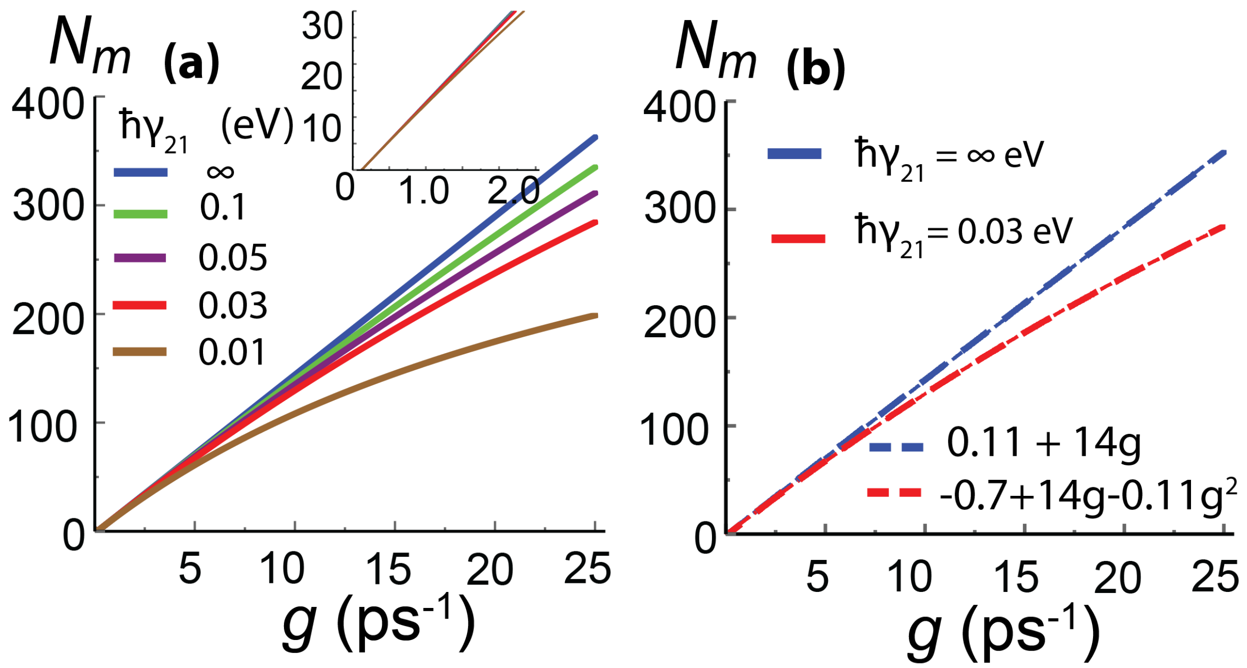

Figure 3.4 The number of generated SPs as a function of gain g in the stationary regime. (a) The number of SPs N_n is shown for different values of the relaxation rate γ_{21}, which characterizes the relaxation from the second excited states of the gain medium to the first excited state. For $\gamma_{21} = \infty$, our model is equivalent to the two-level spaser model. The cropped figure on the top right shows the presence of threshold visible at the lower values of pumping rate (b) The number of SPs as a function of g is shown for two values of γ_{21} with the corresponding parabolic fits. While for $\gamma_{21} = \infty$ the function $N_n(g)$ is a linear function, for $\hbar\gamma_{21} = 0.03$ eV, it is a parabolic function.

3.3.3 Spasing in a Dynamic Regime

The time dynamics of three-level spaser is shown in Fig. 3.5(a) for different values of γ_{21}. The initial number of SP, $N_n(t = 0)$, does not affect the final value of N_n. Thus, we arbitrarily set the initial value of N_n equals 100. The temporal profile of N_n is similar for different values

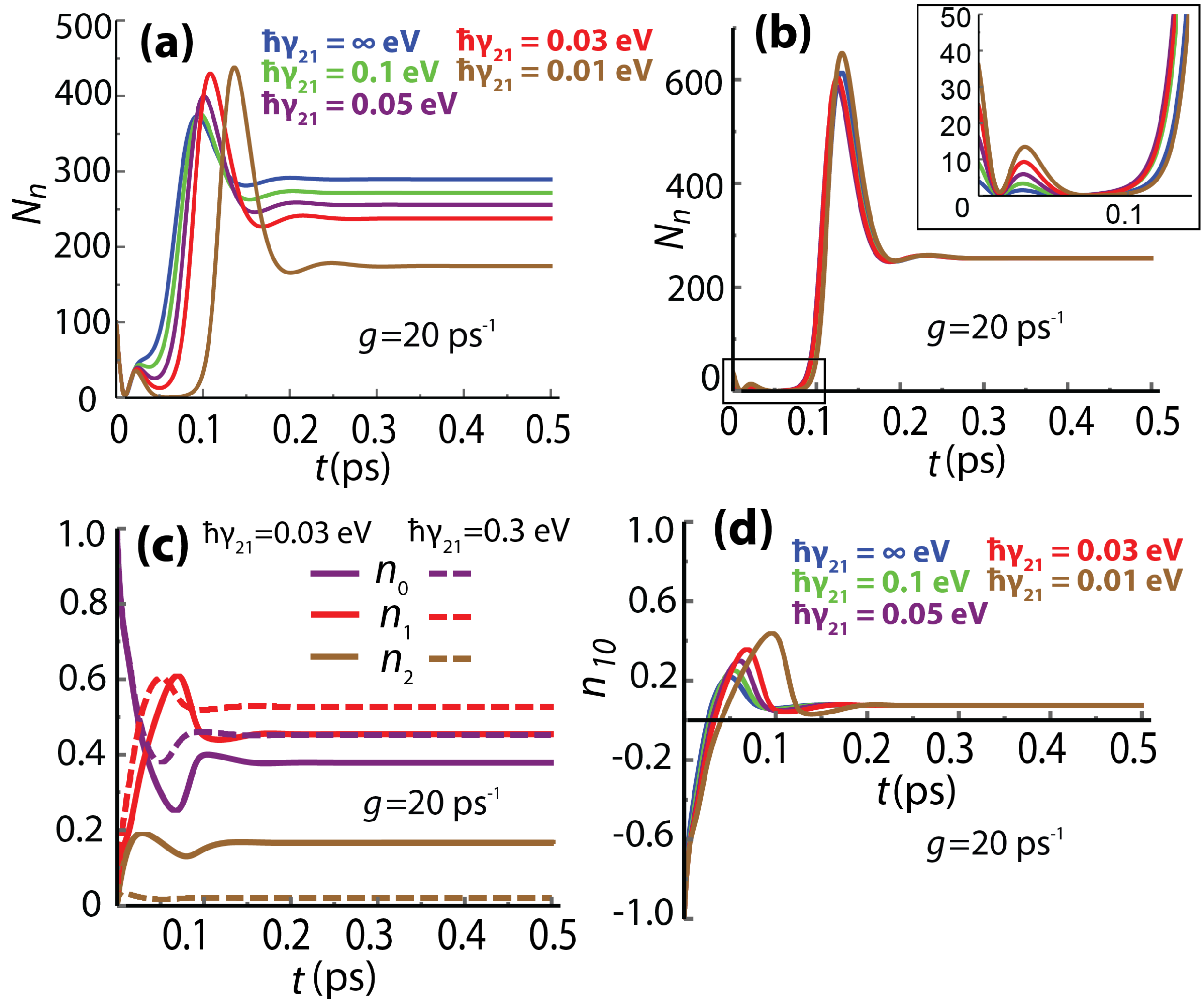

Figure 3.5 Illustration of the temporal dynamics of a spaser. (a) The number of generated SPs is shown as a function of time for different values of the relaxation rate γ_{21}. The gain is 20 ps^{-1}. The initial number of plasmons is 100, $N_n(t=0)=100$. (b) The number of generated SPs is shown as a function of time for different initial numbers of SPs. The gain is 20 ps^{-1} and $\hbar\gamma_{21}=0.05$ eV. (c) Populations n_2, n_1, n_0 of the corresponding levels of the gain medium, $|2>$, $|1>$, $|0>$, are shown as a function of time for two values of the γ_{21}. (d) The population inversion, $n_{10}=n_1-n_0$, is shown as a function of time. The values of γ_{21} are the same as in panel (a). The gain is 20 ps^{-1}.

of γ_{21} with one difference that with decreasing γ_{21} more pronounced oscillation at $t \approx 0.6$ ps are developed. The final stationary values of N_n follows the results shown in Fig. 3.4.

To illustrate that the stationary value of N_n does not depend on the initial condition, we show in Fig. 3.5(b) the profile $N_n(t)$ for different initial values. The relaxation rate is $\hbar\gamma_{21} = 0.05$ eV. The results show that the initial value of N_n only affects the amplitude of oscillations while the stationary solution is independent of $N_n(0)$.

Other characteristics of the spaser dynamics are populations of three levels of the gain medium, n_0, n_1, and n_2. They are shown in Fig. 3.5(c) for fast and slow relaxation rates, where the solid lines correspond to $\hbar\gamma_{21} = 0.03$ eV while the dashed lines correspond to $\hbar\gamma_{21} = 0.3$ eV. The data show that with a fast relaxation rate ($\hbar\gamma_{21} = 0.3$ eV) the population of the high energy level $|2>$ is almost zero, which corresponds to the limit of a two-level spaser system. Also, as expected, with increasing the relaxation rate, the populations of the ground and the first excited states, n_0 and n_1, increases while the population of the second excited state, n_2, decreases. The population inversion, which is the difference between populations n_1 and n_0, $n_{10} = n_1 - n_0$, is the same for both large and small relaxation rates. To illustrate this property we show in Fig. 3.5(d) the population inversion for different values of relaxation rate γ_{21}. The values of γ_{21} are the same as in Fig. 3.5(a). In all cases, the stationary population inversion does not depend on the relaxation rate, γ_{21}. This is consistent with expression (3.25), the right-hand side of which does not depend on γ_{21}.

3.4 Conclusion

Spaser is a unique system where the coupling of the plasmonic system and the gain medium results in the coherent generation of the localized plasmons at the nanoscale. The theories of spaser that are based on the two-level system of gain have their limitation in explaining the spasing behavior at the high pumping rates. In the present paper, we considered, within a semi-classical approach, a three-level gain system to identify the effects of relaxation between the non-spasing levels on the spaser dynamics. Our results show that the number of generated surface plasmons strongly depends on the relaxation rate γ_{21}. At large values of γ_{21}, i.e., fast relaxation, the three-level system converges to the regular two-level spaser system[16] with linear dependence of the number of generated plasmons on the pumping rate. However, at smaller values of γ_{21}, the dependence of the number of plasmons on the pumping rate becomes parabolic, which is more pronounced at large pump intensity. Such behavior is consistent with experimental results[5; 102]. Our spaser model can be beneficial in improving the efficacy of existing models and comparison with experimental results.

3.5 Acknowledgments

Major funding was provided by Grant No. DE-FG02-01ER15213 from the Chemical Sciences, Biosciences and Geosciences Division, Office of Basic Energy Sciences, Office of Science, US Department of Energy. Numerical simulations were performed using support by Grant No. DE-SC0007043 from the Materials Sciences and Engineering Division of the Office of the Basic Energy Sciences, Office of Science, US Department of Energy.

Appendices

A Supporting information for the Topological Nanospaser

A Stationary solution

For the large radius of TMDC nanopatch and for the gain rate larger than the critical value, in the stationary regime, two types of plasmons, co-rotating ($m = -1$) and counter-rotating ($m = 1$), are generated. Although the co-rotating mode is more strongly coupled to the K valley of TMDC then the counter-rotating one, the number of generated counter-rotating plasmons is larger then the number of co-rotating ones, $N_{-1} > N_1$. To understand this relation we consider the following approximation for the Rabi frequency dependence on the position within the TMDC nanopatch: (i) the $m = 1$ plasmon mode is coupled to the K valley of TMDC at $r < r_0 \approx 12$ nm and to the K' valley of TMDC at $r_1 > r > r_0$; (ii) the $m = -1$ plasmon mode is coupled to the K' valley of TMDC at $r < r_0$ and to the K valley of TMDC at $r_1 > r > r_0$. Here r_1 is the radius of TMDC nanopatch. Under this approximation, there two uncoupled systems: system "1": $m = 1$ plasmons, K valley of TMDC at $r < r_0$, and K' valley of TMDC at $r_1 > r > r_0$; system "2": $m = -1$ plasmons, K' valley of TMDC at $r < r_0$, and K valley of TMDC at $r_1 > r > r_0$.

Then the stationary equations for system "1" become (see Eqs. (2.13)-(2.15) of the main text)

$$\begin{aligned}
&\gamma_{\rm sp} a_1 = i\nu \int_{S_0} d^2\mathbf{r} \rho_K^*(\mathbf{r}) \tilde{\Omega}_{1,K}^*(\mathbf{r}) + i\nu \int_{S_1} d^2\mathbf{r} \rho_{K'}^*(\mathbf{r}) \tilde{\Omega}_{1,K'}^*(\mathbf{r}) \ , \\
&4{\rm Im}\left[\rho_K(\mathbf{r})\tilde{\Omega}_{1,K}(\mathbf{r}) a_1\right] = g_K\left[1 - n_K(\mathbf{r})\right] - \gamma_{2K}\left[1 + n_K(\mathbf{r})\right], \\
&\Gamma_{12}\rho_K(\mathbf{r}) = i n_K(\mathbf{r}) \tilde{\Omega}_{1,K}^* a_1^* \ , \\
&4{\rm Im}\left[\rho_{K'}(\mathbf{r})\tilde{\Omega}_{1,K'}(\mathbf{r}) a_1\right] = -\gamma_{2K}\left[1 + n_{K'}(\mathbf{r})\right], \\
&\Gamma_{12}\rho_{K'}(\mathbf{r}) = i n_{K'}(\mathbf{r}) \tilde{\Omega}_{1,K'}^* a_1^* \ .
\end{aligned}$$

Here S_0 and S_1 are defined by the conditions $r < r_0$ and $r_0 < r < r_1$, respectively. We also take into account that only the K valley is pumped by a circularly polarized light. Similar system of equations can be written for the system "2"

$$\begin{aligned}
&\gamma_{\rm sp} a_{-1} = i\nu \int_{S_1} d^2\mathbf{r} \rho_K^*(\mathbf{r}) \tilde{\Omega}_{-1,K}^*(\mathbf{r}) + i\nu \int_{S_0} d^2\mathbf{r} \rho_{K'}^*(\mathbf{r}) \tilde{\Omega}_{-1,K'}^*(\mathbf{r}) \ , \\
&4{\rm Im}\left[\rho_K(\mathbf{r})\tilde{\Omega}_{-1,K}(\mathbf{r}) a_{-1}\right] = g_K\left[1 - n_K(\mathbf{r})\right] - \gamma_{2K}\left[1 + n_K(\mathbf{r})\right], \\
&\Gamma_{12}\rho_K(\mathbf{r}) = i n_K(\mathbf{r}) \tilde{\Omega}_{-1,K}^* a_{-1}^* \ , \\
&4{\rm Im}\left[\rho_{K'}(\mathbf{r})\tilde{\Omega}_{-1,K'}(\mathbf{r}) a_{-1}\right] = -\gamma_{2K}\left[1 + n_{K'}(\mathbf{r})\right], \\
&\Gamma_{12}\rho_{K'}(\mathbf{r}) = i n_{K'}(\mathbf{r}) \tilde{\Omega}_{1,K'}^* a_{-1}^* \ .
\end{aligned}$$

From the above systems of equation, assuming that $|\Omega_{m,\boldsymbol{K}}|^2 a_m^2 \gg g_K \Gamma_{12}$, we obtain

$$N_1 = |a_1|^2 = \frac{\nu}{4\gamma_{\rm sp}}\left[g_K S_0 - \gamma_{2K}(S_0 + S_1)\right] \tag{31}$$

and

$$N_{-1} = |a_{-1}|^2 = \frac{\nu}{4\gamma_{\rm sp}}\left[g_K S_1 - \gamma_{2K}(S_0 + S_1)\right], \tag{32}$$

where S_0 and S_1 are the areas of the corresponding regions. Thus, above the threshold, the number of generated plasmons is proportional to $S_0 = \pi r_0^2$ for co-rotating plasmons and to $S_1 = \pi(r_1^2 - r_0^2)$ for counter-rotating plasmons. If $r_1 > \sqrt{2}r_0 \approx 16$ nm, i.e., $S_1 > S_0$, then the number of counter-rotating plasmons is larger than the number of co-rotating ones, $N_{-1} > N_1$.

B Far-field radiation

The total dipole moment of the spaser can be expressed in the following form

$$\mathbf{d_{total}} = \mathbf{d_{metal}} + \mathbf{d_{tmdc}}, \tag{33}$$

where $\mathbf{d_{metal}}$ is the dipole moment of the metal nanospheroid and $\mathbf{d_{tmdc}}$ is the dipole moment of the TMDC nanoflake.

B.1 Dipole moment of the metal nanospheroid

The electric field inside the metal, which is produced by generated plasmon modes, both $m = 1$ and $m = -1$, is uniform and is given by the following expression

$$\mathbf{E}_m(\mathbf{r}, t) = -A_{\mathrm{sp}}(\nabla\phi_m \hat{a}_m e^{-i\omega t} + \nabla\phi_m^* \hat{a}_m^* e^{i\omega t}), \tag{34}$$

where

$$A_{\mathrm{sp}} = \sqrt{\frac{4\pi\hbar s(\omega)}{\epsilon_d s'(\omega)}} \tag{35}$$

and

$$\mathrm{s}(\omega) = \frac{\epsilon_d}{\epsilon_d - \epsilon_{m(\omega)}}, \tag{36}$$

Then the dipole moment of the metal nanospheroid can be found from the following expression

$$\mathbf{d_{metal}} = \int_V \mu \mathbf{E_m}(\mathbf{r}, \mathbf{t})\, dv \tag{37}$$

where

$$\mu = \frac{\mathrm{Re}[\epsilon_{metal} - \epsilon_d]}{4\pi}. \tag{38}$$

Taking into account that the electric field inside the metal is a constant, $E_0 = |\nabla \phi_m|$, we derive the following expressions for the dipole moment of the metal nanospheroid

$$\mathbf{d_{metal,x}} = -\mu \mathrm{A_{sp}} \mathrm{E_0} \mathrm{V} \Big((\hat{a}_1 e^{-i\omega t} + \hat{a}_1^* e^{i\omega t}) + (\hat{a}_{-1} e^{-i\omega t} + \hat{a}_{-1}^* e^{i\omega t}) \Big) \tag{39}$$

$$\mathbf{d_{metal,y}} = -\mu \mathrm{A_{sp}} \mathrm{E_0} \mathrm{V} \Big(i(\hat{a}_1 e^{-i\omega t} - \hat{a}_1^* e^{i\omega t}) - i(\hat{a}_{-1} e^{-i\omega t} - \hat{a}_{-1}^* e^{i\omega t}) \Big) \tag{40}$$

B.2 Dipole moment of TMDC monolayer

The density matrix of TMDC nanoflake has the following structure

$$\hat{\rho}_{\boldsymbol{\mathcal{K}}}(\mathbf{r}, t) = \begin{pmatrix} \rho_{\boldsymbol{\mathcal{K}}}^{(\mathrm{c})}(\mathbf{r}, t) & \rho_{\boldsymbol{\mathcal{K}}}(\mathbf{r}, t) e^{i\omega t} \\ \rho_{\boldsymbol{\mathcal{K}}}^*(\mathbf{r}, t) e^{-i\omega t} & \rho_{\boldsymbol{\mathcal{K}}}^{(\mathrm{v})}(\mathbf{r}, t) \end{pmatrix}. \tag{41}$$

where $\boldsymbol{\mathcal{K}}$ is the valley index, K or K'. The off-diagonal elements, i.e., coherences, determine the dipole moment of TMDC system

$$\mathbf{d_{tmdc}} = \sum_{\mathrm{S}} \sum_{\boldsymbol{\mathcal{K}} = \mathbf{K}, \mathbf{K'}} (\rho_{\boldsymbol{\mathcal{K}}}(\mathbf{r}) \mathbf{d}_{\boldsymbol{\mathcal{K}}} e^{i\omega t} + \rho_{\boldsymbol{\mathcal{K}}}^*(\mathbf{r}) \mathbf{d}_{\boldsymbol{\mathcal{K}}}^* e^{-i\omega t}) + h.c., \tag{42}$$

where $\sum_{\mathrm{S}}$ is the sum (integral) over all points $\mathbf{r}$ of TMDC nanoflake.

The coherences satisfy the following stationary equation (see Eq. (2.13) of the main text)

$$[-i(\omega-\omega_{21})-\Gamma_{12}]\rho_{\boldsymbol{\mathcal{K}}}(\mathbf{r})+in_{\boldsymbol{\mathcal{K}}}(\mathbf{r})\sum_{m=1,-1}\tilde{\Omega}^{*}_{m,\boldsymbol{\mathcal{K}}}(\mathbf{r})a^{*}_{m}=0, \tag{43}$$

where Γ_{12} is the polarization relaxation rate, $n_{\boldsymbol{\mathcal{K}}}$ is the population inversion defined as

$$n_{\boldsymbol{\mathcal{K}}}\equiv\rho^{(\mathrm{c})}_{\boldsymbol{\mathcal{K}}}-\rho^{(\mathrm{v})}_{\boldsymbol{\mathcal{K}}}\ , \tag{44}$$

and

$$\tilde{\Omega}_{m,\boldsymbol{\mathcal{K}}}(\mathbf{r})=-\frac{1}{\hbar}A_{\mathrm{sp}}\nabla\phi_{m}(\mathbf{r})\mathbf{d}_{\boldsymbol{\mathcal{K}}}\ . \tag{45}$$

From Eq. (43) we can find the stationary coherences of TMDC monolayer

$$\rho_{\boldsymbol{\mathcal{K}}}(\mathbf{r})=-\frac{in_{\boldsymbol{\mathcal{K}}}(\mathbf{r})\sum_{m=1,-1}\tilde{\Omega}^{*}_{m,\boldsymbol{\mathcal{K}}}(\mathbf{r})a^{*}_{m}}{-(\omega-\omega_{21})+i\Gamma_{12}}. \tag{46}$$

We substitute Eq. (46) into Eq. (42) and obtain the following expression for the dipole moment of TMDC

$$\mathbf{d_{tmdc}}=\mathrm{f}_{\mathbf{K}}\mathbf{d}_{\mathbf{K}}e^{i\omega t}+\mathrm{f}_{\mathbf{K}'}\mathbf{d}_{\mathbf{K}'}e^{i\omega t}+h.c., \tag{47}$$

where the following notations were introduced

$$\mathrm{f}_{\mathbf{K}}=-\nu\sum_{\mathrm{S}}\frac{in_{\mathbf{K}}(\mathbf{r})\sum_{m=1,-1}\tilde{\Omega}^{*}_{m,\mathbf{K}}a^{*}_{m}}{-(\omega-\Delta_{\mathrm{g}})+i\Gamma_{12}} \tag{48}$$

$$\mathrm{f}_{\mathbf{K}'}=-\nu\sum_{\mathrm{S}}\frac{in_{\mathbf{K}'}(\mathbf{r})\sum_{m=1,-1}\tilde{\Omega}^{*}_{m,\mathbf{K}'}a^{*}_{m}}{-(\omega-\Delta_{\mathrm{g}})+i\Gamma_{12}}. \tag{49}$$

Taking into account that $\mathbf{d_K} = \mathrm{d}_0(1, i)$ and $\mathbf{d_{K'}} = \mathrm{d}_0(1, -i)$ we obtain the x and y components of the dipole moment

$$\mathbf{d_{tmdc,x}} = \mathrm{f}_{\mathbf{K}}\mathrm{d}_0 e^{i\omega t} + \mathrm{f}_{\mathbf{K'}}\mathrm{d}_0 e^{i\omega t} + h.c. \tag{50}$$

$$\mathbf{d_{tmdc,y}} = i\mathrm{f}_{\mathbf{K}}\mathrm{d}_0 e^{i\omega t} - i\mathrm{f}_{\mathbf{K'}}\mathrm{d}_0 e^{i\omega t} + h.c. \tag{51}$$

B.3 Far field dipole radiation

The total dipole moment of the spaser system is the sum of the dipole moment of the metal nanospheroid and TMDC nanoflake. Its x and y components can be expressed as

$$\begin{aligned}\mathbf{d_{total,x}} = &-\mu \mathrm{A_{sp}} \mathrm{E}_0 \mathrm{V} \left(\hat{a}_1 e^{-i\omega t} + \hat{a}_{-1} e^{-i\omega t} + h.c.\right) \\ &+ \left(\mathrm{f}_{\mathbf{K}}\mathrm{d}_0 e^{i\omega t} + \mathrm{f}_{\mathbf{K'}}\mathrm{d}_0 e^{i\omega t} + h.c.\right) \end{aligned} \tag{52}$$

$$\begin{aligned}\mathbf{d_{total,y}} = &-\mu \mathrm{A_{sp}} \mathrm{E}_0 \mathrm{V} \left((i\hat{a}_1 e^{-i\omega t} - i\hat{a}_{-1} e^{-i\omega t} + h.c.\right) \\ &+ \left(i\mathrm{f}_{\mathbf{K}}\mathrm{d}_0 e^{i\omega t} - i\mathrm{f}_{\mathbf{K'}}\mathrm{d}_0 e^{i\omega t} + h.c.\right) \end{aligned} \tag{53}$$

These expressions have the following structure

$$\mathbf{d_{total,x}} = 2\mathrm{Re}\left[B_x e^{i\omega t}\right], \tag{54}$$

$$\mathbf{d_{total,y}} = 2\mathrm{Re}\left[B_y e^{i\omega t}\right], \tag{55}$$

where,

$$B_x = -\mu \mathrm{A}_{\mathrm{sp}} \mathrm{E}_0 \mathrm{V}(\hat{a}_1^* + \hat{a}_{-1}^*) + \mathrm{f}_{\mathbf{K}} \mathrm{d}_0 + \mathrm{f}_{\mathbf{K}'} \mathrm{d}_0, \tag{56}$$

$$B_y = i\mu \mathrm{A}_{\mathrm{sp}} \mathrm{E}_0 \mathrm{V}(\hat{a}_1^* - \hat{a}_{-1}^*) + i\mathrm{f}_{\mathbf{K}} \mathrm{d}_0 - i\mathrm{f}_{\mathbf{K}'} \mathrm{d}_0. \tag{57}$$

The total dipole moment of the system determines the far-field radiation of the spaser. The polarization of radiation is characterized by the x and y components of the far electric field, which are proportional to the corresponding components of the dipole moment, i.e., $\mathbf{d}_{\mathbf{total},\mathbf{x}}$ and $\mathbf{d}_{\mathbf{total},\mathbf{y}}$, while the total radiation power is given by the following expression

$$\begin{aligned} I &= \frac{4}{3}\left(\frac{\omega}{c_0}\right)^3 \frac{(\epsilon_{\mathrm{d}})^{1/2}}{\hbar} \langle |\mathbf{d}_{\mathbf{total}}|^2 \rangle \\ &= \frac{8}{3}\left(\frac{\omega}{c_0}\right)^3 \frac{(\epsilon_{\mathrm{d}})^{1/2}}{\hbar} (|B_x|^2 + |B_y|^2) \end{aligned} \tag{58}$$

where $\langle \ldots \rangle$ means the time average.

REFERENCES

[1] A. L. Schawlow, C. H. Townes, Infrared and optical masers, Phys. Rev. 112 (1958) 1940.

[2] T. H. Maiman, et al., Stimulated optical radiation in ruby (1960).

[3] D. J. Bergman, M. I. Stockman, Surface plasmon amplification by stimulated emission of radiation: Quantum generation of coherent surface plasmons in nanosystems, Phys. Rev. Lett. 90 (2003) 027402–1–4.

[4] J. Reed, Light-matter interactions of plasmonic nanostructures (2013).

[5] E. I. Galanzha, R. Weingold, D. A. Nedosekin, M. Sarimollaoglu, J. Nolan, W. Harrington, A. S. Kuchyanov, R. G. Parkhomenko, F. Watanabe, Z. Nima, A. S. Biris, A. I. Plekhanov, M. I. Stockman, V. P. Zharov, Spaser as a biological probe, Nat. Commun. 8 (2017) 15528–1–7.

[6] G. Barbillon, T. Noblet, B. Busson, A. Tadjeddine, C. Humbert, Localised detection of thiophenol with gold nanotriangles highly structured as honeycombs by nonlinear sum frequency generation spectroscopy, Journal of materials science 53 (6) (2018) 4554–4562.

[7] M. Dolci, J.-F. Bryche, C. Leuvrey, S. Zafeiratos, S. Gree, S. Begin-Colin, G. Barbillon, B. P. Pichon, Robust clicked assembly based on iron oxide nanoparticles for a new type of spr biosensor, Journal of Materials Chemistry C 6 (34) (2018) 9102–9110.

[8] Y. He, S. Su, T. Xu, Y. Zhong, J. A. Zapien, J. Li, C. Fan, S.-T. Lee, Silicon nanowires-based highly-efficient sers-active platform for ultrasensitive dna detection, Nano Today 6 (2) (2011) 122–130.

[9] G. Barbillon, Fabrication and sers performances of metal/si and metal/zno nanosensors: A review, Coatings 9 (2) (2019) 86.

[10] M. Li, U. Guler, Y. Li, A. Rea, E. K. Tanyi, Y. Kim, M. A. Noginov, Y. Song, A. Boltasseva, V. M. Shalaev, et al., Plasmonic biomimetic nanocomposite with spontaneous subwavelength structuring as broadband absorbers, ACS Energy Letters 3 (7) (2018) 1578–1583.

[11] C. Haffner, W. Heni, Y. Fedoryshyn, J. Niegemann, A. Melikyan, D. L. Elder, B. Baeuerle, Y. Salamin, A. Josten, U. Koch, et al., All-plasmonic mach–zehnder modulator enabling optical high-speed communication at the microscale, Nature Photonics 9 (8) (2015) 525–528.

[12] Y. Salamin, P. Ma, B. Baeuerle, A. Emboras, Y. Fedoryshyn, W. Heni, B. Cheng, A. Josten, J. Leuthold, 100 ghz plasmonic photodetector, ACS photonics 5 (8) (2018) 3291–3297.

[13] I. Vangelidis, A. Theodosi, M. J. Beliatis, K. K. Gandhi, A. Laskarakis, P. Patsalas, S. Logothetidis, S. R. P. Silva, E. Lidorikis, Plasmonic organic photovoltaics: unraveling plasmonic enhancement for realistic cell geometries, Acs Photonics 5 (4) (2018) 1440–1452.

[14] M. Willatzen, L. C. L. Y. Voon, Oblate spheroidal coordinates, in: Separable Boundary-Value Problems in Physics, Wiley-VCH, Weinheim, Germany, 2011, pp. 155–164.

[15] M. I. Stockman, S. V. Faleev, D. J. Bergman, Localization versus delocalization of surface plasmons in nanosystems: Can one state have both characteristics?, Phys. Rev. Lett. 87 (2001) 167401–1–4.

[16] M. I. Stockman, The spaser as a nanoscale quantum generator and ultrafast amplifier, Journal of Optics 12 (2010) 024004–1–13.

[17] P. B. Johnson, R. W. Christy, Optical constants of noble metals, Phys. Rev. B 6 (1972) 4370–4379.

[18] G. B. Liu, W. Y. Shan, Y. G. Yao, W. Yao, D. Xiao, Three-band tight-binding model for monolayers of group-VIB transition metal dichalcogenides, Phys. Rev. B 88 (2013) 085433–1–10.

[19] M. V. Berry, Quantal phase factors accompanying adiabatic changes, Proc. Royal Soc. London Ser. A 392 (1984) 45–57.

[20] D. Xiao, M. C. Chang, Q. Niu, Berry phase effects on electronic properties, Reviews of Modern Physics 82 (3) (2010) 1959–2007. `doi:10.1103/RevModPhys.82.1959`. URL `<GotoISI>://WOS:000279557500001`

[21] K. Li, X. Li, M. I. Stockman, D. J. Bergman, Surface plasmon amplification by stimulated emission in nanolenses, Phys. Rev. B 71 (2005) 115409–1–4.

[22] D. Y. Fedyanin, Toward an electrically pumped spaser, Opt. Lett. 37 (2012) 404–406.

[23] D. G. Baranov, A. P. Vinogradov, A. A. Lisyansky, Y. M. Strelniker, D. J. Bergman, Magneto-optical spaser, Opt. Lett. 38 (2013) 2002–2004.

[24] N. I. Zheludev, S. L. Prosvirnin, N. Papasimakis, V. A. Fedotov, Lasing spaser, Nat. Phot. 2 (2008) 351–354.

[25] M. A. Noginov, G. Zhu, A. M. Belgrave, R. Bakker, V. M. Shalaev, E. E. Narimanov, S. Stout, E. Herz, T. Suteewong, U. Wiesner, Demonstration of a spaser-based nanolaser, Nature 460 (2009) 1110–1112.

[26] R. F. Oulton, V. J. Sorger, T. Zentgraf, R.-M. Ma, C. Gladden, L. Dai, G. Bartal,

X. Zhang, Plasmon lasers at deep subwavelength scale, Nature 461 (2009) 629–632.

[27] R.-M. Ma, R. F. Oulton, V. J. Sorger, G. Bartal, X. Zhang, Room-temperature sub-diffraction-limited plasmon laser by total internal reflection, Nat. Mater. 10 (2010) 110–113.

[28] R. A. Flynn, C. S. Kim, I. Vurgaftman, M. Kim, J. R. Meyer, A. J. Mäkinen, K. Bussmann, L. Cheng, F. S. Choa, J. P. Long, A room-temperature semiconductor spaser operating near 1.5 micron, Opt. Express 19 (2011) 8954–8961.

[29] M. J. H. Marell, B. Smalbrugge, E. J. Geluk, P. J. van Veldhoven, B. Barcones, B. Koopmans, R. Nötzel, M. K. Smit, M. T. Hill, Plasmonic distributed feedback lasers at telecommunications wavelengths, Opt. Express 19 (2011) 15109–15118.

[30] F. v. Beijnum, P. J. v. Veldhoven, E. J. Geluk, M. J. A. d. Dood, G. W. t. Hooft, M. P. v. Exter, Surface plasmon lasing observed in metal hole arrays, Phys. Rev. Lett. 110 (2013) 206802–1–5.

[31] Y.-J. Lu, C.-Y. Wang, J. Kim, H.-Y. Chen, M.-Y. Lu, Y.-C. Chen, W.-H. Chang, L.-J. Chen, M. I. Stockman, C.-K. Shih, S. Gwo, All-color plasmonic nanolasers with ultralow thresholds: Autotuning mechanism for single-mode lasing, Nano Lett. 14 (2014) 4381–4388.

[32] Q. Zhang, G. Li, X. Liu, F. Qian, Y. Li, T. C. Sum, C. M. Lieber, Q. Xiong, A room temperature low-threshold ultraviolet plasmonic nanolaser, Nat. Commun. 5 (2014) 4953–1–9.

[33] B. T. Chou, Y. H. Chou, Y. M. Wu, Y. C. Chung, W. J. Hsueh, S. W. Lin, T. C. Lu, T. R. Lin, S. D. Lin, Single-crystalline aluminum film for ultraviolet plasmonic nanolasers, Sci. Rep. 6 (2016) 19887–1–9.

[34] C.-J. Lee, H. Yeh, F. Cheng, P.-H. Su, T.-H. Her, Y.-C. Chen, C.-Y. Wang, S. Gwo, S. R. Bank, C.-K. Shih, W.-H. Chang, Low-threshold plasmonic lasers on a single-crystalline epitaxial silver platform at telecom wavelength, ACS Photonics 4 (2017) 1431–1439.

[35] S. Sun, C. Zhang, K. Wang, S. Wang, S. Xiao, Q. Song, Lead halide perovskite nanoribbon based uniform nanolaser array on plasmonic grating, ACS Photonics 4 (2017) 649–656.

[36] R. Ma, X. Yin, R. F. Oulton, V. J. Sorger, X. Zhang, Multiplexed and electrically modulated plasmon laser circuit, Nano Lett. (2012) doi: 10.1021/nl302809a.

[37] R.-M. Ma, S. Ota, Y. Li, S. Yang, X. Zhang, Explosives detection in a lasing plasmon nanocavity, Nature Nanotechnology 9 (2014) 600–604.

[38] S. Wang, B. Li, X. Y. Wang, H. Z. Chen, Y. L. Wang, X. W. Zhang, L. Dai, R. M. Ma, High-yield plasmonic nanolasers with superior stability for sensing in aqueous solution, ACS Photonics 4 (2017) 1355–1360.

[39] Z. Wu, J. Chen, Y. Mi, X. Sui, S. Zhang, W. Du, R. Wang, J. Shi, X. Wu, X. Qiu, Z. Qin, Q. Zhang, X. Liu, All-inorganic cspbbr$_3$ nanowire based plasmonic lasers, Advanced Optical Materials (2018) 1800674–1–8.

[40] Y.-J. Lu, J. Kim, H.-Y. Chen, C. Wu, N. Dabidian, C. E. Sanders, C.-Y. Wang, M.-Y. Lu, B.-H. Li, X. Qiu, W.-H. Chang, L.-J. Chen, G. Shvets, C.-K. Shih, S. Gwo, Plasmonic nanolaser using epitaxially grown silver film, Science 337 (2012) 450–453.

[41] C.-J. Lee, H. Yeh, F. Cheng, P.-H. Su, T.-H. Her, Y.-C. Chen, C.-Y. Wang, S. Gwo, S. R. Bank, C.-K. Shih, W.-H. Chang, Low-threshold plasmonic lasers on a single-crystalline epitaxial silver platform at telecom wavelength, ACS Photonics 4 (2017)

1431–1439.

[42] S. Gwo, C.-K. Shih, Semiconductor plasmonic nanolasers: Current status and perspectives, Rep. Prog. Phys. 79 (2016) 086501.

[43] C.-Z. Ning, Semiconductor nanolasers and the size-energy-efficiency challenge: A review, Advanced Photonics 1 (2019) 014002–1–10.

[44] S. J. P. Kress, J. Cui, P. Rohner, D. K. Kim, F. V. Antolinez, K.-A. Zaininger, S. V. Jayanti, P. Richner, K. M. McPeak, D. Poulikakos, D. J. Norris, A customizable class of colloidal-quantum-dot spasers and plasmonic amplifiers, Science Advances 3 (2017) e1700688–1–7.

[45] E. Plum, V. A. Fedotov, P. Kuo, D. P. Tsai, N. I. Zheludev, Towards the lasing spaser: Controlling metamaterial optical response with semiconductor quantum dots, Opt. Express 17 (2009) 8548–8551.

[46] Y.-W. Huang, W. T. Chen, P. C. Wu, V. A. Fedotov, N. I. Zheludev, D. P. Tsai, Toroidal lasing spaser, Sci. Rep. 3 (2013) 1237–1–4.

[47] W. Zhou, M. Dridi, J. Y. Suh, C. H. Kim, D. T. Co, M. R. Wasielewski, G. C. Schatz, T. W. Odom, Lasing action in strongly coupled plasmonic nanocavity arrays, Nature Nano 8 (2013) 506–511.

[48] J.-S. Wu, V. Apalkov, M. I. Stockman, Topological spaser, arXiv: 1909.11113 [cond-mat.mes-hall] (2019).

[49] X. Y. Wang, Y. L. Wang, S. Wang, B. Li, X. W. Zhang, L. Dai, R. M. Ma, Lasing enhanced surface plasmon resonance sensing, Nanophotonics 6 (2017) 472–478.

[50] M. Stockman, Spasers to speed up cmos processors (2018).

[51] D. Xiao, M.-C. Chang, Q. Niu, Berry phase effects on electronic properties, Reviews

of Modern Physics 82 (2010) 1959–2007.

[52] Y. M. You, X. X. Zhang, T. C. Berkelbach, M. S. Hybertsen, D. R. Reichman, T. F. Heinz, Observation of biexcitons in monolayer wse2, Nat. Phys. 11 (2015) 477–U138.

[53] K. S. Novoselov, A. Mishchenko, A. Carvalho, A. H. C. Neto, 2d materials and van der Waals heterostructures, Science 353 (2016) 461–1–11.

[54] D. N. Basov, M. M. Fogler, F. J. G. de Abajo, Polaritons in van der Waals materials, Science 354 (2016) 195–1–8.

[55] O. Salehzadeh, M. Djavid, N. H. Tran, I. Shih, Z. Mi, Optically pumped two-dimensional mos2 lasers operating at room-temperature, Nano letters 15 (8) (2015) 5302–5306.

[56] Y. Ye, Z. J. Wong, X. Lu, X. Ni, H. Zhu, X. Chen, Y. Wang, X. Zhang, Monolayer excitonic laser, Nat. Phot. 9 (2015) 733.

[57] S. Wu, S. Buckley, J. R. Schaibley, L. Feng, J. Yan, D. G. Mandrus, F. Hatami, W. Yao, J. Vučković, A. Majumdar, X. Xu, Monolayer semiconductor nanocavity lasers with ultralow thresholds, Nature 520 (2015) 69–72.

[58] T. Cao, G. Wang, W. Han, H. Ye, C. Zhu, J. Shi, Q. Niu, P. Tan, E. Wang, B. Liu, J. Feng, Valley-selective circular dichroism of monolayer molybdenum disulphide, Nat. Commun. 3 (2012) 887–1–5.

[59] Z. Ye, D. Sun, T. F. Heinz, Optical manipulation of valley pseudospin, Nat. Phys. 13 (2016) 26–30.

[60] S. Wu, S. Buckley, J. R. Schaibley, L. Feng, J. Yan, D. G. Mandrus, F. Hatami, W. Yao, J. Vuckovic, A. Majumdar, Ultra-low threshold monolayer semiconductor nanocavity lasers, arXiv preprint arXiv:1502.01973 (2015).

[61] F. Bloch, A. Siegert, Magnetic resonance for nonrotating fields, Phys. Rev. 57 (1940) 522–527. `doi:10.1103/PhysRev.57.522`.
URL `https://link.aps.org/doi/10.1103/PhysRev.57.522`

[62] G. S. Agarwal, Rotating-wave approximation and spontaneous emission, Phys. Rev. A 4 (1971) 1778–1781. `doi:10.1103/PhysRevA.4.1778`.
URL `https://link.aps.org/doi/10.1103/PhysRevA.4.1778`

[63] M. I. Stockman, Nanoplasmonics: Past, present, and glimpse into future, Opt. Express 19 (2011) 22029–22106.

[64] L. D. Landau, E. M. Lifshitz, The Classical Theory of Fields, Pergamon Press, Oxford, New York, 1975.

[65] R. Ghimire, J.-S. Wu, V. Apalkov, M. I. J. N. Stockman, Topological nanospaser 1 (ahead-of-print) (2020).

[66] X. Fan, S.-H. J. N. m. Yun, The potential of optofluidic biolasers 11 (2) (2014) 141–147.

[67] M. I. Stockman, Nanoplasmonics: The physics behind the applications, Phys. Today 64 (2) (2011) 39–44.

[68] M. I. Stockman, Nanoplasmonics: past, present, and glimpse into future, Optics express 19 (22) (2011) 22029–22106.

[69] B. Dong, Y. Ma, Z. Ren, C. Lee, Recent progress in nanoplasmonics-based integrated optical micro/nano-systems, Journal of Physics D: Applied Physics 53 (21) (2020) 213001. `doi:10.1088/1361-6463/ab77db`.
URL `http://dx.doi.org/10.1088/1361-6463/ab77db`

[70] S. Kawata, Y. Inouye, P. Verma, Plasmonics for near-field nano-imaging and superlensing, Nature Photonics 3 (7) (2009) 388–394. `doi:10.1038/nphoton.2009.111`.

URL `https://doi.org/10.1038/nphoton.2009.111`

[71] N. Kholmicheva, L. R. Romero, J. Cassidy, M. Zamkov, Prospects and applications of plasmon-exciton interactions in the near-field regime, Nanophotonics 8 (4) (2018) 613–628.

[72] J. N. Anker, W. P. Hall, O. Lyandres, N. C. Shah, J. Zhao, R. P. Van Duyne, Biosensing with plasmonic nanosensors, Nanoscience and Technology: A Collection of Reviews from Nature Journals (2010) 308–319.

[73] H. Kim, J. U. Lee, S. Kim, S. Song, S. J. Sim, A nanoplasmonic biosensor for ultrasensitive detection of alzheimer's disease biomarker using a chaotropic agent, ACS sensors 4 (3) (2019) 595–602.

[74] D. Zhang, Q. Zhang, Y. Lu, Y. Yao, S. Li, Q. Liu, Nanoplasmonic biosensor using localized surface plasmon resonance spectroscopy for biochemical detection, Springer, 2017.

[75] Y. Liu, J. Guo, J. Jiang, W. Chen, L. Zhao, W. Chen, R. Liang, J. Xu, Simple Preparations for Plasmon-Enhanced Photodetectors, IntechOpen, 2019.

[76] L. Tang, S. E. Kocabas, S. Latif, A. K. Okyay, D.-S. Ly-Gagnon, K. C. Saraswat, D. A. Miller, Nanometre-scale germanium photodetector enhanced by a near-infrared dipole antenna, Nature Photonics 2 (4) (2008) 226–229.

[77] M. I. Stockman, Brief history of spaser from conception to the future, Advanced Photonics 2 (5) (2020) 054002.

[78] S. I. Azzam, A. V. Kildishev, R.-M. Ma, C.-Z. Ning, R. Oulton, V. M. Shalaev, M. I. Stockman, J.-L. Xu, X. Zhang, Ten years of spasers and plasmonic nanolasers, Nature 9 (1) (2020) 1–21.

[79] M. Premaratne, M. I. Stockman, Theory and technology of spasers, Advances in Optics and Photonics 9 (1) (2017) 79–128. `doi:10.1364/AOP.9.000079`.
URL `http://aop.osa.org/abstract.cfm?URI=aop-9-1-79https://www.osapublishing.org/aop/abstract.cfm?uri=aop-9-1-79`

[80] J. Aizpurua, H. A. Atwater, J. J. Baumberg, S. I. Bozhevolnyi, M. L. Brongersma, J. A. Dionne, H. Giessen, N. Halas, Y. Kivshar, M. F. Kling, F. Krausz, S. Maier, S. V. Makarov, M. Mikkelsen, M. Moskovits, P. Norlander, T. Odom, A. Polman, C. W. Qiu, M. Segev, V. M. Shalaev, P. Törmä, D. P. Tsai, E. Verhagen, A. Zayats, X. Zhang, N. I. Zheludev, Mark stockman: Evangelist for plasmonics, ACS Photonics 8 (3) (2021) 683–698. `doi:10.1021/acsphotonics.1c00299`.
URL `https://doi.org/10.1021/acsphotonics.1c00299`

[81] A. Boltasseva, V. M. Shalaev, N. I. Zheludev, Mark stockman, the knight of plasmonics, Nature Photonics 15 (5) (2021) 321–322. `doi:10.1038/s41566-021-00799-7`.
URL `https://doi.org/10.1038/s41566-021-00799-7`

[82] M. Khajavikhan, A. Simic, M. Katz, J. Lee, B. Slutsky, A. Mizrahi, V. Lomakin, Y. J. N. Fainman, Thresholdless nanoscale coaxial lasers 482 (7384) (2012) 204–207.

[83] C.-Z. J. A. P. Ning, Semiconductor nanolasers and the size-energy-efficiency challenge: a review 1 (1) (2019) 014002.

[84] J. Shane, Q. Gu, F. Vallini, B. Wingad, J. S. Smalley, N. C. Frateschi, Y. Fainman, Thermal considerations in electrically-pumped metallo-dielectric nanolasers, in: Physics and Simulation of Optoelectronic Devices XXII, Vol. 8980, International Society for Optics and Photonics, p. 898027.

[85] K. Shen, C. Ku, C. Hsieh, H. Kuo, Y. Cheng, D. P. J. A. M. Tsai, Deep-ultraviolet

hyperbolic metacavity laser 30 (21) (2018) 1706918.

[86] K. Ding, C.-Z. J. L. S. Ning, Applications, Metallic subwavelength-cavity semiconductor nanolasers 1 (7) (2012) e20–e20.

[87] K. Ding, J. Diaz, D. Bimberg, C.-Z. J. L. Ning, P. Reviews, Modulation bandwidth and energy efficiency of metallic cavity semiconductor nanolasers with inclusion of noise effects 9 (5) (2015) 488–497.

[88] V. Dolores-Calzadilla, B. Romeira, F. Pagliano, S. Birindelli, A. Higuera-Rodriguez, P. Van Veldhoven, M. Smit, A. Fiore, D. J. N. c. Heiss, Waveguide-coupled nanopillar metal-cavity light-emitting diodes on silicon 8 (1) (2017) 1–8.

[89] P.-J. Cheng, Z.T. Huang, J.-H. Li, B.-T. Chou, Y.-H. Chou, W.-C. Lo, K.-P. Chen, T.-C. Lu, T.-R. J. A. P. Lin, High-performance plasmonic nanolasers with a nanotrench defect cavity for sensing applications 5 (7) (2018) 2638–2644.

[90] S. Wang, B. Li, X.-Y. Wang, H.-Z. Chen, Y.-L. Wang, X.-W. Zhang, L. Dai, R.-M. J. A. P. Ma, High-yield plasmonic nanolasers with superior stability for sensing in aqueous solution 4 (6) (2017) 1355–1360.

[91] X.-Y. Wang, Y.-L. Wang, S. Wang, B. Li, X.-W. Zhang, L. Dai, R.-M. J. N. Ma, Lasing enhanced surface plasmon resonance sensing 6 (2) (2017) 472–478.

[92] D. J. Bergman, D. Stroud, Physical properties of macroscopically inhomogeneous media, Solid state physics 46 (1992) 147–269.

[93] N. I. Zheludev, S. Prosvirnin, N. Papasimakis, V. Fedotov, Lasing spaser, Nature photonics 2 (6) (2008) 351–354.

[94] K. A. Willets, R. P. Van Duyne, Localized surface plasmon resonance spectroscopy and sensing, Annu. Rev. Phys. Chem. 58 (2007) 267–297.

[95] K. M. Mayer, J. H. Hafner, Localized surface plasmon resonance sensors, Chemical reviews 111 (6) (2011) 3828–3857.

[96] R. F. Oulton, V. J. Sorger, T. Zentgraf, R.-M. Ma, C. Gladden, L. Dai, G. Bartal, X. Zhang, Plasmon lasers at deep subwavelength scale, Nature 461 (7264) (2009) 629–632.

[97] M. H. Motavas, A. Zarifkar, Low threshold nanorod-based plasmonic nanolasers with optimized cavity length, Optics and Laser Technology 111 (2019) 315–322.

[98] R. Ghimire, F. Nematollahi, J.-S. Wu, V. Apalkov, M. I. Stockman, Tmdc-based topological nanospaser: single and double threshold behavior, ACS Photonics 8 (3) (2021) 907–915.

[99] T. H. Maiman, et al., Stimulated optical radiation in ruby (1960).

[100] S. Withanage, T. Nanayakkara, U. Wijewardena, A. Kriisa, R. Mani, The role of surface morphology on nucleation density limitation during the cvd growth of graphene and the factors influencing graphene wrinkle formation, Journal Name: MRS Advances; Journal Volume: 4; Journal Issue: 61-62 (2019) Medium: X; Size: 3337 to 3345.

[101] F. Nematollahi, S. A. Oliaei Motlagh, J.-S. Wu, R. Ghimire, V. Apalkov, M. I. Stockman, Topological resonance in weyl semimetals in a circularly polarized optical pulse, Phys. Rev. B 102 (2020) 125413. `doi:10.1103/PhysRevB.102.125413`.
URL `https://link.aps.org/doi/10.1103/PhysRevB.102.125413`

[102] P. Song, J.-H. Wang, M. Zhang, F. Yang, H.-J. Lu, B. Kang, J.-J. Xu, H.-Y. Chen, Three-level spaser for next-generation luminescent nanoprobe, Science advances 4 (8) (2018) eaat0292.

[103] X.-L. Zhong, Z.-Y. Li, All-analytical semiclassical theory of spaser performance in a

plasmonic nanocavity, Physical Review B 88 (8) (2013) 085101.

[104] P. B. Johnson, R.-W. Christy, Optical constants of the noble metals, Physical review B 6 (12) (1972) 4370.

[105] P. L. Knight, P. W. Milonni, The rabi frequency in optical spectra, Physics Reports 66 (2) (1980) 21–107.